HyspIRI Sun Glint Report

E.J. Hochberg
Nova Southeastern University Oceanographic Center
Dania Beach, FL

C.F. Bruce
R.O. Green
B.V. Oaida
Jet Propulsion Laboratory

F.E. Muller-Karger
University of South Florida
Tampa, FL

C.D. Mobley
Sequoia Scientific, Inc.
Bellevue, WA

Y. Park
CSIRO
Clayton South VIC 3169, Australia

J. Goodman
University of Puerto Rico at Mayagüez
Mayagüez, Puerto Rico

R.G. Knox
E.M. Middleton
K.R. Turpie
S. Ungar
Goddard Space Flight Center
Greenbelt, MD

P.J. Minnett
University of Miami
Coral Gables, FL

C. Gentemann
Remote Sensing Systems
Santa Rosa, CA

R.C. Zimmerman
Old Dominion University
Norfolk, VA

W. Turner
NASA Headquarters
Washington, DC

B.-C. Gao
Naval Research Laboratory
Washington, DC

Executive Summary

The basic objective of the Hyperspectral Infrared Imager (HyspIRI) mission is to provide high-quality imaging spectrometer global observations to characterize a baseline of multiple Earth-surface processes at timescales ranging from seasonal to multi-annual. Among the HyspIRI science objectives, several questions address aquatic ecosystems. Several factors confound easy interpretation of aquatic remote-sensing data. Reflectance of sunlight and skylight off the water surface, or glint, is one potential obstacle to HyspIRI's successful application to study of aquatic systems.

To address this issue, the HyspIRI Sun Glint Subgroup was formed during the fall of 2009. The Subgroup had three main objectives:

(1) Quantitatively characterize the glint problem;
(2) Determine glint impacts to HyspIRI mission aquatic science objectives; and
(3) Provide advice on a way forward to address the glint issue.

To achieve these objectives, the Subgroup initiated a series of weekly teleconferences, beginning in October 2009 and extending into April 2010. The Subgroup first developed a plan of action to address the objectives. Figure 1 provides a brief outline of the steps taken by the Subgroup. The general plan was first to quantitatively characterize glint primarily using radiative transfer models, including both basic analytical equations and HydroMod. The characterization was supplemented with examination of actual remote sensing image data. To assess glint impacts on HyspIRI aquatic science objectives, the Subgroup relied on radiative transfer modeling, using both HydroLight and HydroMod. Various glint correction procedures were assessed using both modeled and real-world data. Finally, the Subgroup agreed on a short list of recommendations for future activities.
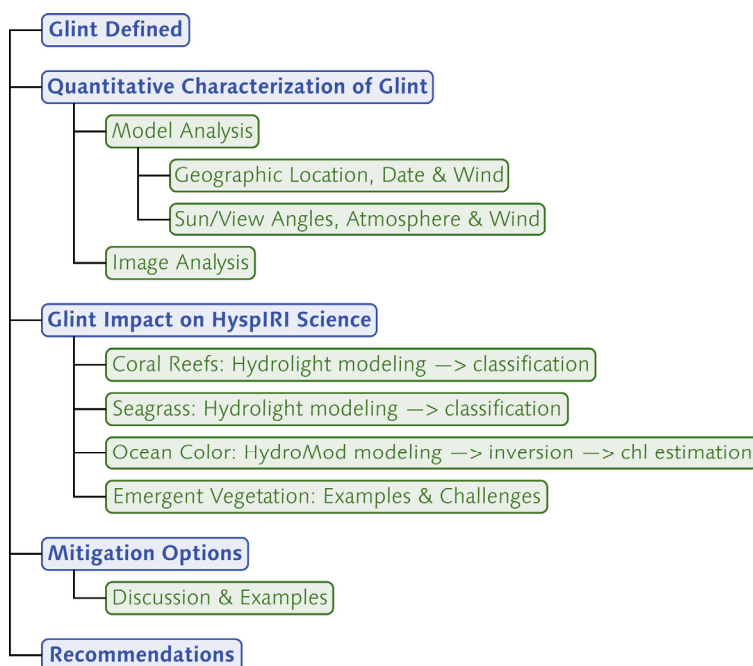

Figure 1. HyspIRI Sun Glint Subgroup Activities Overview

The Subgroup's investigations point to several summary observations:

- Quantitative Characterization of Glint
  – Because HyspIRI views from near zenith, glint has a stronger effect where the sun is also near-zenith.
  – Glint effects are present in a latitudinal band that is 50° to 100° wide, depending on wind speed and the across-track pixel location.
  – Glint at the east edge of the HyspIRI scan line is consistently higher (by a factor of two to five) than at the west edge.
  – HyspIRI glint is sensitive to wind speed at moderate-to-high sun zenith angles, which correspond with low-to-moderate glint in the absence of wind, but it is less sensitive to wind speed at low sun zenith angles, which correspond to high glint in the absence of wind.
  – Glint radiance is a function of incident irradiance.
  – Glint reflectance can surpass that of water-leaving reflectance.
  – Glint reflectance at the sea surface, to first order, is spectrally flat across the visible, near infrared and short-wave infrared.

- Glint Impact on HyspIRI Aquatic Science
  – Results from two basic HyspIRI science objectives, to investigate glint impacts on retrievals for coral reefs and seagrass, showed that expected levels of glint do not appear to dramatically affect classification retrievals.
  – Glint has the greatest impact when retrieval conditions are already marginal, for example, when water column optical properties limit penetration depth.
  – For the open ocean, with very low suspended chlorophyll levels, it is clear that glint correction must be tied to correction for atmospheric aerosols.
  – The impact of glint on retrievals of emergent vegetation is less clear, as measurement and modeling capabilities for these systems lag those for shallow and deep oceans.

- Mitigation Options
  – Avoidance is the simplest method for glint mitigation, but it is often not an option for nearshore and benthic applications.
  – Empirical corrections based on the linear relationship between visible and near-infrared radiances have been demonstrated to perform very well at correcting for glint, but these techniques have yet to be automated.
  – Computation glint reflectance in the near infrared, followed by subtraction of that value in the visible, has also been demonstrated to be very effective at correcting for glint.
  – Discrimination between aerosol and glint reflectance may lead to better determination of near-infrared reflectance.

- Recommendations
  – Glint correction algorithms should be refined and tested using real-world data sets.
  – Further sensitivity analyses should be conducted to investigate glint impacts on other aspects of HyspIRI aquatic science objectives.
  – Field measurements are required to validate model results for select HyspIRI aquatic science objectives.

- In the longer term, a glint "toolbox" of computer code should be developed that would allow a user to select among a suite of glint correction techniques.
- In the longer term, a comprehensive data set of oceanic and atmospheric radiometric parameters would be very valuable for validation of radiative transfer models; this would not only benefit HyspIRI, but would also benefit all remote-sensing missions that observe the ocean.

Table of Contents

1 HyspIRI Sun Glint Subgroup
1.1 Background and Rationale

HyspIRI data and products are designed to address a set of key science questions initially indentified by the National Research Council (NRC) in its Decadal Survey *Earth Science and Applications from Space: National Imperatives for the Next Decade and Beyond*. The general questions identified by the NRC Decadal Survey are consistent with those posed by the HyspIRI Science Study Groups and support a broad set of terrestrial, limnological, and marine research communities, as well as resource management efforts. The questions are grouped into three areas: (1) questions primarily requiring visible-to-shortwave infrared (VSWIR) data; (2) questions primarily requiring thermal infrared (TIR) data; and (3) questions requiring a combination of VSWIR and TIR data.

The HyspIRI mission will include two instruments mounted on a satellite in low-Earth orbit: a VSWIR imaging spectrometer and a TIR multispectral imager. The VSWIR and TIR instruments will both have a spatial resolution of 60 m at nadir. The VSWIR instrument will have a temporal revisit of approximately three weeks (19 days), and the TIR instrument will have a temporal revisit of approximately one week (5 days).

Among the HyspIRI science objectives, several questions address aquatic ecosystems. Among these are as follows:

- How do inland, coastal, and open ocean aquatic ecosystems change due to local and regional thermal climate, land-use change, and other factors? (Combined VSWIR+TIR Question 1)
- What are the seasonal expressions and cycles for terrestrial and aquatic ecosystems, functional groups, and diagnostic species? How are these being altered by changes in climate, land use, and disturbance? (VSWIR Question 2)
- What is the land surface soil/rock and shallow water substrate composition? (VSWIR Question 6)

The unique HyspIRI design allows unprecedented high-quality imaging spectrometer observations in marine and inland aquatic environments. Although the mission will collect data globally, the data over ocean areas deeper than 50 m is planned to be binned into 1-km pixels. Over the coastal ocean and inland aquatic ecosystems, the higher resolution VSWIR and TIR image data can provide excellent information about the composition, distribution, and functional status of aquatic ecosystems. VSWIR data are particularly important for optically shallow waters, such as coral reefs and seagrass beds, and for sandy, rocky or other bottoms from the tropics to high latitudes, where the problem of determining benthic community structure and processes is confounded by unknown water depths and unknown water column optical properties.

That said, there are several well-documented difficulties inherent to satellite-based VSWIR imaging of the ocean (and other aquatic systems). Chief among these is proper correction for atmospheric path radiance contributions to the remotely sensed signal. For shallow waters, there is also the previously mentioned conundrum of correcting for unknown water depth and optical properties to derive bottom composition. These issues are well studied, and they continue to be the focus of ongoing research.

1

The issue of sea surface glint (also referred to as "glitter" or "clutter") has received somewhat less investigative attention. In fact, in existing ocean color missions, the primary method to mitigate for glint is avoidance, rather than correction. However, for researchers utilizing higher-resolution imagery (1–10 m, as opposed to 1 km) to study the coastal zone, glint avoidance is generally not an option. Of necessity, these coastal researchers have developed various approaches to correct for glint impacts where possible. Many published approaches for glint mitigation in high-spatial-resolution remote sensing rely on in-scene statistics, but these methods are not suitable for automated global remote sensing. While mitigation has been repeatedly demonstrated, and such mitigation has been further demonstrated to improve quality of retrievals of subsurface features, the issue is devising a method that can be automated. Many of these approaches are straightforward, but they are typically unrefined in terms of ability to be applied to a variety of imagery on a general basis.

Because several aquatic science questions are central to the HyspIRI mission, the issue of glint and glint mitigation must be investigated. The HyspIRI Sun Glint Subgroup was formed to provide preliminary assessment of the impact of glint on HyspIRI aquatic science objectives. It is important to note that HyspIRI is not the sole owner of the glint problem: glint is an issue for any VSWIR remote sensing of aquatic systems. Thus, the analysis and results of the HyspIRI Sun Glint Subgroup are useful for other current and future mission.

1.2   Glint

In remote sensing of any water body, some of the measured signal arises from light reflected from the water surface. This light does not penetrate into the water column and thus does not provide information about submerged materials. There are two sources for this light: the direct solar beam and skylight. Reflection of the direct solar beam into the remote sensing signal is termed *sun glint*, while reflection of skylight is termed *sky glint*. Together, the sun glint and sky glint contribution constitutes *glint radiance* in the remotely sensed signal. The directionality, distribution, and magnitude of glint are a function of sun angle, view angle, and the state of the water surface. Glint can adversely affect the remote-sensing retrieval of subsurface features (Wang and Bailey 2001; Hochberg et al. 2003). Qualitative examples of sun glint and sky glint scales, derived from Quickbird imagery, are given in Figures 1.2-1 through 1.2-4.

In traditional remote sensing of ocean color, glint mitigation is achieved largely by avoidance: the radiometer is simply pointed in a direction away from the glint pattern on the sea surface (Wang and Bailey 2001). The remotely sensed portion of the ocean is presumed to include some small glint contribution; this contribution is modeled using Cox-Munk wind-wave statistics (Cox and Munk 1954) and then subtracted from the total signal. These corrections are designed for the open ocean, where wind waves are assumed to be mono-directional, and for low-resolution data ($\geq$1 km), where glint effects occur at a scale much smaller than pixel dimensions. For nearshore or shallow environments, because of the varied topography, the assumption of mono-directionality of waves (Borrego 1993) is generally not valid. Moreover, ocean color algorithms (Fraser et al. 1997; Wang and Bailey 2001) are designed for low-resolution data ($\geq$1 km), where glint effects occur at a scale much smaller than pixel dimensions.

2
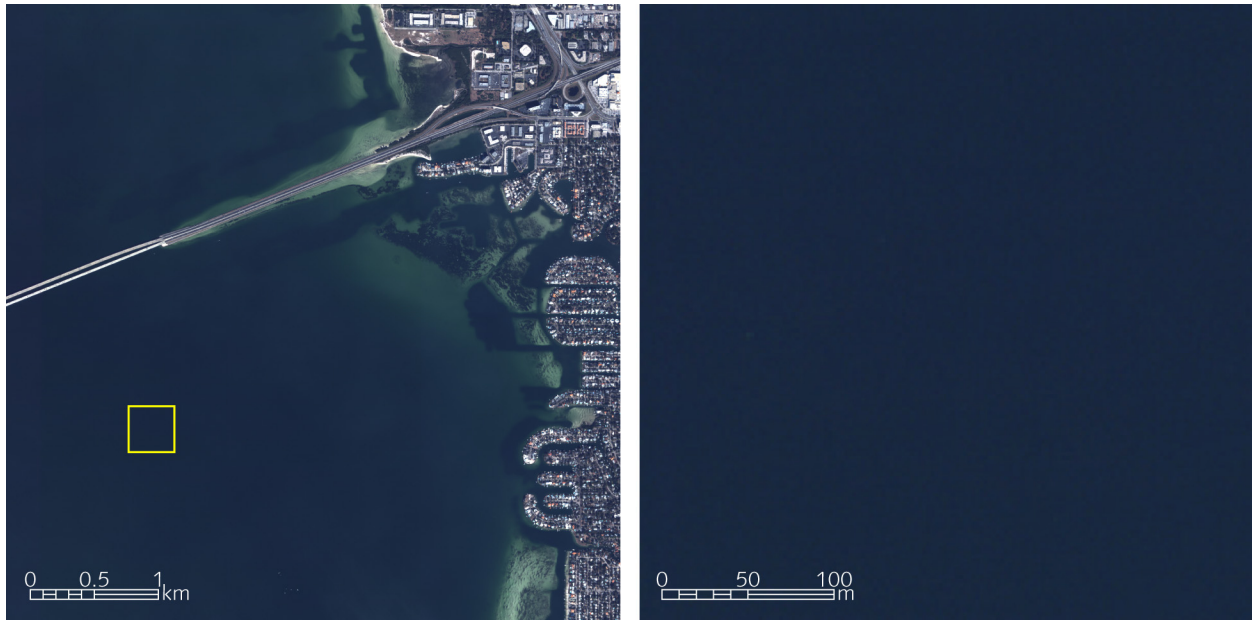
Figure 1.2-1. Quickbird scene of Tampa Bay, Florida. (Left) Wide-area scene to provide context. Yellow box shows location of close-up detail scene. (Right) Close-up scene to show detail (if any) of glint distribution. Wind conditions are very calm, resulting in virtually no capillary waves. This is a sheltered embayment, so there are also no surface gravity waves. In this case, there is sky glint but no sun glint.
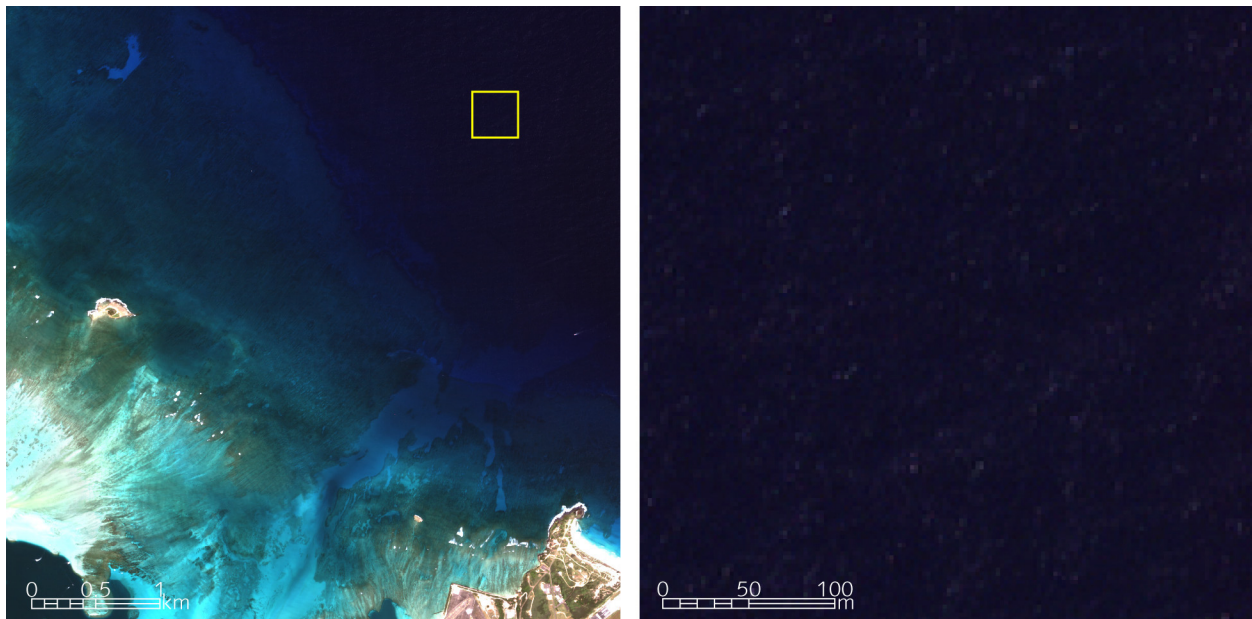
Figure 1.2-2. Quickbird scene of Kaneohe Bay, Hawaii. (Left) Wide-area scene to provide context. Yellow box shows location of close-up detail scene. (Right) Close-up scene to show detail of glint distribution. Wind speed is low, but non-zero, resulting in some capillary waves. Small (~0.5 m) surface gravity waves generated at distance are also present. In this case, there are both sky glint and sun glint, although sun glint intensity is minimal.

3
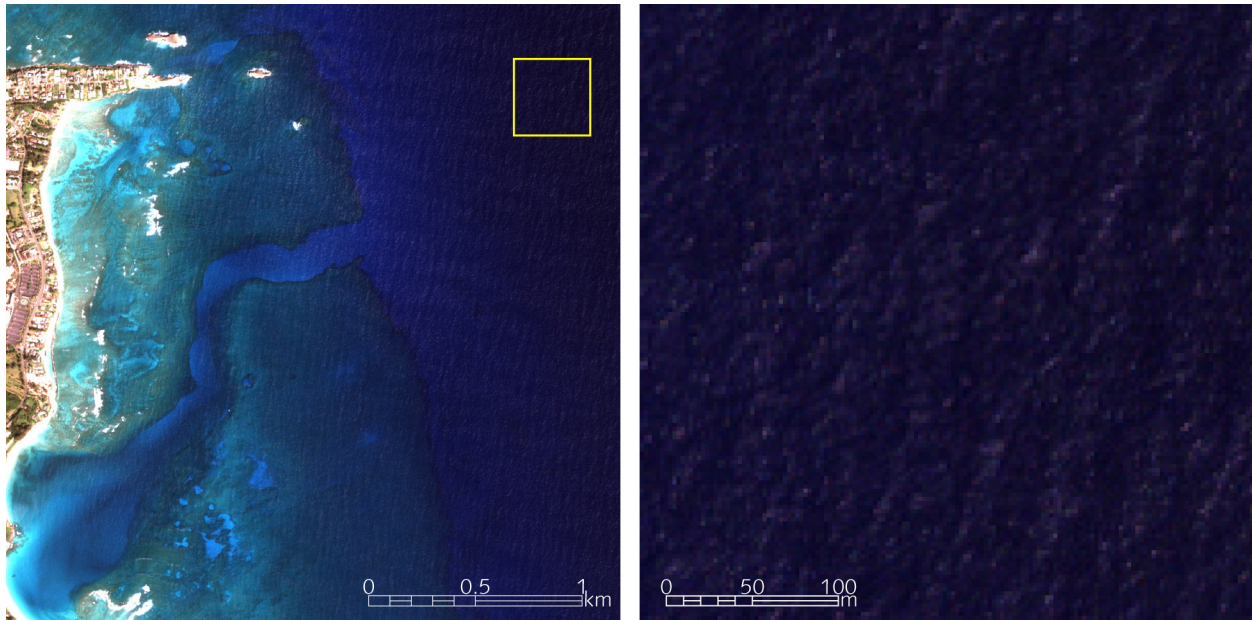
Figure 1.2-3. Quickbird scene of Punaluu, Hawaii. (Left) Wide-area scene to provide context. Yellow box shows location of close-up detail scene. (Right) Close-up scene to show detail of glint distribution. Typical trade wind speed is about 5–10 m s^{-1}. Trade wind waves (~2 m) are also present. Sun glint is readily apparent on the faces of surface gravity waves.
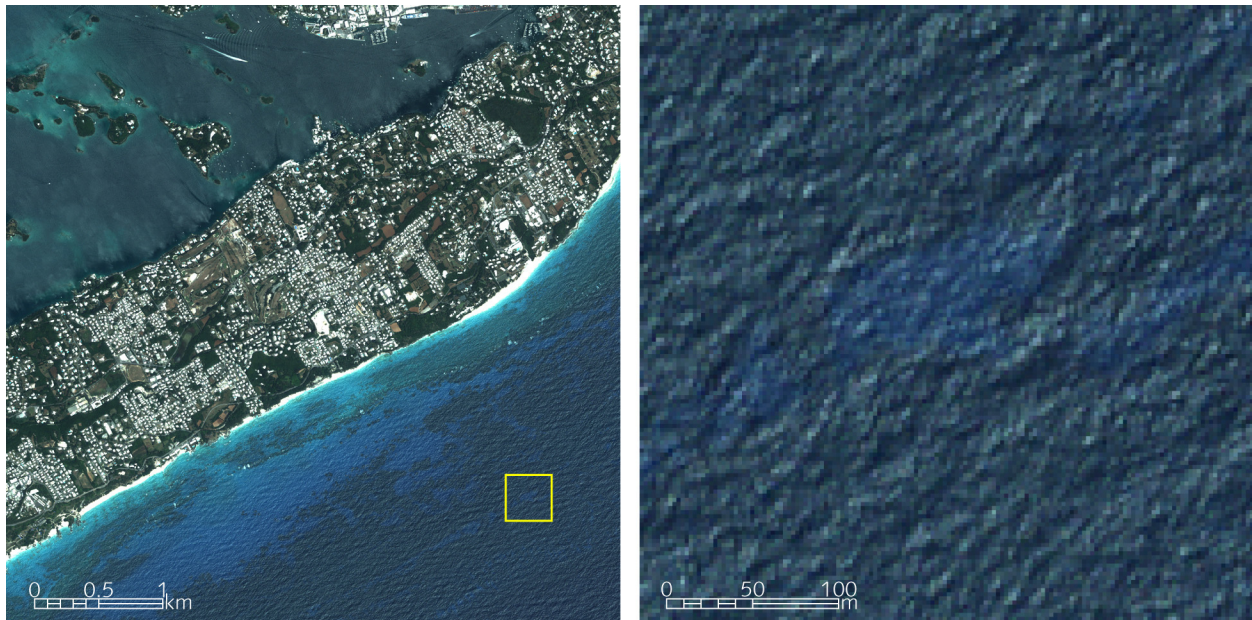
Figure 1.2-4. Quickbird scene of Bermuda. (Left) Wide-area scene to provide context. Yellow box shows location of close-up detail scene. (Right) Close-up scene to show detail of glint distribution. This scene illustrates a nearly stochastic sea surface; wind chop is convolved with small surface gravity waves. In this case, sensor view angle also increases sun glint intensity.

HyspIRI has a nominal ground sample distance of 60 m, which is roughly equivalent to the scale of gravity waves on the ocean surface. Thus, if the ocean is not flat, any given HyspIRI pixel is subject to glint, whether or not the sensor is pointed away from the main glint pattern. The

average amount of glint will vary statistically by latitude as a function of the time of the year, but any given pixel can contain more or less glint.

1.3   Tasks

The objective of the Sun Glint Subgroup is to characterize the potential impact of sun glint on aquatic science applications and to develop a mitigation approach for removing or reducing the impact of sun glint. The approaches to glint should be quantitative, physically based, and traced to work that is supported by the refereed literature. Glint results must be linked to the relevant HyspIRI science questions.

The original tasks for the Subgroup are as follows:

- Define sun glint plan for HyspIRI;
- Characterize sun glint effects of different orbits/crossing times and view angles for inclusion in plan;
- Outline Phase A process for developing HyspIRI-specific algorithm(s) to mitigate and/or remove sun glint building on existing and future published techniques;
- Engage different disciplines of the coastal and marine communities to assess percentages of additional radiance from sun glint, aerosols, and other atmospheric effects they can tolerate and still achieve their science—assessments included in the Sun Glint Plan; and
- Prepare an initial draft Sun Glint Plan to be ready for the HyspIRI Mission Concept Review (MCR) and complete a final plan with algorithm(s) to address glint and other during HyspIRI mission Phase A/B, including plans to test the algorithm(s).

1.3.1   Quantitatively Characterize Glint

The first component of this report is a quantification of glint levels across the range of conditions that HyspIRI will be imaging aquatic systems. Important parameters that determine glint magnitude include sun zenith and azimuth angles, sensor (view) zenith and azimuth angles, atmosphere gas and aerosol conditions, and state of the sea surface. Additional subsurface parameters are required to characterize aquatic science objectives, e.g., water depth, water optical properties, and nature of the sea floor. Aquatic bodies are complex optical systems, and complete characterization would require a concerted effort beyond the current scope of work. The objective of the HyspIRI Sun Glint Subgroup has been characterization of glint primarily through computer-based modeling (Section 3.1), as well as through examination of existing remote-sensing data (Section 3.2).

1.3.2   Determine Glint Impacts on HyspIRI Science

The second component of this report is an investigation into the impacts of glint on representative HyspIRI science objectives. These objectives were initially defined by the NRC Decadal Survey and fall under the key science questions identified by the HyspIRI Science Study Groups and the wider research community. Of importance is to examine the magnitude and errors in surface reflectance to assess whether the signal introduced by glint renders accurate retrieval of subsurface radiance reflectance impossible. For the current report, the Sun Glint

Subgroup has chosen to investigate glint impacts on retrievals for coral reef (Section 4.1), seagrass (Section 4.2) and optically deep-water (Section 4.3) science. Emergent vegetation is another important objective, but neither suitable models nor data were available to the Subgroup, and analysis has been deferred. Because appropriate radiometric data sets are also not available to investigate the three HyspIRI science questions that are addressed, the Subgroup has decided to rely on modeling using HydroLight and/or HydroMod to generate the necessary data.

1.3.3 Suggest Options for Way Forward

The final component of this report is a discussion of options for the "way forward." This includes the Subgroup's collective suggestions for glint mitigation approaches that currently seem most promising (Section 5), as well as recommended directions for future investigations (Section 6). This discussion is not exhaustive, but it does reflect the consensus of the Subgroup.

1.4 Participants

Table 1.4-1 lists the individuals nominally in the HyspIRI Sun Glint Subgroup and their institutions. The Subgroup initiated weekly teleconferences in October 2009. These individuals receive weekly email reminders about the teleconferences, as well as copies of all documents circulated within the Subgroup.

Table 1.4-1. HyspIRI Sun Glint Subgroup email distribution list.

Name	Institution
Paul Bisset	Florida Environmental Research institute
Paula Bontempi	NASA Headquarters Ocean Biology and Biogeochemistry
Vittorio Brando	Australia Commonwealth Scientific and Industrial Research Organisation
Carl Bruce	NASA Jet Propulsion Laboratory
Kyle Cavanaugh	University of California at Santa Barbara
Arnold Dekker	Australia Commonwealth Scientific and Industrial Research Organisation
Heidi Dierssen	University of Connecticut
Bo-Cai Gao	Naval Research Laboratory
James Goodman	University of Puerto Rico at Mayagüez
Robert Green	NASA Jet Propulsion Laboratory
Eric Hochberg	National Coral Reef Institute, Nova Southeastern University
Robert Knox	NASA Goddard Space Flight Center
Fred Lipschultz	NASA Headquarters Ocean Biology and Biogeochemistry
Betsy Middleton	NASA Goddard Space Flight Center
Peter Minnet	Rosenstiel School of Marine and Atmospheric Science, University of Miami
Curtis Mobley	Sequoia Scientific, Inc.
Frank Muller-Karger	College of Marine Science, University of South Florida
Bogdan Oaida	NASA Jet Propulsion Laboratory
Youngje Park	Australia Commonwealth Scientific and Industrial Research Organisation
Thomas Schroeder	Australia Commonwealth Scientific and Industrial Research Organisation
Dave Siegel	University of California at Santa Barbara
Woody Turner	NASA Headquarters Biological Diversity
Kevin Turpie	NASA Goddard Space Flight Center
Stephen Ungar	NASA Goddard Space Flight Center
Richard Zimmerman	Old Dominion University

1.5   Timeline

The timeline for Subgroup activities is short. Discussion began in late September 2009, with an initial date for the draft report at the end of January 2010. The current timeline has the draft report being completed in June 2010.

September 2009	Initiate Sun Glint Subgroup
October 2009	Begin teleconferencing Begin modeling of glint intensities
November 2009	Continued modeling of glint intensities Continued discussions
December 2009	Begin modeling of glint impact on science Continued discussions
January 2010	Continued modeling of glint impact on science Continued discussions Begin draft outline of report
April 2010	Continued modeling Continued discussions Completion of draft report
May 2010	Feedback/Review of draft report
June 2010	Revise draft report
June–July 2010	Pre-Phase A HyspIRI Sun Glint Subgroup Report

2 Literature Review

Glint has been recognized as a potentially confounding factor from the outset of ocean remote sensing. Correspondingly, there has been a fair amount of research into the subject. Kay et al. (2009) provide a thorough review of the physical processes that engender glint, as well as existing mitigation strategies.

Approaches to glint mitigation follow the strategies of avoidance and correction. Avoidance refers to physically pointing the remote sensor toward the ocean at an angle that minimizes specular reflection at the sea surface. The actual pointing angle is determined by the position of the sensor relative to the position of the sun, generally assuming the ocean is smooth. This is a fundamental component of the SeaWiFS glint mitigation strategy, which was possible since SeaWiFS was designed solely for ocean color.

Even in cases where the bulk of direct specular reflection can be avoided, sky-glint contamination remains, as does sun glint that arises due to deviations from the level-surface ocean, i.e., waves. As a result, glint correction is also a central component of ocean remote sensing. There are two basic approaches to glint correction: (1) statistical modeling of sea surface state to infer glint contribution and (2) direct estimation of glint contribution from the remote-sensing image data. Statistical modeling of sea surface state can be traced to Cox and Munk (1954), who analyzed aerial photographs of sun glint to infer statistics of the sea surface wave slope distribution as a function of wind speed. This is the basis for ocean color glint correction: knowledge of wind speed can be used to estimate the sea surface wave slope distribution, which in turn can be used to estimate the combined sky- and sun-glint radiances.

An alternative correction approach is to estimate the glint signal directly from remote-sensing data. This approach is based on the common assumption that there is no water-leaving radiance in the near infrared (NIR) due to strong absorption of light by water at these wavelengths, especially greater than 900 nm (Figure 2-1). This means that top-of-atmosphere NIR signals can arise only from the atmosphere or sea surface. After atmosphere corrections, the only remaining NIR signals must originate from the sea surface, i.e., glint.

Based on these principles, several researchers have developed interactive, empirical approaches to glint correction (Tassan 1994; Hochberg et al. 2003; Hedley et al. 2005; Lyzenga et al. 2006). These correction techniques all rely on the linear relationship between glint radiances at visible and near-infrared wavelengths. In addition, these correction techniques generally require human interaction to develop necessary statistics describing that linear relationship.

It is important to note that the linear relationship between VIS and NIR glint radiances has a physical basis: the index of refraction of seawater is (nearly) the same at VIS and NIR wavelengths (Figure 2-2). As a result, the reflectance of the water surface is (nearly) spectrally flat, i.e., glint has the same reflectance at VIS and NIR wavelengths. This is the basis for an empirical correction that does not require human interaction (Gao et al. 2000). Simply, after atmospheric correction, any remaining NIR reflectance is due to glint. This glint reflectance can simply be subtracted from VIS wavelengths, leaving only water-leaving reflectance.

For moderate- and low-spatial-resolution remote sensing, it is often sufficient to mitigate for glint via simple avoidance coupled with statistical estimation of sub-pixel glint content. Published methods for glint mitigation in high-spatial-resolution remote sensing all rely on in-scene statistics. Such methods are not suitable for automated global remote sensing. It is important to note that mitigation has been repeatedly demonstrated, and such mitigation has been further demonstrated to improve quality of retrievals of subsurface features. However, the issue is devising a method that can be automated.
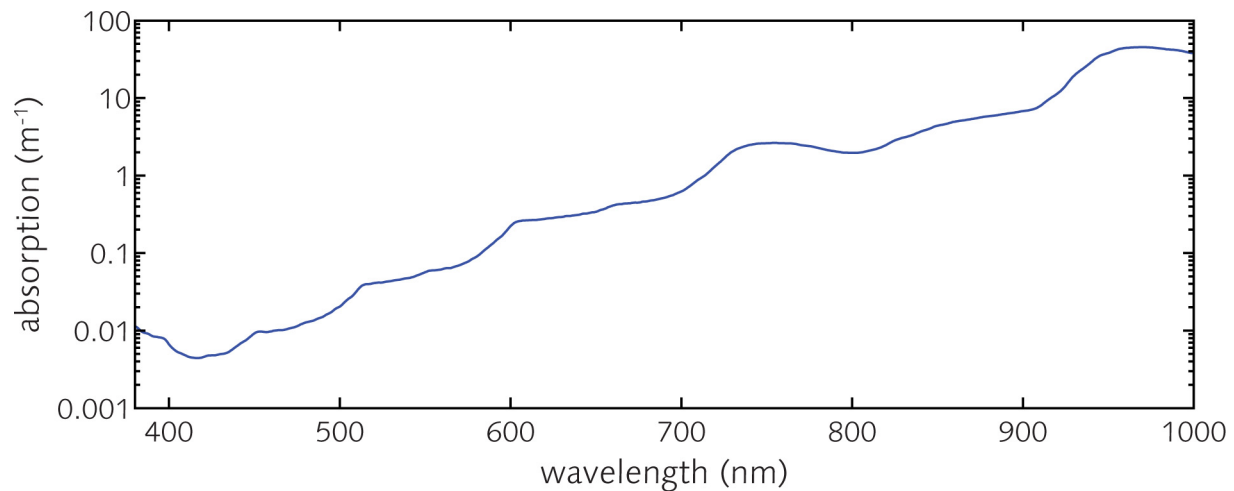
Figure 2-1. Water absorbs light very strongly at NIR wavelengths, especially >900 nm. Water-leaving radiance at these wavelengths is negligible. Data at VIS wavelengths from Pope and Fry (1997); data at NIR wavelengths from Kou et al. (1993).
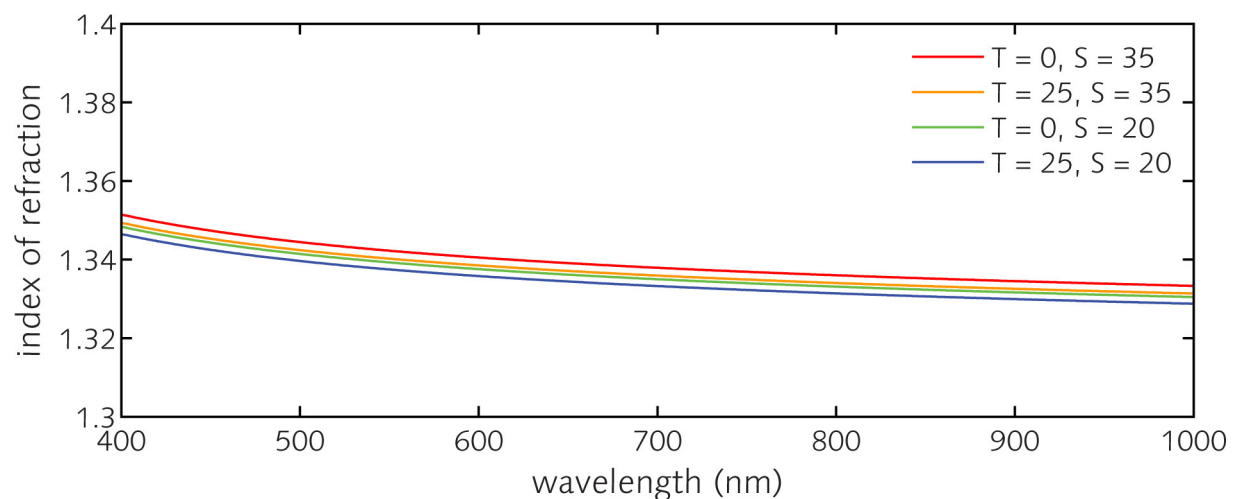
Figure 2-2. Index of refraction of water. Values are calculated following empirical model of Quan and Fry (1995), which is valid for wavelength range 400–700 nm, temperature range 0°–30°, and salinity range 0‰–35‰. Values are modeled for four combinations of temperature (T, °C) and salinity (S, ‰).

3   Quantitative Characterization of Glint
3.1   Modeling

The HyspIRI Sun Glint Subgroup has adopted computer-based radiative transfer modeling as the primary route to characterize glint for two reasons. First, modeling provides exact numerical determination of light fluxes that can be partitioned based on their sources (e.g., subsurface vs. glint). Second, there are no existing comprehensive data sets that contain the entire suite of radiometric and environmental measurements necessary to investigate both varying degrees of glint and the impact of glint on remote sensing science retrievals.

Two modeling approaches are utilized in this report. The first approach, performed by Youngje Park of Australia's Commonwealth Scientific and Industrial Research Organisation (CSIRO), utilizes analytical and empirical equations to determine glint reflectance as a function of latitude for four key dates in the HyspIRI orbit (March 21, June 21, September 21, and December 21). These simulations describe the approximate high, low and average glint values that can be expected for HyspIRI. Details of the model approach and results are provided in Section 3.1.1.

The second approach, performed by Curtis Mobley of Sequoia Scientific, Inc., utilizes HydroMod, a coupled HydroLight-MODTRAN radiative transfer model. HydroLight computes in-water and water-leaving spectral radiance distributions, while MODTRAN computes radiance distributions in and above the atmosphere. HydroMod simulations are used here to investigate glint under specific coupled atmosphere-water column conditions. Chosen conditions do not necessarily cover extremes that HyspIRI may encounter but are representative of "typical" conditions. Details of the model approach and results are provided in Section 3.1.2.

3.1.1   Glint Reflectance: Geographic Location, Date, and Wind

In order to investigate seasonal variability of glint reflectance, computations were made for four key dates (March 21, June 21, September 21, December 21) for which HyspIRI orbits have been simulated. Model computations differentiated the east edge, middle point, and west edge of the HyspIRI swath to examine variability within a cross-track line. Wind data were taken from global wind speed climatology.

In this model estimation, the nondimensional sun glint reflectance at the surface (ρ_g^{0+}) is defined by

$$\rho_g^{0+} = \frac{\pi L_g^{0+}}{E_d^{0+}},$$
(3.1.1-1)

where L_g^{0+} is the radiance at surface due to sun glint and E_d^{0+} is the downward irradiance (due to direct sun) at the surface. This definition is equivalent to

$$\rho_g^{0+} = \pi \, BRDF(a, w; \theta_0, \phi_0 \rightarrow \theta_v, \phi_v),$$
(3.1.1-2)

where θ_0, ϕ_0, θ_v, and ϕ_v are the solar zenith angle, the solar azimuth angle, the sensor zenith angle and the sensor azimuth angle, respectively; and $BRDF(a, w; \theta_0, \phi_0 \rightarrow \theta_v, \phi_v)$ is the bidirectional

reflectance distribution function (with units sr^{-1}; Nicodemus et al. 1977) for reflectance by the air-water surface itself (not including the water below the surface), including the effects of sea surface roughness. Equation (3.1.1-2) shows that the nondimensional reflectance of equation (3.1.1-1) is the surface BRDF normalized by the BRDF of a perfectly reflecting (white) Lambertian surface, for which the BRDF is $1/\pi$. By purely geometrical consideration, it is related to the surface slope distribution (Cox and Munk 1954):

$$\rho_g^{0+} = \frac{\pi \rho_F(\omega) P_s(\theta_0, \phi_0, \theta_v, \phi_v; W)}{4 \mu_v \mu_0 \cos^4(\theta_n)},$$

(3.1.1-3)

where $\rho_F(\omega)$ is the Fresnel reflectance; $P_s(\theta_0, \phi_0, \theta_v, \phi_v; W)$ is the probability of surface slope for which the incident ray with direction (θ_0, ϕ_0) is reflected to the direction (θ_v, ϕ_v); W is the wind speed about 10 m above sea surface; ω is half of the angle between the vectors of surface to sun and surface to sensor; and μ_v and μ_0 are the cosines of θ_v and θ_0. This formula for the sun glint reflectance at sea surface (equation [3.1.1-3]) can be found in Viollier et al. (1980) and is used for ocean color image processing (Montagner et al. 2003; Gordon and Voss 2004). Equation (3.1.1-3) considers the highly pointing incident solar beam reflected to the sensor, and thus it excludes the sky glint effect. In fact, Cox and Munk (1954) removed sky glint and water-leaving radiances in their analysis of aerial photographs.

The wind-direction-independent (azimuthally isotropic) surface slope distribution function, $P_s(\theta_0, \phi_0, \theta_v, \phi_v; W)$ is approximated by

$$P_s(\theta_0, \phi_0, \theta_v, \phi_v; W) = \frac{1}{\pi \sigma^2} \exp\left(-\frac{\tan^2 \theta_n}{\sigma^2}\right),$$

(3.1.1-4)

where $\sigma^2 = 0.003 + 0.512 W$.

The wind-direction-dependent (azimuthally anisotropic) model for the slope distribution is expressed as follows:

$$P_s(\theta_0, \phi_0, \theta_v, \phi_v; W, X) = \frac{1}{2\pi \sigma_c \sigma_u} \exp\left(-\frac{\xi^2 + \eta^2}{2}\right) \cdot$$
$$\left\{\begin{array}{l} 1 - \frac{1}{2} c_{21}(\xi^2 - 1)\eta - \frac{1}{6} c_{03}(\eta^3 - 3\eta) + \frac{1}{24} c_{40}(\xi^4 - 6\xi^2 + 3) \\ + \frac{1}{4} c_{22}(\xi^2 - 1)(\eta^2 - 1) + \frac{1}{24} c_{04}(\eta^4 - 6\eta^2 + 3) \end{array}\right\},$$

(3.1.1-5)

where

$\sigma_c^2 = 0.003 + 0.00192 \times W$;
$\sigma_u^2 = 0.00316 \times W$;
$\xi = z_c / \sigma_c$;
$\eta = z_u / \sigma_u$;
$z_c = \tan \beta \sin \alpha$: surface slope in crosswind direction;

$z_u = \tan \beta \cos \alpha$: surface slope in upwind direction;
$\alpha = \phi_n - X$: azimuth of surface normal vector, ϕ_n from upwind direction, X ;
$\beta = \theta_n$: zenith of surface normal vector;
$c_{21} = 0.01 - 0.0086 \times W$;
$c_{03} = 0.04 - 0.033 \times W$;
$c_{40} = 0.40$;
$c_{22} = 0.12$; and
$c_{04} = 0.23$.

The sun-glint reflectance is determined from sun-sensor angles and wind speed according to equation (3.1.1-3). Sun zenith varies with season and latitude. Sensor-viewing angles are determined by pixel position within a cross-track line. To examine seasonal effects on sun glint, HyspIRI orbits are simulated by latitude, altitude, sun zenith angle, and sun azimuth angle for four key dates: March 21, June 21, September 21, and December 21.

Sun azimuth angles were measured counterclockwise from spacecraft flight direction. Sensor azimuth seen from the ground is 90° (or -90°) measured counterclockwise from spacecraft flight direction toward west (or east) edge of the ground track. By pointing 4° west, the sensor-viewing zenith at scene edges is 10° (or 2°) at the western (or eastern) edge. Within a cross-track line, the minimum glint reflectance would occur at the west edge (sensor azimuth 90° and zenith 10°), while the maximum would occur at the east edge (sensor azimuth -90° and zenith 2°). To highlight this cross-track variability, sun-glint reflectance was computed separately for east edge, middle point and west edge.

Glint Global Longitudinal Variability

The global wind climatology is given as Weibull parameters as function of location (latitude and longitude) for each month, which are converted to the mean and standard deviation. (Details on the global wind speed climatology are described in Appendix A.) Here, the wind climatology is used to estimate (1) global longitudinal variability for given latitude and month and (2) local (temporal) variability for given latitude, longitude, and month. Since wind direction information is not available in this climatology, we use the wind-direction-independent glint model (equation [3.1.1-4]). In this section, we assume the index of refraction of seawater relative to air to be a constant 1.34, although the index of refraction does, in fact, vary slightly with wavelength. Medium, minimum, and maximum wind speeds at each latitude and month were extracted from the <u>mean</u> wind speed field, which is converted from the Weibull parameters. These numbers provide a rough estimate of the medium, low and high bounds of the wind speed for each latitude and month; they are used as input to the sea surface slope model as described above.

Figures 3.1.1-1 through 3.1.1-4 illustrate the simulated global longitudinal variability of sun-glint reflectance for the simulated HyspIRI orbits for the four key dates. Table 3.1.1-1 provides the expected range (min ~ max) of the sun-glint reflectances for the east and west edges of the HyspIRI field of view.

Table 3.1.1-1. Summary table for global longitudinal variability of the sea-surface sun-glint reflectance for the east and west edges of the HyspIRI field of view.

	March 21		June 21		September 21		December 21	
Lat	West edge	East edge	West edge	East edge	West edge	East edge	West edge	East edge
70°N	< 0.001	< 0.001	0.000 ~ 0.001	0.000 ~ 0.005	< 0.001	< 0.001	< 0.001	< 0.001
60°N	< 0.001	0.000 ~ 0.002	0.000 ~ 0.007	0.001 ~ 0.021	< 0.001	0.000 ~ 0.001	< 0.001	< 0.001
50°N	0.000 ~ 0.002	0.000 ~ 0.005	0.000 ~ 0.018	0.005 ~ 0.047	0.000 ~ 0.001	0.000 ~ 0.003	< 0.001	< 0.001
40°N	0.000 ~ 0.005	0.000 ~ 0.015	0.005 ~ 0.030	0.037 ~ 0.083	0.000 ~ 0.003	0.000 ~ 0.010	< 0.001	0.000 ~ 0.001
30°N	0.000 ~ 0.007	0.004 ~ 0.025	0.011 ~ 0.036	0.076 ~ 0.108	0.000 ~ 0.008	0.003 ~ 0.029	0.000 ~ 0.000	0.000 ~ 0.002
20°N	0.000 ~ 0.015	0.010 ~ 0.044	0.011 ~ 0.035	0.059 ~ 0.104	0.001 ~ 0.019	0.015 ~ 0.054	0.000 ~ 0.003	0.000 ~ 0.008
10°N	0.001 ~ 0.021	0.020 ~ 0.055	0.002 ~ 0.031	0.016 ~ 0.065	0.002 ~ 0.028	0.044 ~ 0.075	0.000 ~ 0.006	0.000 ~ 0.017
0°	0.000 ~ 0.019	0.021 ~ 0.055	0.000 ~ 0.019	0.001 ~ 0.037	0.005 ~ 0.028	0.060 ~ 0.076	0.000 ~ 0.010	0.002 ~ 0.034
10°S	0.001 ~ 0.012	0.014 ~ 0.048	0.000 ~ 0.007	0.000 ~ 0.015	0.001 ~ 0.025	0.020 ~ 0.064	0.001 ~ 0.017	0.016 ~ 0.052
20°S	0.001 ~ 0.009	0.005 ~ 0.030	0.000 ~ 0.002	0.000 ~ 0.006	0.000 ~ 0.019	0.006 ~ 0.041	0.002 ~ 0.021	0.043 ~ 0.059
30°S	0.000 ~ 0.005	0.002 ~ 0.015	< 0.001	0.000 ~ 0.001	0.001 ~ 0.009	0.004 ~ 0.021	0.007 ~ 0.021	0.041 ~ 0.058
40°S	0.000 ~ 0.001	0.000 ~ 0.004	< 0.001	< 0.001	0.000 ~ 0.003	0.000 ~ 0.008	0.003 ~ 0.015	0.018 ~ 0.044
50°S	0.000 ~ 0.001	0.000 ~ 0.002	< 0.001	< 0.001	0.000 ~ 0.002	0.000 ~ 0.004	0.002 ~ 0.011	0.009 ~ 0.028
60°S	< 0.001	0.000 ~ 0.001	< 0.001	< 0.001	< 0.001	0.000 ~ 0.001	0.000 ~ 0.005	0.001 ~ 0.013
70°S	< 0.001	< 0.001	< 0.001	< 0.001	< 0.001	< 0.001	< 0.001	0.000 ~ 0.002

Figure 3.1.1-1. Global longitudinal variability of sea-surface sun-glint reflectance for the **March 21** HyspIRI orbit for (a) three levels of wind speed, which were used to compute sea-surface glint at (b) the west edge, (c) the middle point, and (d) the east edge of the HyspIRI field of view.
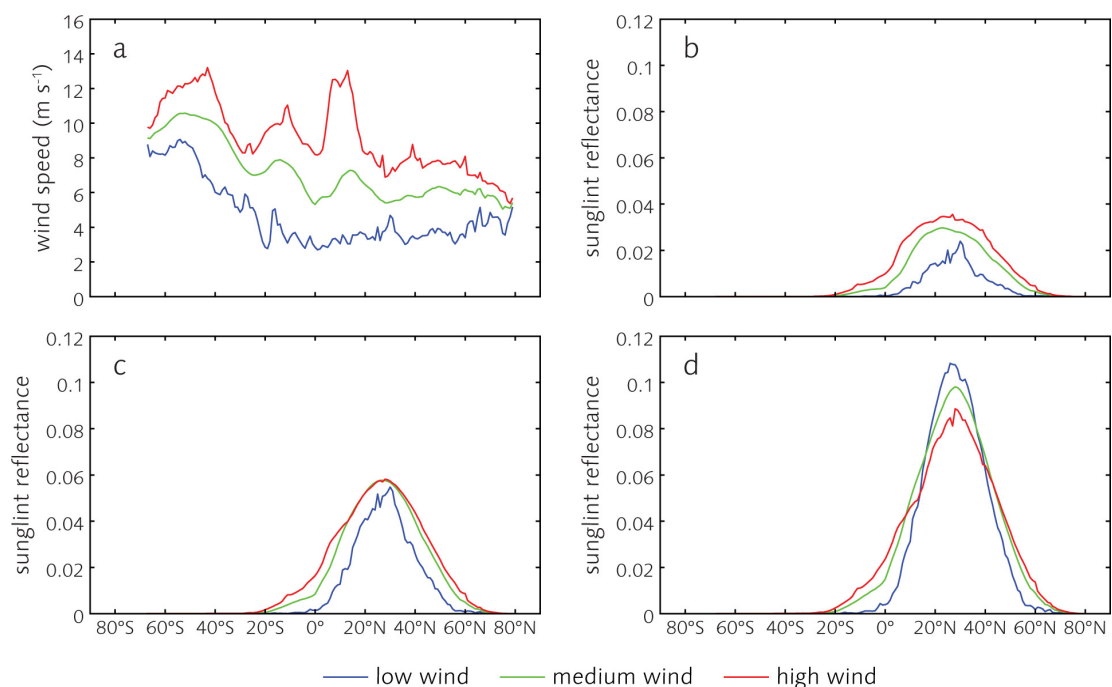
Figure 3.1.1-2. Global longitudinal variability of sea-surface sun-glint reflectance for the **June 21** HyspIRI orbit for (a) three levels of wind speed, which were used to compute sea-surface glint at (b) the west edge, (c) the middle point, and (d) the east edge of the HyspIRI field of view.

Figure 3.1.1-3. Global longitudinal variability of sea-surface sun-glint reflectance for the **September 21** HyspIRI orbit for (a) three levels of wind speed, which were used to compute sea-surface glint at (b) the west edge, (c) the middle point, and (d) the east edge of the HyspIRI field of view.
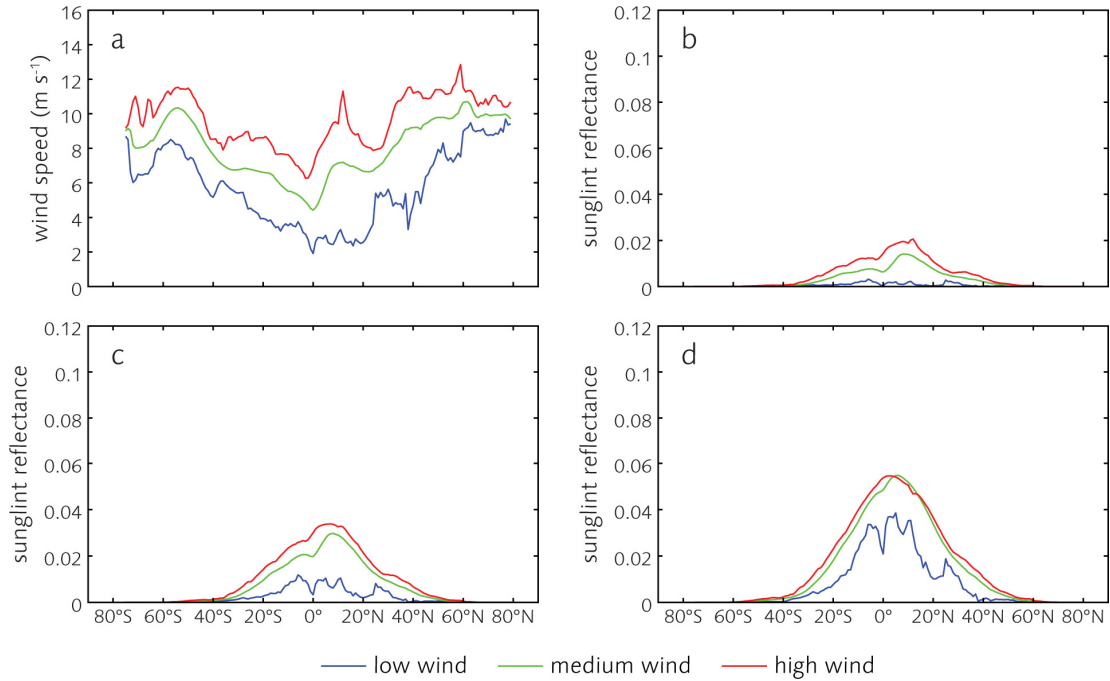
14

Figure 3.1.1-4. Global longitudinal variability of sea-surface sun-glint reflectance for the **December 21** HyspIRI orbit for (a) three levels of wind speed, which were used to compute sea-surface glint at (b) the west edge, (c) the middle point, and (d) the east edge of the HyspIRI field of view.

Glint Regional Temporal Variability

By this model, the glint reflectance is given as function of solar angles, view angles, and wind speed. Wind speed climatology varies across the world's oceans. To further examine glint intensities at a regional scale, we used the wind speed climatology for the longitude band 165°W–150°W. Again, we estimated three wind speed levels: medium, low, and high. The medium wind speed is computed as an arithmetic mean of the mean wind field within the longitude zone for each latitude. The high and low wind speeds were computed as the arithmetic mean plus/minus one sigma, respectively. The sigma was taken as a mean of the standard deviation (computed from the Weibull parameters) over the given longitude range.

Figures 3.1.1-5 through 3.1.1-8 illustrate example results from modeling sun-glint reflectance in the specific longitude range (165°W–150°W) for the same four key dates as previously modeled. Note the y-axis scale for sun-glint reflectance varies depending on date. Table 3.1.1-2 summarizes the expected range of the sun-glint reflectances for the east and west edges of the HyspIRI field of view.

15

Table 3.1.1-2. Summary table for local temporal variability of the sea-surface sun-glint reflectance for the longitude band 165°W–150°W.

	March 21		June 21		September 21		December 21	
	West edge	East edge	West edge	East edge	West edge	East edge	West edge	East edge
70°N	< 0.001	< 0.001	< 0.001	< 0.001	< 0.001	< 0.001	< 0.001	< 0.001
60°N	0.000 ~ 0.001	0.000 ~ 0.003	0.000 ~ 0.009	0.000 ~ 0.023	0.000 ~ 0.001	0.000 ~ 0.002	< 0.001	< 0.001
50°N	0.000 ~ 0.003	0.000 ~ 0.008	0.000 ~ 0.022	0.005 ~ 0.047	0.000 ~ 0.002	0.000 ~ 0.006	< 0.001	< 0.001
40°N	0.000 ~ 0.007	0.001 ~ 0.016	0.004 ~ 0.030	0.036 ~ 0.084	0.000 ~ 0.005	0.000 ~ 0.014	< 0.001	0.000 ~ 0.001
30°N	0.000 ~ 0.011	0.004 ~ 0.029	0.008 ~ 0.037	0.075 ~ 0.107	0.000 ~ 0.011	0.002 ~ 0.032	0.000 ~ 0.001	0.000 ~ 0.003
20°N	0.002 ~ 0.018	0.016 ~ 0.044	0.024 ~ 0.037	0.061 ~ 0.098	0.003 ~ 0.022	0.021 ~ 0.055	0.000 ~ 0.003	0.000 ~ 0.010
10°N	0.010 ~ 0.022	0.043 ~ 0.055	0.005 ~ 0.030	0.025 ~ 0.066	0.004 ~ 0.025	0.055 ~ 0.075	0.000 ~ 0.007	0.003 ~ 0.019
0	0.005 ~ 0.020	0.042 ~ 0.055	0.001 ~ 0.014	0.005 ~ 0.035	0.011 ~ 0.025	0.063 ~ 0.077	0.002 ~ 0.011	0.011 ~ 0.035
10°S	0.001 ~ 0.015	0.011 ~ 0.048	0.000 ~ 0.006	0.001 ~ 0.014	0.007 ~ 0.024	0.035 ~ 0.064	0.002 ~ 0.016	0.027 ~ 0.052
20°S	0.000 ~ 0.009	0.004 ~ 0.030	0.000 ~ 0.002	0.000 ~ 0.005	0.002 ~ 0.018	0.009 ~ 0.041	0.003 ~ 0.022	0.041 ~ 0.059
30°S	0.000 ~ 0.006	0.000 ~ 0.017	< 0.001	0.000 ~ 0.001	0.000 ~ 0.010	0.001 ~ 0.022	0.002 ~ 0.022	0.029 ~ 0.058
40°S	0.000 ~ 0.002	0.000 ~ 0.007	< 0.001	0.000 ~ 0.001	0.000 ~ 0.005	0.000 ~ 0.011	0.002 ~ 0.017	0.013 ~ 0.044
50°S	0.000 ~ 0.001	0.000 ~ 0.003	< 0.001	< 0.001	0.000 ~ 0.002	0.000 ~ 0.004	0.001 ~ 0.012	0.004 ~ 0.028
60°S	< 0.001	0.000 ~ 0.001	< 0.001	< 0.001	0.000 ~ 0.001	0.000 ~ 0.002	0.000 ~ 0.006	0.000 ~ 0.015
70°S	< 0.001	< 0.001	< 0.001	< 0.001	< 0.001	< 0.001	0.000 ~ 0.002	0.000 ~ 0.005

Figure 3.1.1-5. Example sea-surface sun-glint reflectance variability in a 15° longitudal band (165°W–150°W) for the **March 21** HyspIRI orbit at (a) three levels of wind speed, which were used to compute sea-surface glint at (b) the west edge, (c) the middle point, and (d) the east edge of the HyspIRI field of view.
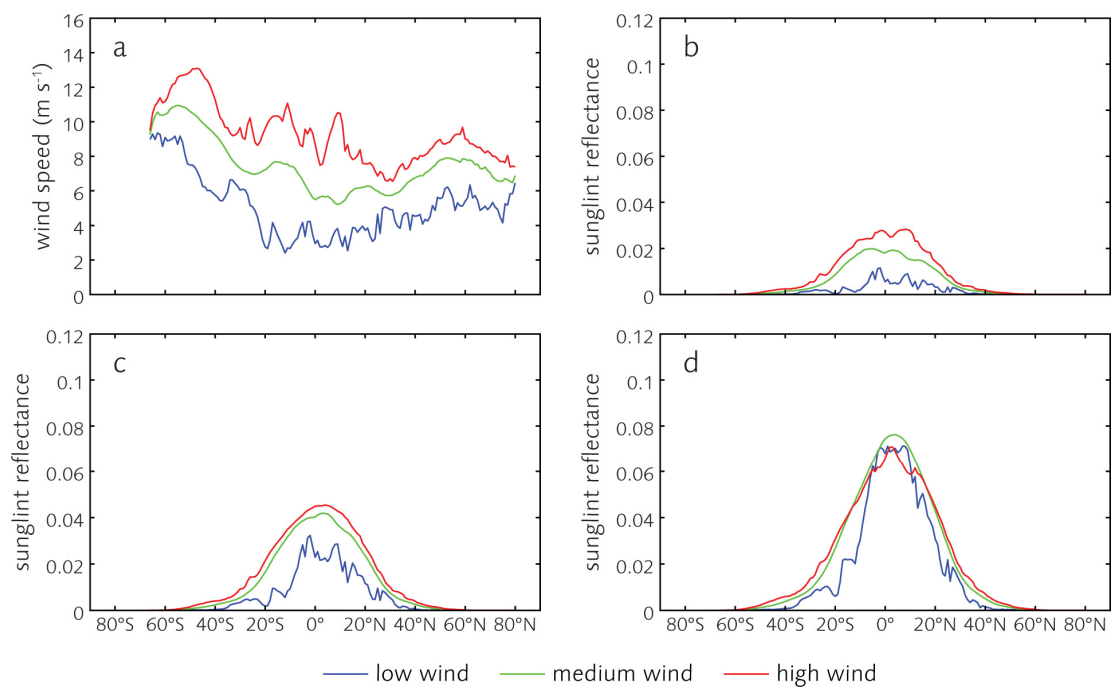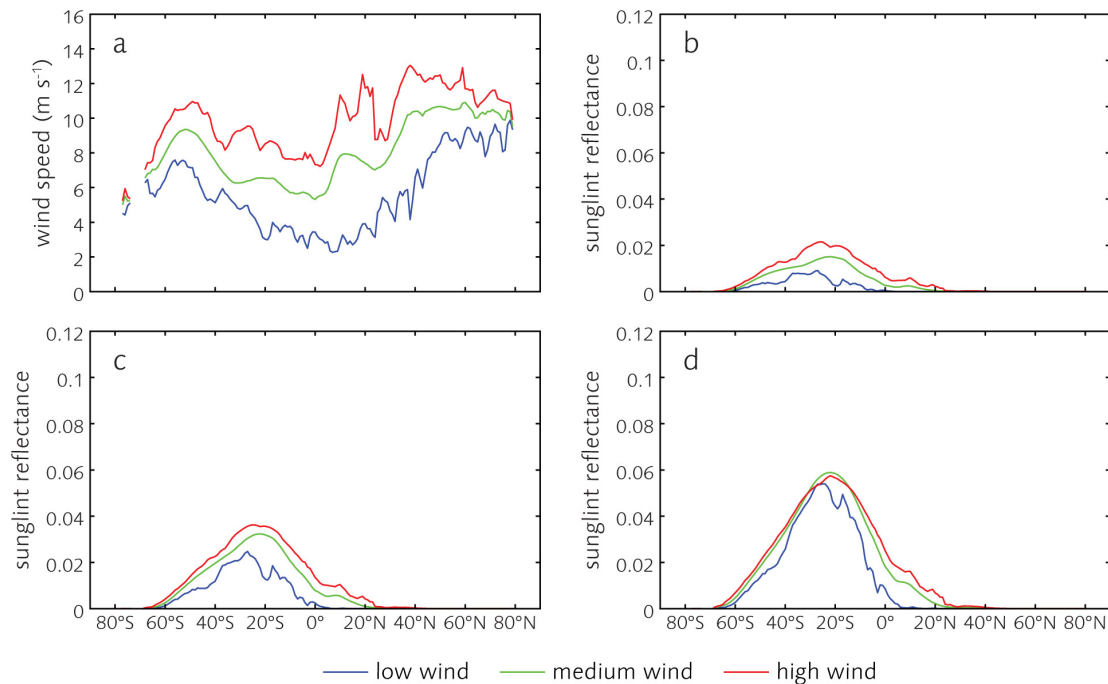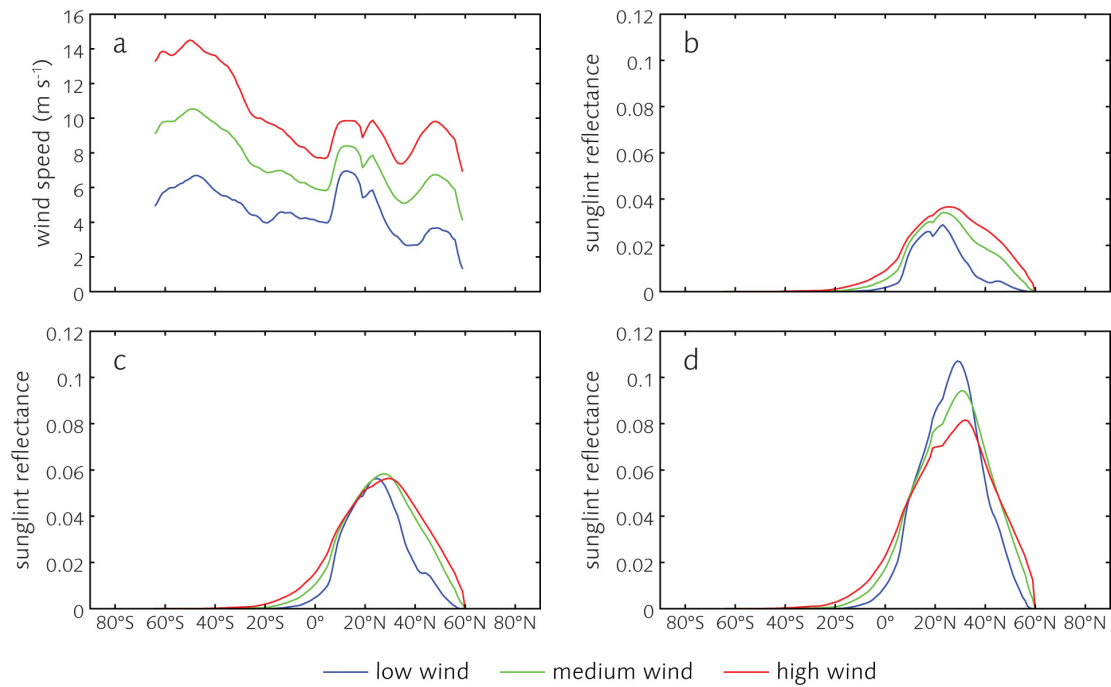
Figure 3.1.1-6. Example sea-surface sun-glint reflectance variability in a 15° longitudal band (165°W–150°W) for the **June 21** HyspIRI orbit at (a) three levels of wind speed, which were used to compute sea-surface glint at (b) the west edge, (c) the middle point, and (d) the east edge of the HyspIRI field of view.
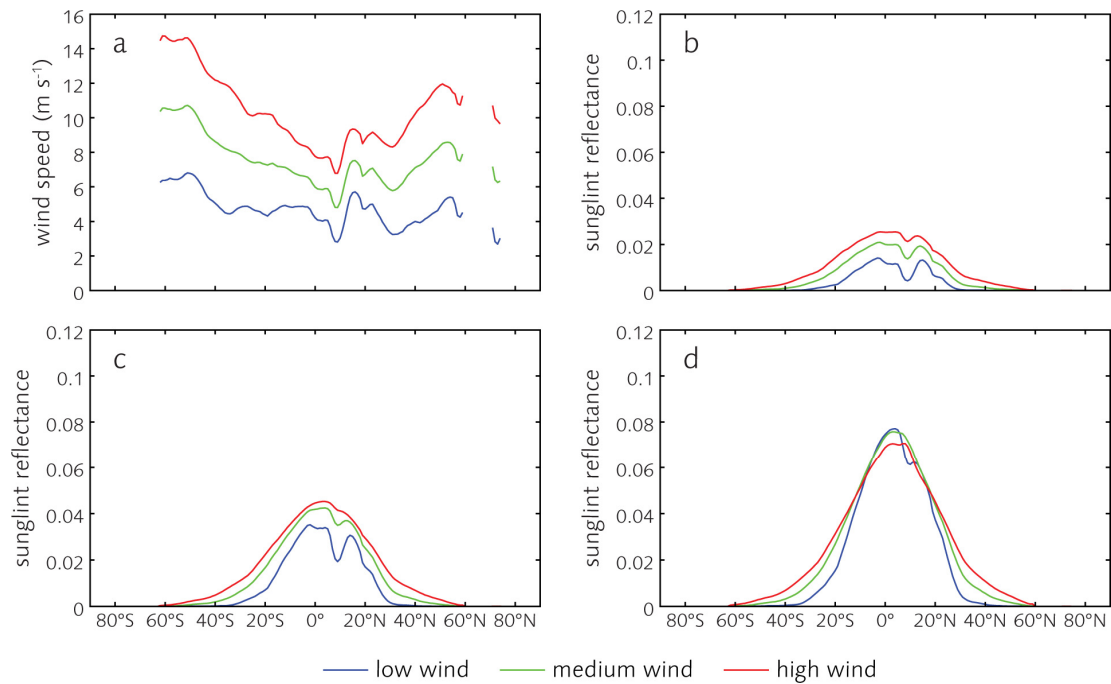
Figure 3.1.1-7. Example sea-surface sun-glint reflectance variability in a 15° longitudal band (165°W–150°W) for the **September 21** HyspIRI orbit at (a) three levels of wind speed, which were used to compute sea-surface glint at (b) the west edge, (c) the middle point, and (d) the east edge of the HyspIRI field of view.
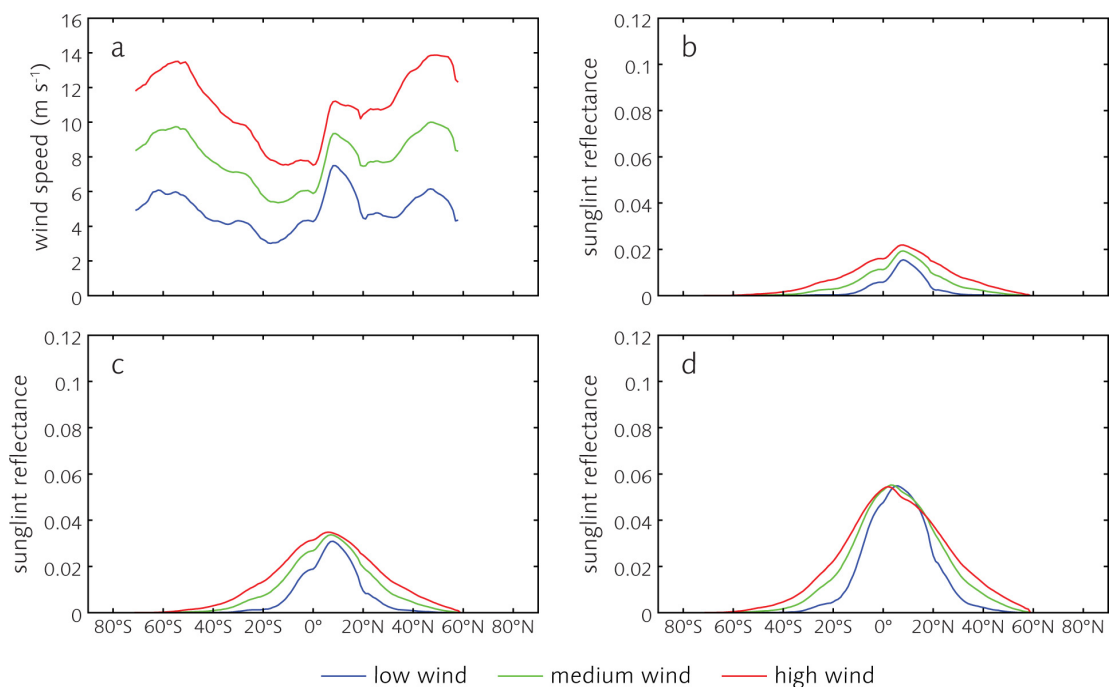
17
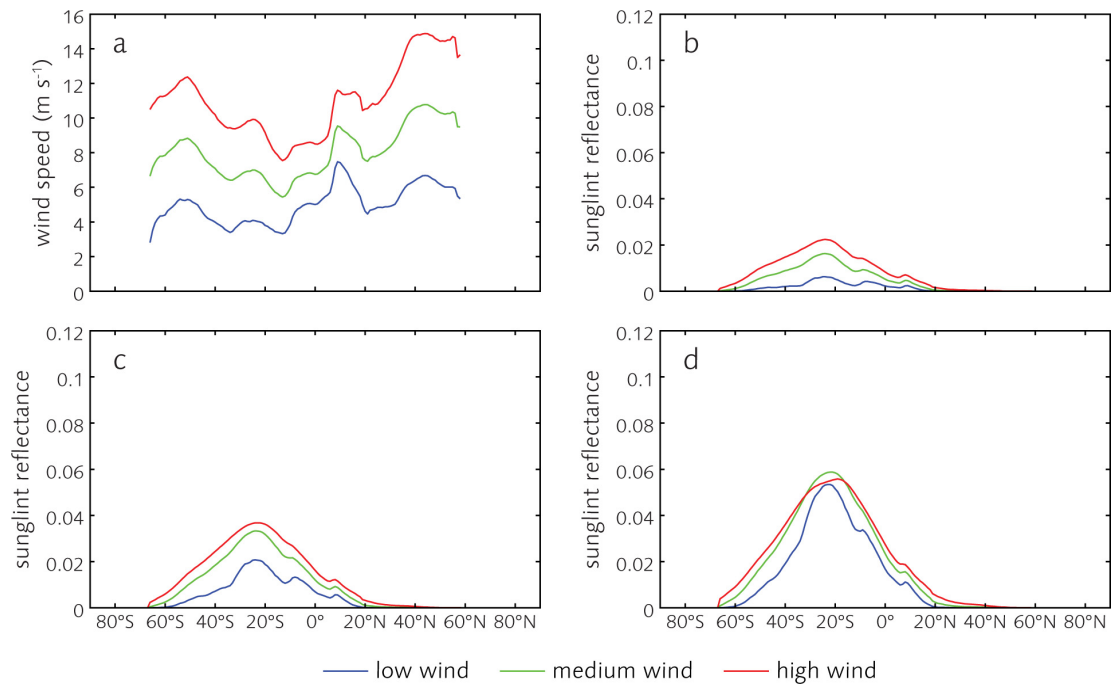
Figure 3.1.1-8. Example sea-surface sun-glint reflectance variability in a 15° longitudal band (165°W–150°W) for the **December 21** HyspIRI orbit at (a) three levels of wind speed, which were used to compute sea-surface glint at (b) the west edge, (c) the middle point, and (d) the east edge of the HyspIRI field of view.

Several summary observations can be made from the model results:

- The effect of latitude is very clear. Sun glint is stronger where the sun is high, because HyspIRI looks almost straight down. Sun-glint effects are apparent across a latitude band of 50° to 100° (i.e., 25°S–25°N to 50°S–50°N), depending on wind speed and the across-track pixel location.
- Sun glint is sensitive to wind speed for low to moderate glint strength and less sensitive for high glint.
- Sun glint at the east edge is consistently stronger (a factor of two) than at the west edge.
- Sun glint is high in summer due to high sun and low in winter due to low sun. At the equator in the middle point of the swath, sun-glint reflectance takes values of 0.025, 0.01, 0.04, and 0.01 for March, June, September, and December, respectively.
- Regional temporal variability appears similar to global longitudinal variability in magnitude.

3.1.2 Glint Reflectance: Sun/View Angles, Atmosphere, and Wind

This modeling activity utilizes HydroMod (integrated HydroLight and Modtran radiative transfer codes) to model the coupled water column and atmosphere system. Results provide information on glint reflectance intensity but also crucial information about water-leaving reflectance intensities. Importantly, HydroMod accurately models light fields for both optically shallow and

18

optically deep waters. Thus, it is possible to investigate the combined effects of atmospheric conditions, solar angles, view angles, water optical properties, and seafloor conditions (where desired) on the water-leaving signal and the potentially confounding glint signal.

The HydroLight radiative transfer model (Mobley et al. 1993, 1994; see www.hydrolight.info) computes radiance distributions and derived quantities for natural water bodies. In brief, HydroLight solves the scalar radiative transfer equation to compute the time-independent radiance distribution as a function of depth, direction, and wavelength within and leaving any plane-parallel water body. The upwelling radiance just above the sea surface includes both the water-leaving radiance and that part of the incident direct and diffuse sky radiance that is reflected upward by the wind-blown sea surface (glint radiance). The water-leaving and reflected-sky radiances are computed separately in order to isolate the water-leaving radiance, which is the quantity of interest in most remote sensing applications. Input to the model consists of the absorbing and scattering properties of the water body, the wind speed, the BRDF of the bottom of the water column, and the sun and sky radiance incident on the sea surface.

Modtran (Acharya et al. 1998; www.kirtland.af.mil/library/factsheets/factsheet.asp?id=7915) similarly computes spectral radiances within the atmosphere, given detailed information about the atmospheric constituents, the solar and viewing geometry, and the BRDF of the earth or sea surface at the lower boundary of the atmosphere.

In its standard form, HydroLight uses approximate semi-analytical models to obtain the incident spectral radiance onto the sea surface for a given solar zenith angle and atmospheric conditions. The incident radiance so computed is sufficiently accurate for most purposes of optical oceanography, such as computing remote-sensing reflectances or in-water irradiances. However, HydroLight's simple atmospheric models can neither simulate the full range of atmospheric conditions, nor can HydroLight propagate its water-leaving or surface-reflected radiances upward through the atmosphere. Modtran allows the user to select the BRDF of the land or water at the lower boundary of the atmosphere from several options defined by idealized analytic BRDFs. The only option for an ocean as the lower boundary is a Lambertian BRDF with a user-specified spectral irradiance reflectance. Modtran cannot compute the non-Lambertian BRDF corresponding to particular ocean conditions. Although both HydroLight and Modtran are considered industry standards for solving the unpolarized radiative transfer equation (RTE) with great accuracy within their respective oceanic and atmospheric domains, each is limited by its simplifying assumptions about the other domain.

To overcome the limitations of HydroLight and Modtran when run as separate codes, C. Mobley previously coupled HydroLight and Modtran into one package, called HydroMod. HydroMod is able to make round-trip radiative transfer simulations beginning with sunlight entering the top of the atmosphere, propagating through the atmosphere and into the ocean, propagating within and leaving the ocean, and finally returning to the top of the atmosphere. One complete HydroMod run generates the total radiance as measured for a single viewing direction and altitude, as seen by a satellite or aircraft-imaging sensor viewing a particular spot on the ocean. The at-sensor radiance includes ocean water-leaving and surface-reflected radiances transmitted through the atmosphere and atmospheric path radiance resulting from sunlight being scattered into the viewing direction between the sea surface and the sensor. These three contributions to the total

radiance are separately computed so that the total radiance can be partitioned into these contributions. All of the scattering and absorption effects within the ocean and atmosphere are computed just as in the separate codes. HydroMod is thus well suited for evaluation of airborne and satellite ocean color sensors.

The primary limitation of HydroMod is that it does not include polarization effects. Including polarization would require development of a vector version of HydroLight, then coupling that code with a vector atmospheric code such as 6SV (Kotchenova et al. 2006; http://6s.ltdri.org/). This would be a major project far beyond the scope of the Subgroup. Note that the lack of polarization code is an issue for many radiative transfer models that are routinely used for ocean and atmosphere studies. Thus, the Subgroup's use of HydroMod is in line with current practices of the wider research community.

The HyspIRI equatorial crossing data for March 21 were used to determine the sun and sensor geometry for the east and west edges of the HyspIRI scan (sensor off-nadir angles of 2° E and 10° W, perpendicular to the sensor flight direction; the solar zenith angle was 24.33°). The wind speed was 5 m s^{-1}. Modtran's default tropical atmosphere was used, with its various default values for marine aerosols, humidity, etc. The water index of refraction was a function of wavelength, although this is a small effect in the visible and near-IR wavelength range. These runs covered the range 350–1500 nm at 5-nm resolution.

Geometry of model input and output is an important consideration: incorrect geometries would produce much less meaningful results. Figure 3.1.2-1 illustrates the geometry used in the HydroMod simulations.

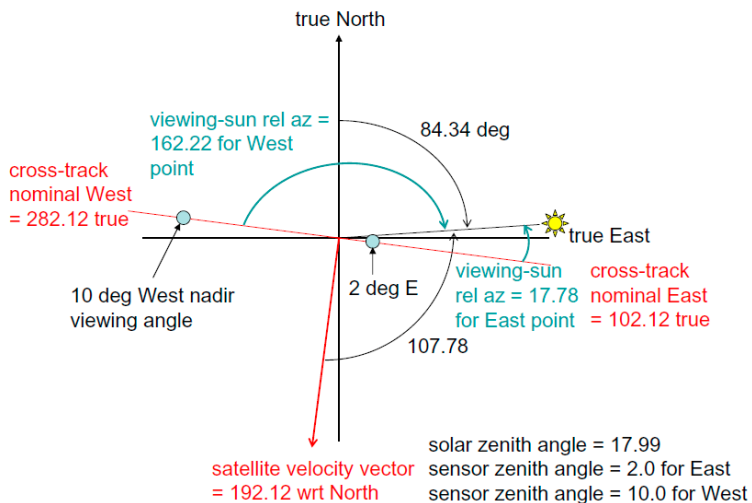**Figure 3.1.2-1.** Example geometry used in HydroMod simulations, in this case for Station ALOHA on June 21.

Two cases were simulated for in-water and bottom conditions:

1. Shallow-water, coral and sand bottom: Case 1 water with chlorophyll concentration of 0.3 mg m^{-3} in the "new Case 1" inherent optical properties (IOP) model of HydroLight version 5 (based on recent publications by Bricaud and Morel; see Mobley and Sundman

2008). In this model, all IOPs are determined by the chlorophyll value alone. The bottom was 50% sand and 50% coral at 5 m depth. This gives a large water-leaving radiance because of the clear water and relatively bright bottom.

2. Deep, dark ocean: Case 1 water with chlorophyll concentration of 5 mg m^{-3} and infinitely deep water. The high chlorophyll value and optically deep water together result in a much smaller water-leaving radiance.

Figure 3.1.2-2 shows the results for the shallow-water case, east edge of the HyspIRI field of view. The green line shows the water-leaving reflectance at the sea surface. This curve depends on both the water column optical properties and the bottom reflectance. The teal curve shows how much of the water-leaving reflectance (i.e., water-leaving radiance) actually reaches the top of the atmosphere (TOA). The red line shows the sea-surface glint reflectance (including both sun glint and sky glint, which are not separated in HydroMod). Note that the glint reflectance is almost independent of wavelength. (The small kinks near 1360 nm are due to Modtran numerical inaccuracies in the opaque atmospheric window where surface radiances are extremely small.) The purple curve shows how much of the surface glint makes it to the TOA. The orange curve shows the atmospheric path radiance at the TOA. This curve includes both Rayleigh and aerosol scattering contributions to the TOA path radiance. Finally, the blue curve shows the total TOA reflectance as would be measured by HyspIRI. (This curve is π times the TOA radiance divided by the TOA solar plane irradiance E_d.) The TOA ρ_u curve is the sum of the atmospheric and TOA glint and water-leaving curves.
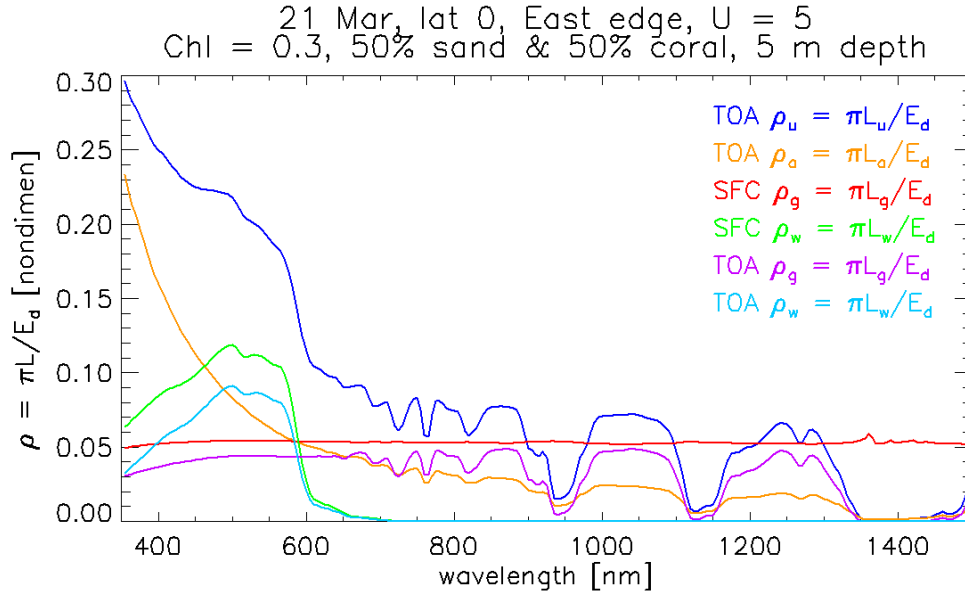
Figure 3.1.2-2. HydroMod results for the equator, March 21, shallow water, east-edge simulation.

Figure 3.1.2-3 compares the east and west edges of the HyspIRI field of view, with all other conditions the same as in Figure 3.1.2-2. It should be noted that the water-leaving reflectances are almost identical. However, the surface glint is much less for the west edge of the field of view because that viewing geometry picks up much less direct sun glint than the east edge. The

atmospheric contribution for the west edge is slightly greater than for the east edge, owing to the slightly longer atmospheric path length and different scattering angles from the sun's direct beam direction into the sensor.
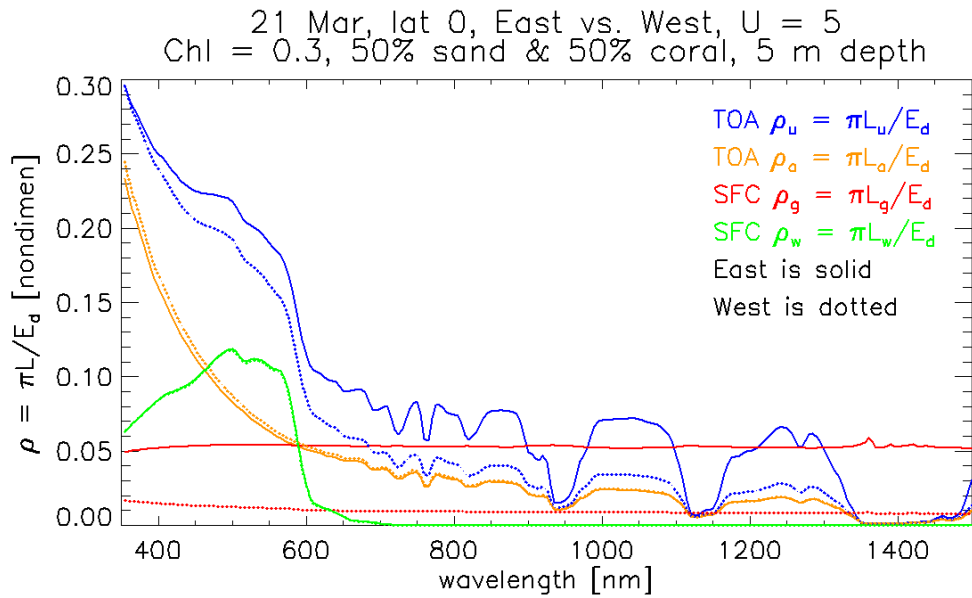
Figure 3.1.2-3. Same conditions as Figure 3.1.2-2 but including the west edge of the HyspIRI field of view.

Figure 3.1.2-4 corresponds to Figure 3.1.2-2, except that the chlorophyll concentration is 5.0 mg m^{-3} and the water is infinitely deep. The surface glint and atmospheric reflectances are almost identical. However, the water-leaving reflectance is now much less for the deep, high-chlorophyll ocean than for the shallow, clear water case.
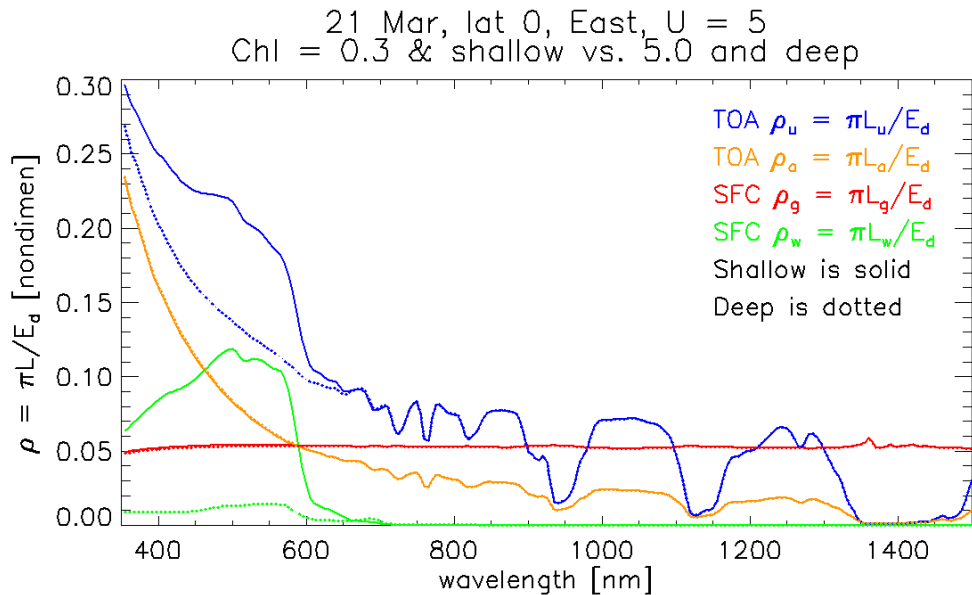
Figure 3.1.2-4. Same conditions as Figure 3.1.2-2 but including the high chlorophyll, optically deep case.

In summary, Figure 3.1.2-3 shows the large differences in glint reflectance that can occur from the east to the west edges of the HyspIRI field of view for moderate wind speeds in equatorial regions. Figure 3.1.2-4 shows the range of water-leaving reflectances that can occur for shallow clear waters with a mixed coral and sand bottom compared to deep, high-chlorophyll waters. In all of the examples, the remote-sensing problem is to start with any of the blue curves and retrieve the corresponding green curves after atmospheric and glint correction.

3.2   Glint Reflectance: Image Analysis

The objective here is to estimate glint radiances using remote-sensing imagery. This analysis utilizes seven scenes of AVIRIS high-altitude spectral imagery from the 2000 campaign in Hawaii (Figure 3.2-1).
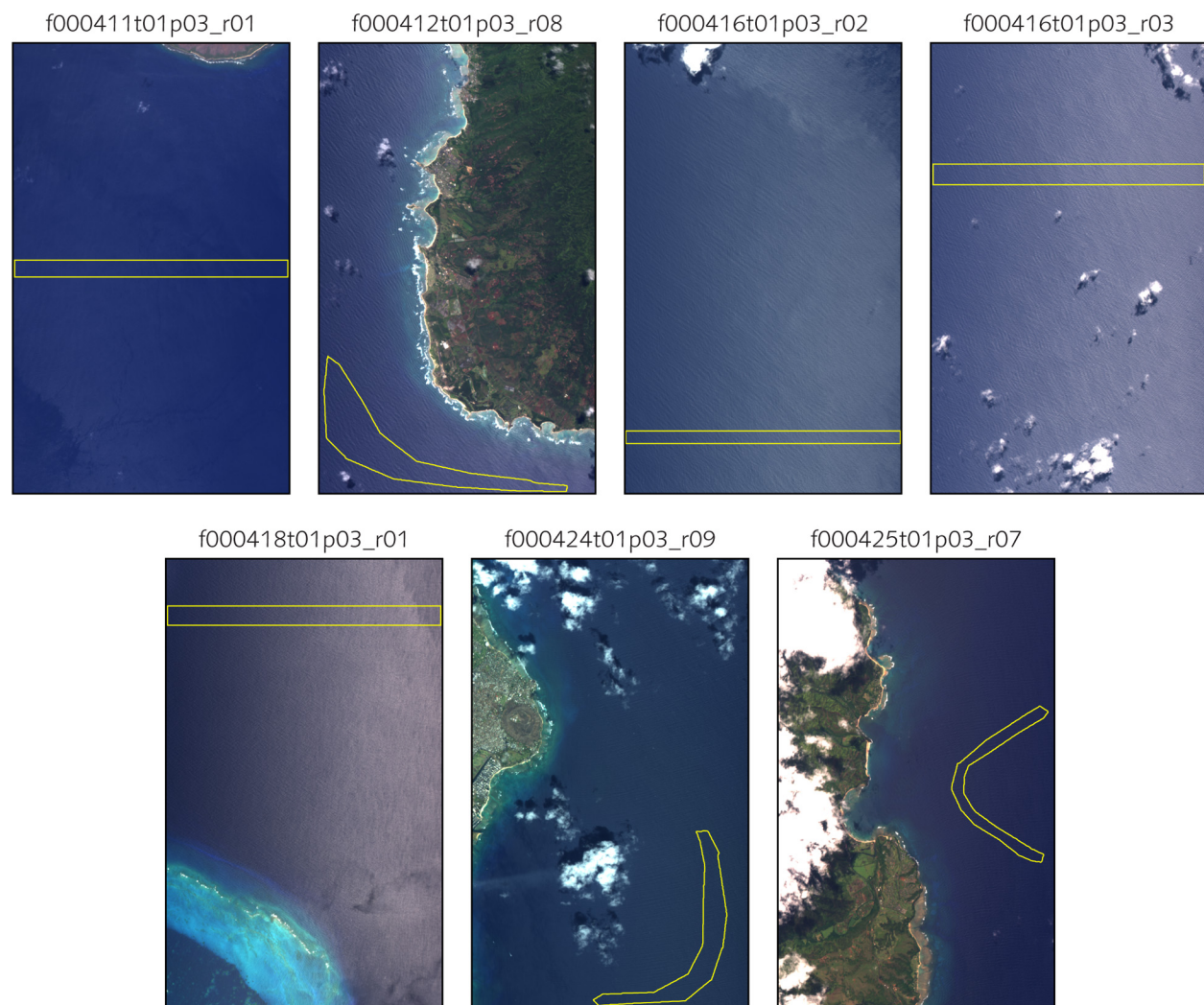
Figure 3.2-1. AVIRIS scenes used to estimate glint radiance for comparison with modeled values. These scenes are from the 2000 campaign in Hawaii. Yellow regions are deep-water areas used to extract glint statistics.

Assuming that a small area of deep ocean has uniform water-leaving reflectance, and also assuming that the same small area has uniform atmospheric absorbance and transmittance properties, then the variability in TOA measured reflectances must be due to variations in glint intensity in that small area. For this analysis, deep ocean areas were identified in each of the seven AVIRIS scenes, and TOA reflectance spectra were extracted for all pixels in the areas.

Within each area, the spectrum with the highest values represents the maximum observed glint intensity, and the spectrum with the lowest values represents the minimum observed glint intensity. Note that these maximum and minimum intensities are not globally absolute; they are only relative to the current area of interest. The difference between the maximum and minimum spectra represents the maximum range of glint reflectance in the area of interest, as observed at the TOA. Figure 3.2-2 shows this range for each of the seven AVIRIS scenes.
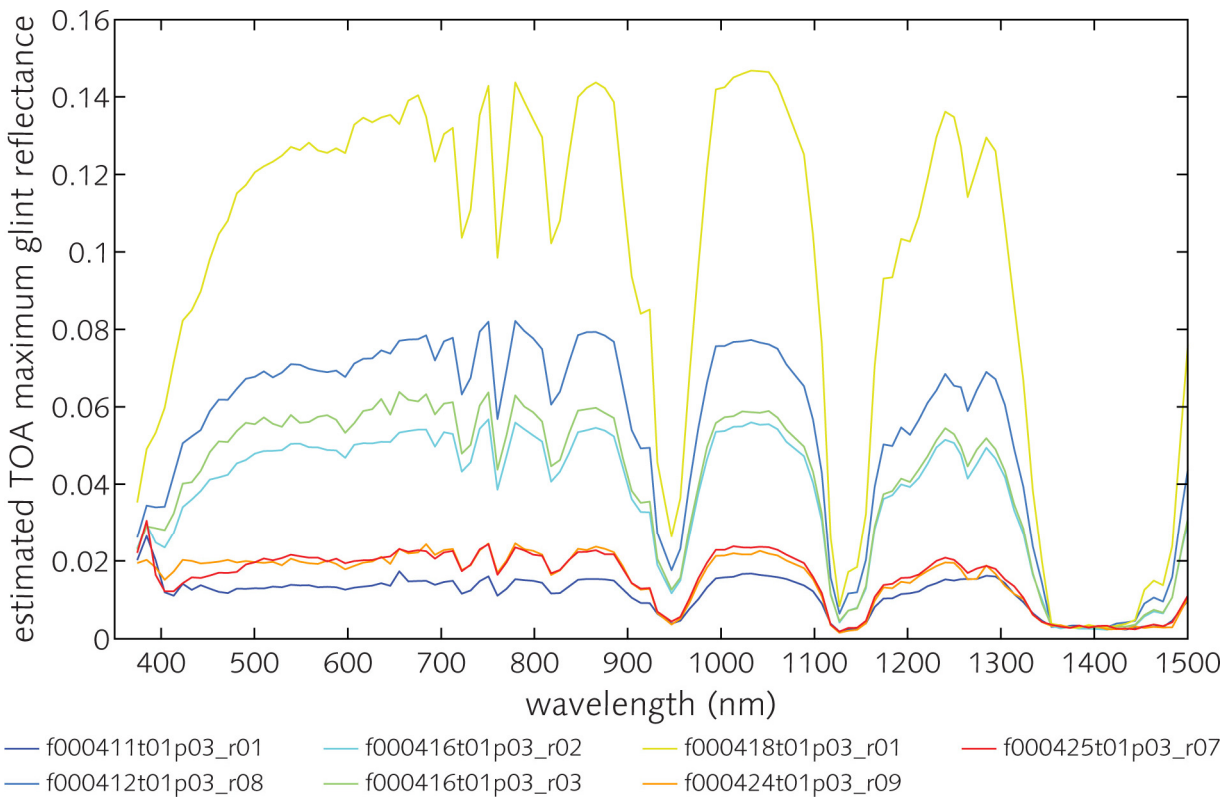
Figure 3.2-2. Estimated maximum glint reflectances for seven AVIRIS scenes.

The magnitude of glint reflectance varies with visually apparent sea surface glint intensity (see Figure 3.2-1). The high level of glint seen in AVIRIS scene f000418t01p03_r01 is demonstrative of the impact of sun and view angles on the glint signal.

TOA ρ_g can be separated from TOA ρ_a via simple algebraic decomposition (see Sections 4.3.2 and 5.5). In the NIR, the spectral shape of ρ_a is considerably steeper than that of ρ_g, which is nearly spectrally flat. At NIR wavelength λ, where water-leaving radiance is zero, the total reflectance minus Rayleigh reflectance gives the reflectance due to aerosol and glint (and their interaction):

$$\rho_{ga}(\lambda) = \rho_g(\lambda) + \rho_a(\lambda).$$

Assuming constant but different spectral shapes for the glint and aerosol components, glint and aerosol reflectances at one wavelength can be expressed as a function of their respective reflectances at a reference wavelength:

$$\rho_g(\lambda_1) = G \cdot \rho_g(\lambda_0) \text{ and } \rho_a(\lambda_1) = A \cdot \rho_a(\lambda_0),$$

where G and A are constants. Thus, with reflectances at two bands, the glint and aerosol reflectances can be solved by simple algebra.

Based on radiative transfer simulations of the conditions in AVIRIS scene f000418t01p03_r01, the following constants are set for analysis of that scene: $G = 0.95$, $A = 0.65$, $\lambda_0 = 1042$ nm and $\lambda_1 = 1553$ nm. Figure 3.2-3 shows the location of a cross-track sample extracted from the scene, and Figure 3.2-4 shows the ratio $\rho_{ga}(1042 \text{ nm}) / \rho_{ga}(1553 \text{ nm})$ along the cross-track line, as well as $\rho_g(1042)$ and $\rho_g(1042)$ along the cross-track line.
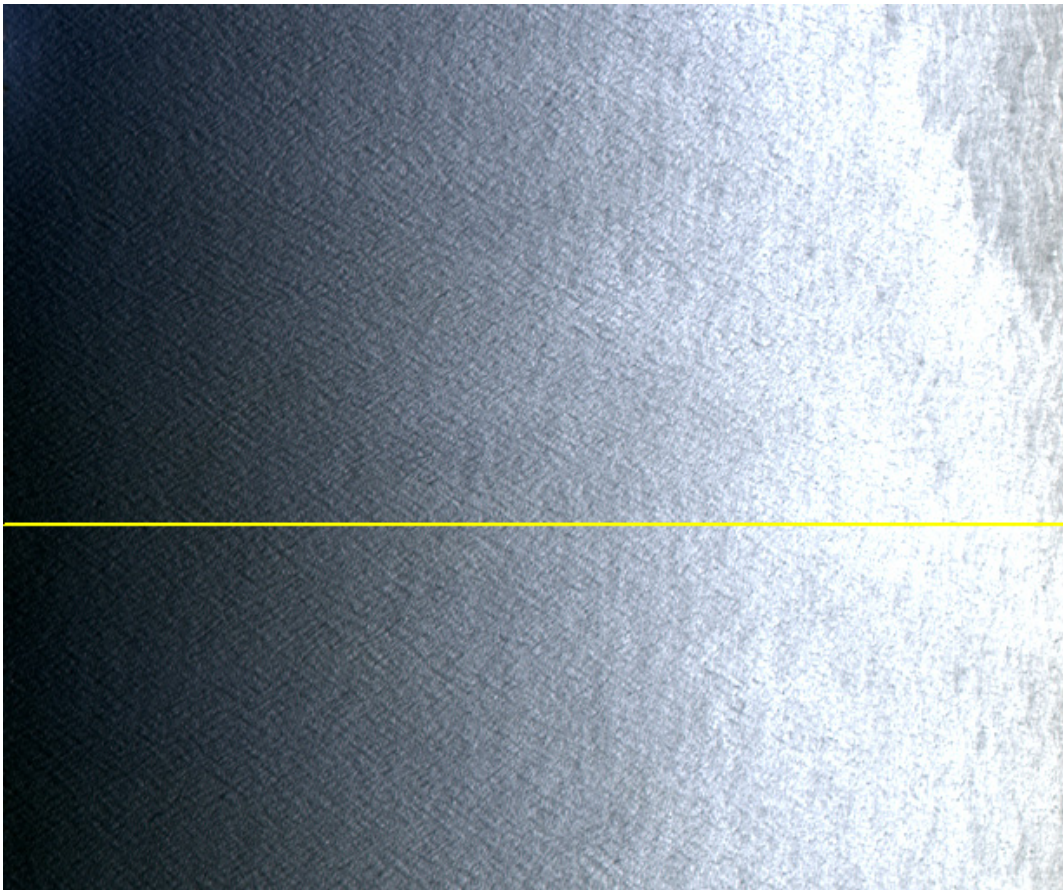
Figure 3.2-3. AVIRIS scene f000418t01p03_r01. The yellow line shows the location of the cross-track sample analyzed in Figure 3.2-4.
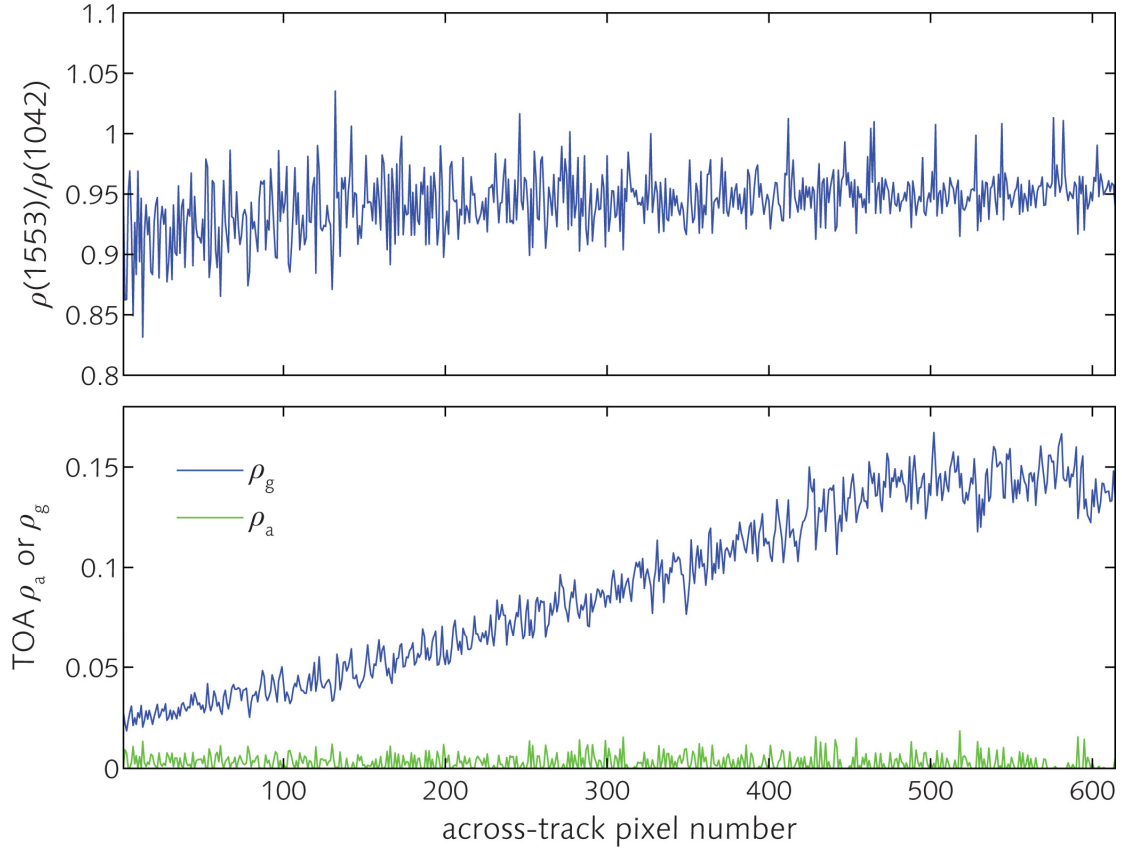
Figure 3.2-4. Discrimination between ρ_g and ρ_a. (Top) Ratio of TOA apparent reflectance at 1553 nm to TOA apparent reflectance at 1042 nm. (Bottom) Extracted ρ_g and ρ_a.

The reflectance ratio $\rho_{ga}(1553) / \rho_{ga}(1042)$ ranges from 0.9 at the left edge of the scene and quickly rises to ~0.95, where glint dominates over aerosol reflectance. The value 0.95 is consistent with radiative transfer simulations (not shown). ρ_a has a value ~0.003, while ρ_g ranges 0.02~0.15 in this scene: at least an order of magnitude higher than ρ_a. Note that a noisy reflectance ratio generates a noisy ρ_a. The noise level 0.005 in reflectance corresponds to $0.005 \times 65 \div \pi = 10\ \mu W\ cm^{-2}\ nm^{-1}\ sr^{-1}$ at 1042 nm. In practical image processing, since ρ_a varies at a much larger spatial scale than ρ_g, ρ_a can and should be smoothed first by spatial averaging. Then, the smoothed ρ_a can be used to derive ρ_g.

3.3   Summary

There are several key points to be taken from the model and image analysis:

(1)   Glint intensity can surpass that of water-leaving radiance;
(2)   Glint radiance is function of incident irradiance;
(3)   Glint reflectance is a function of the index of refraction of the water body; and
(4)   Glint reflectance at the sea surface, to the first order, is spectrally flat.

Point (4) is particularly important, because it is the basis for virtually all glint-correction strategies.

4   Glint Impact on HyspIRI Science
4.1   Coral Reefs

One science question for HyspIRI, as stated repeatedly in the NRC Decadal Survey (2007), is to determine the health and extent of coral reefs. The most common scientific approach to the question of coral reef health is to quantify the areal coverage of a reef by corals, various algae, and sediment. From the perspective of HyspIRI, the issue becomes one of accurate spectral discrimination between coral, algae, and sand (the predominant sediment on reefs). To investigate the impact of glint on retrievals of coral, algae, and sand, we conducted a modeling exercise using HydroLight.

The preferred method to evaluate spectral discrimination is through classification analysis. In classification analysis, a data set is used to train a classifier, which is then applied to the same or another data set to make predictions about class membership. The idea is to find the rates that spectra are predicted to belong to the correct class, as well as the rates that spectra are predicted to belong to the wrong class. These rates are very readily interpretable. For example, it is possible to say that coral is correctly predicted to be coral X% of the time, and coral is incorrectly predicted to be algae Y% of the time. The problem is obtaining the necessary data. At a minimum, the training data must have as many spectra as wavebands. Ideally, there should be hundreds to thousands of spectra for each class.

It is not reasonable to makes tens of thousands of HydroLight runs in the short time available to the HyspIRI Sun Glint Subgroup. So, an approximation was employed: run HydroLight for several different conditions with spectrally flat bottom reflectance, then interpolate between modeled values as needed. In all, HydroLight was run 5,832 times. In each run, one of the following parameters was varied among the listed values:

- Bottom reflectance: 0, 5, 10, 25, 65, 100%; spectrally flat
- Suspended chlorophyll: 0.05, 0.5, 1 mg m^{-3}
- $a_{CDOM}(440)$: 0, 0.15, 0.3 m^{-1}
- Suspended sand: 0, 0.5, 1 g m^{-3}
- Water depth: 0.5, 2, 5, 10 m
- Wind speed: 0, 5, 10 m s^{-1}
- Sun zenith: 20°, 30°, 40°

Output was taken for the following wavelengths and geometries:

- Wavelength: 355–995 nm in steps of 10 nm
- Sun azimuth wrt to along-track: 30°, 45°, 60°, 75°, 90°, 105°, 120°, 135°, 150°, 165°
- View zenith: 0°, 10°, 20°

Thus, there are values for water-leaving radiance (L_w), glint radiance (L_g), and downwelling irradiance (E_d) at each of the conditions specified by the 10 parameters (11,372,400 total values for each radiometric quantity).

The L_w, L_g, and E_d values have been assembled into three separate 10-dimensional arrays. These arrays are essentially look-up tables. With these arrays, it is possible to specify any bottom reflectance spectrum, suspended chlorophyll level, aCDOM(440), etc., then interpolate to get L_w, L_g, and E_d for the desired conditions and geometries. Several comparisons between interpolated values and explicitly modeled HydroLight values showed that results are nearly identical. However, for the present purposes, the aim is only to interpolate between bottom reflectances at condition values already in the arrays, not to interpolate between (for example) chlorophyll values.

Using the interpolation technique, it is possible to derive L_w, L_g and E_d under, for example, specific chlorophyll, CDOM, and sand conditions for 10,000 different bottom spectra in about 30 seconds. This affords the ability to use true multivariate analyses (namely, classification analysis) to explore the impact of glint on spectral separability of the classes. The current analysis utilizes reflectance spectra measured *in situ* for coral ($n = 4,005$), algae ($n = 5,500$), and sand ($n = 642$), and explores spectral separability of these bottom types under two different water and sun conditions, both without and with glint.

The first step is to interpolate at specified water, sun, and bottom reflectance conditions to generate appropriate L_w, L_g, and E_d spectra. In the coral reef case, each interpolation included coral, algae, and sand, for a total of 10,147 spectra. For each water/sun condition, interpolations were performed at four seafloor depths (0.5, 2, 5, and 10 m). The interpolation result for a single set of water/sun conditions totals 40,588 spectra. This is equivalent to running HydroLight 40,588 times, once for each bottom spectrum under the given water, sun, and depth conditions.

The next step is to build the classification functions. The objective here is not explicit radiative transfer inversion, where water column effects are derived and then subtracted from above-water spectra. Rather, we follow the implicit inversion approach put forward by Mobley and colleagues (Louchard et al. 2003; Mobley et al. 2005; Lesser and Mobley 2007) and Lee and colleagues (Lee et al. 1998, 1999, 2001, 2007). In this approach, above-water spectra are classified directly as combinations of bottom-type, water depth, and water optical properties. The difference is that, in the present case, classifications utilize class covariances and are based on statistical comparison with large samples, whereas the previous workers made single spectrum-to-spectrum comparisons. Thus, classes are not simply *coral, algae,* and *sand* but, rather, *coral-at-2-m-depth, algae-at-10-m-depth*, and so on.

Classification functions were based on remote-sensing reflectance, defined as

$$R_{rs} = L_w / E_d.$$

The classification functions were built <u>without</u> glint. Two coral reef scenarios were explored separately. Each scenario had coral, algae, and sand at four depths, resulting in 12 classes per scenario and 144 possible classification outcomes, as shown in Table 4.1-1.

Table 4.1-1. Matrix of possible classification outcomes. Cells labeled with a "C" indicate that the outcome is a correct classification. All other outcomes are incorrect classifications.

		ACTUAL CLASSES											
		coral 0.5 m	algae 0.5 m	sand 0.5 m	coral 2 m	algae 2 m	sand 2 m	coral 5 m	algae 5 m	sand 5 m	coral 10 m	algae 10 m	sand 10 m
PREDICTED CLASSES	coral 0.5 m	C											
	algae 0.5 m		C										
	sand 0.5 m			C									
	coral 2 m				C								
	algae 2 m					C							
	sand 2 m						C						
	coral 5 m							C					
	algae 5 m								C				
	sand 5 m									C			
	coral 10 m										C		
	algae 10 m											C	
	sand 10 m												C

The same R_{rs} spectra were used to test the classification. (Resubstitution has the potential to favorably bias the results, but with large data sets such as this, the bias is negligible.) Each spectrum was identified as belonging to one of the 144 outcomes, and the total count in each outcome was tallied in an error matrix similar to Table 4.1-1. Classification rates were calculated by dividing the number of spectra predicted to belong in a given class by the total number of spectra in the actual class (i.e., counts divided by column totals). To simplify interpretation, the 12×12 table was partitioned into nine 4×4 tables, arranged by actual and predicted classes. The idea is to more clearly show rates between the same bottom-type at different depths, as well as to highlight rates of misclassification.

Next, the same classification functions were applied to remote-sensing reflectance with glint, defined as

$$R_{rs,glint} = (L_w + L_g) / E_d.$$

That is, the $R_{rs,glint}$ data were classified using classification functions derived from R_{rs}. The objective is to see how glint impacts the classification. As before, results were tallied, converted to rates, then partitioned into 4×4 tables.

29

Again, this was done for two coral reef scenarios. The results for scenario #1 (clear water, sun zenith 20°, wind 5 m s^{-1}, sun azimuth 90°) are shown in Tables 4.1-2 and 4.1-3 for R_{rs} and $R_{rs,glint}$, respectively. The results for scenario #2 (turbid water, sun zenith 40°, wind 10 m s^{-1}, sun azimuth 30°) are shown in Tables 4.1-4 and 4.1-5 for R_{rs} and $R_{rs,glint}$, respectively. The complete conditions for each scenario are listed at the top of each table.

Summary interpretations of each table are as follows:

Table 4.1-2: Clear water, small sun zenith angle, no glint. Coral and algae are reasonably well separated. Interestingly, rates of correct classification increase with depth. Most misclassification is between depths within coral or algae, not between coral and algae. There is virtually no confusion with sand.

Table 4.1-3: Clear water, small sun zenith angle, glint. Correct classifications increase in spots and decrease markedly in others. Again, rates of correct classification are high at 10 m. Most confusion appears between 2-m and 5-m depths within coral or algae, not between coral and algae. There is virtually no confusion with sand. It is important to recall that classification functions were trained using glint-free R_{rs}.

Table 4.1-4: Turbid water, large sun zenith angle, no glint. Coral and algae are reasonably well separated to 5 m. At 10 m, coral/algae discrimination fails. Misclassification between algae and coral is higher than clear water (Table 4.1-2), especially at 5 m. There is virtually no confusion with sand.

Table 4.1-5: Turbid water, large sun zenith angle, glint. Coral and algae separation is very similar to the glint-free scenario (Table 4.1-4) to 5 m. At 10 m, coral is misclassified almost entirely as algae. Confusion with sand increases, but not markedly.

Tables are shown separately on the following pages.

Table 4.1-2. Classification rates in percent.

R_{rs} model: L_w / E_d
wavebands: 405–695 nm at 10 nm intervals
suspended chl: 0.05 mg m^{-3}
aCDOM(440): 0 m^{-1}
suspended sand: 0 g m^{-3}
sun azimuth wrt along track: 90°
sun zenith: 20°
view zenith: 10°
wind: 5 m s^{-1}

ACTUAL CLASS

PREDICTED CLASS	coral 0.5 m	coral 2 m	coral 5 m	coral 10 m
coral 0.5 m	84.3	0	0	0
coral 2 m	7.7	93.7	0	0
coral 5 m	0.1	1	90.5	1.6
coral 10 m	0.2	0.5	4.7	94.2

ACTUAL CLASS

PREDICTED CLASS	coral 0.5 m	coral 2 m	coral 5 m	coral 10 m
algae 0.5 m	1.9	0	0	0
algae 2 m	0.1	1.6	0	0
algae 5 m	3.3	2.7	2.8	0
algae 10 m	2.4	0.5	2	4.1

ACTUAL CLASS

PREDICTED CLASS	coral 0.5 m	coral 2 m	coral 5 m	coral 10 m
sand 0.5 m	0	0	0	0
sand 2 m	0	0	0	0
sand 5 m	0	0	0	0
sand 10 m	0	0	0	0

PREDICTED CLASS	algae 0.5 m	algae 2 m	algae 5 m	algae 10 m
coral 0.5 m	2.1	0	0	0
coral 2 m	0.1	1.6	0	0
coral 5 m	0	0.2	3.9	0.1
coral 10 m	0	0	0.7	6

PREDICTED CLASS	algae 0.5 m	algae 2 m	algae 5 m	algae 10 m
algae 0.5 m	82	0	0	0
algae 2 m	7.6	89.3	0.4	0
algae 5 m	8.1	8.7	94.7	0.7
algae 10 m	0	0	0.1	93.1

PREDICTED CLASS	algae 0.5 m	algae 2 m	algae 5 m	algae 10 m
sand 0.5 m	0.1	0	0	0
sand 2 m	0	0.1	0	0
sand 5 m	0	0	0.1	0
sand 10 m	0	0	0	0.1

PREDICTED CLASS	sand 0.5 m	sand 2 m	sand 5 m	sand 10 m
coral 0.5 m	0	0	0	0
coral 2 m	0	0	0	0
coral 5 m	0	0	0	0
coral 10 m	0	0	0	0

PREDICTED CLASS	sand 0.5 m	sand 2 m	sand 5 m	sand 10 m
algae 0.5 m	0	0	0	0
algae 2 m	0	0	0	0
algae 5 m	0	0	0	0
algae 10 m	0	0	0	0

PREDICTED CLASS	sand 0.5 m	sand 2 m	sand 5 m	sand 10 m
sand 0.5 m	100	0	0	0
sand 2 m	0	100	0	0
sand 5 m	0	0	100	0
sand 10 m	0	0	0	100

Table 4.1-3. Classification rates in percent.

$$R_{rs} \text{ model:} \quad (L_w + L_g) / E_d$$
wavebands: 405–695 nm at 10 nm intervals
suspended chl: 0.05 mg m^{-3}
aCDOM(440): 0 m^{-1}
suspended sand: 0 g m^{-3}
sun azimuth wrt along track: 90°
sun zenith: 20°
view zenith: 10°
wind: 5 m s^{-1}

ACTUAL CLASS

PREDICTED CLASS

	coral 0.5 m	coral 2 m	coral 5 m	coral 10 m
coral 0.5 m	95	0.4	0	0
coral 2 m	0	80.2	0	0
coral 5 m	0.5	15.4	90.8	1.5
coral 10 m	0	1.6	7.7	97.3

ACTUAL CLASS

	coral 0.5 m	coral 2 m	coral 5 m	coral 10 m
algae 0.5 m	1.5	0	0	0
algae 2 m	0	0.2	0	0
algae 5 m	0.1	0.5	0.7	0
algae 10 m	2.9	1.6	0.7	1.1

ACTUAL CLASS

	coral 0.5 m	coral 2 m	coral 5 m	coral 10 m
sand 0.5 m	0	0	0	0
sand 2 m	0	0	0	0
sand 5 m	0	0	0	0
sand 10 m	0	0	0	0

PREDICTED CLASS

	algae 0.5 m	algae 2 m	algae 5 m	algae 10 m
coral 0.5 m	3.1	0	0	0
coral 2 m	0	3	0	0
coral 5 m	0.1	2.1	8	0.2
coral 10 m	0	0.3	1.3	9.5

	algae 0.5 m	algae 2 m	algae 5 m	algae 10 m
algae 0.5 m	96.2	15.5	0	0
algae 2 m	0	31.7	0	0
algae 5 m	0.4	47.2	75.1	0.3
algae 10 m	0	0.2	15.5	89.9

	algae 0.5 m	algae 2 m	algae 5 m	algae 10 m
sand 0.5 m	0.1	0	0	0
sand 2 m	0	0.1	0	0
sand 5 m	0	0	0.1	0
sand 10 m	0	0	0	0.1

PREDICTED CLASS

	sand 0.5 m	sand 2 m	sand 5 m	sand 10 m
coral 0.5 m	0	0	0	0
coral 2 m	0	0	0	0
coral 5 m	0	0	0	0
coral 10 m	0	0	0	0

	sand 0.5 m	sand 2 m	sand 5 m	sand 10 m
algae 0.5 m	0	0	0	0
algae 2 m	0	0	0	0
algae 5 m	0	0	0	0
algae 10 m	0	0	0	0

	sand 0.5 m	sand 2 m	sand 5 m	sand 10 m
sand 0.5 m	100	0	0	0
sand 2 m	0	100	0	0
sand 5 m	0	0	100	0
sand 10 m	0	0	0	100

Table 4.1-4. Classification rates in percent.

R_{rs} model: L_w / E_d
wavebands: 405–695 nm at 10 nm intervals
suspended chl: 1 mg m^{-3}
aCDOM(440): 0.3 m^{-1}
suspended sand: 0.5 g m^{-3}
sun azimuth wrt along track: 30°
sun zenith: 40°
view zenith: 10°
wind: 10 m s^{-1}

ACTUAL CLASS

PREDICTED CLASS	coral 0.5 m	coral 2 m	coral 5 m	coral 10 m
coral 0.5 m	93.3	0	0	0
coral 2 m	1.2	94.4	0	0
coral 5 m	0	0.5	79.8	0
coral 10 m	0	0	0.6	48.2

ACTUAL CLASS

PREDICTED CLASS	coral 0.5 m	coral 2 m	coral 5 m	coral 10 m
algae 0.5 m	4.8	0	0	0
algae 2 m	0.4	4.9	0	0
algae 5 m	0	0	18.4	0
algae 10 m	0.2	0	0	51.8

ACTUAL CLASS

PREDICTED CLASS	coral 0.5 m	coral 2 m	coral 5 m	coral 10 m
sand 0.5 m	0	0	0	0
sand 2 m	0	0	0	0
sand 5 m	0	0	0	0
sand 10 m	0	0	1.2	0

PREDICTED CLASS	algae 0.5 m	algae 2 m	algae 5 m	algae 10 m
coral 0.5 m	1.5	0	0	0
coral 2 m	0	2	0	0
coral 5 m	0	0.1	4.4	0
coral 10 m	0	0	0.1	8.5

PREDICTED CLASS	algae 0.5 m	algae 2 m	algae 5 m	algae 10 m
algae 0.5 m	98.4	0	0	0
algae 2 m	0.1	97.5	0	0
algae 5 m	0	0.4	91.2	0
algae 10 m	0	0	2.7	91.3

PREDICTED CLASS	algae 0.5 m	algae 2 m	algae 5 m	algae 10 m
sand 0.5 m	0.1	0	0	0
sand 2 m	0	0.1	0	0
sand 5 m	0	0	0.1	0
sand 10 m	0	0	1.5	0.2

PREDICTED CLASS	sand 0.5 m	sand 2 m	sand 5 m	sand 10 m
coral 0.5 m	0	0	0	0
coral 2 m	0	0	0	0
coral 5 m	0	0	0	0
coral 10 m	0	0	0	0

PREDICTED CLASS	sand 0.5 m	sand 2 m	sand 5 m	sand 10 m
algae 0.5 m	0.3	0	0	0
algae 2 m	0	0	0	0
algae 5 m	0	0	0	0
algae 10 m	0	0	0	0

PREDICTED CLASS	sand 0.5 m	sand 2 m	sand 5 m	sand 10 m
sand 0.5 m	99.5	0	0	0
sand 2 m	0	100	0	0
sand 5 m	0.2	0	100	0
sand 10 m	0	0	0	100

Table 4.1-5. Classification rates in percent.

$$R_{rs} \text{ model:} \quad (L_w + L_g) / E_d$$

wavebands:	405–695 nm at 10 nm intervals
suspended chl:	1 mg m^{-3}
aCDOM(440):	0.3 m^{-1}
suspended sand:	0.5 g m^{-3}
sun azimuth wrt along track:	30°
sun zenith:	40°
view zenith:	10°
wind:	10 m s^{-1}

ACTUAL CLASS

PREDICTED CLASS

	coral 0.5 m	coral 2 m	coral 5 m	coral 10 m
coral 0.5 m	94	0	0	0
coral 2 m	2	98.2	0	0
coral 5 m	0	0.9	79.8	0
coral 10 m	0	0	1.4	3.2

ACTUAL CLASS

	coral 0.5 m	coral 2 m	coral 5 m	coral 10 m
algae 0.5 m	3.6	0	0	0
algae 2 m	0	0.8	0	0
algae 5 m	0	0.1	15	0
algae 10 m	0.3	0	0.5	96.7

ACTUAL CLASS

	coral 0.5 m	coral 2 m	coral 5 m	coral 10 m
sand 0.5 m	0	0	0	0
sand 2 m	0	0	0	0
sand 5 m	0	0	0	0
sand 10 m	0	0	3.2	0

PREDICTED CLASS

	algae 0.5 m	algae 2 m	algae 5 m	algae 10 m
coral 0.5 m	1.6	0	0	0
coral 2 m	0	4.6	0	0
coral 5 m	0	0.1	4	0
coral 10 m	0	0	0	0

	algae 0.5 m	algae 2 m	algae 5 m	algae 10 m
algae 0.5 m	98.2	0	0	0
algae 2 m	0	93.8	0	0
algae 5 m	0	1.3	86	0
algae 10 m	0	0	6.9	99.6

	algae 0.5 m	algae 2 m	algae 5 m	algae 10 m
sand 0.5 m	0.1	0	0	0
sand 2 m	0	0.1	0	0
sand 5 m	0	0	0.2	0
sand 10 m	0	0	2.9	0.4

PREDICTED CLASS

	sand 0.5 m	sand 2 m	sand 5 m	sand 10 m
coral 0.5 m	0	0	0	0
coral 2 m	0	0	0	0
coral 5 m	0	0	0	0
coral 10 m	0	0	0	0

	sand 0.5 m	sand 2 m	sand 5 m	sand 10 m
algae 0.5 m	0.2	0	0	0
algae 2 m	0	0	0	0
algae 5 m	0	0	0	0
algae 10 m	0	0	0	0

	sand 0.5 m	sand 2 m	sand 5 m	sand 10 m
sand 0.5 m	99.7	0	0	0
sand 2 m	0	99.7	0	0
sand 5 m	0.2	0.3	100	0
sand 10 m	0	0	0	100

Another interpretation approach is to consider that the predicted depth does not matter—only the predicted bottom type matters. This amounts to simply computing the column totals of the 4×4 partitioned tables. Thus, for example, it is possible to see how often *coral-0.5-m* is classified as *coral*. Those results are shown in Figures 4.1-1 and 4.1-2; for brevity, and because there is no problem with its discrimination, sand is not included in the figures.
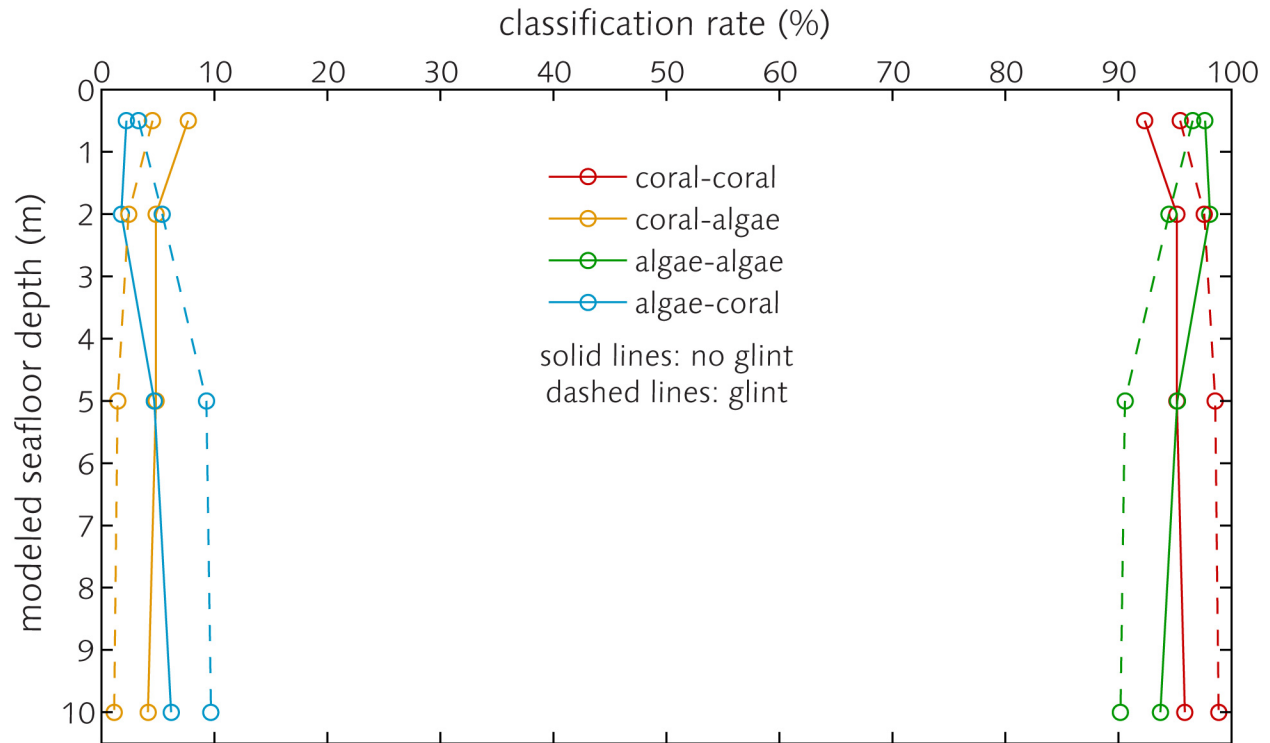

Figure 4.1-1. Classification rates for coral reef scenario #1 (conditions in Tables 4.1-2 and 4.1-3). Values indicate classification rates for specific bottom-type/depth combinations classified as bottom-type at any depth. Thus, for example, *coral-at-0.5-m* is classified as *coral-at-any-depth* approximately 92% of the time. Solid lines show results of R_{rs} modeled without glint (Table 4.1-2). Dashed lines show results of R_{rs} modeled with full glint (Table 4.1-3). Under the given water column and view conditions, glint actually increases the correct classification rate of coral at all depths, but it also increases the misclassification of algae as coral at all depths.
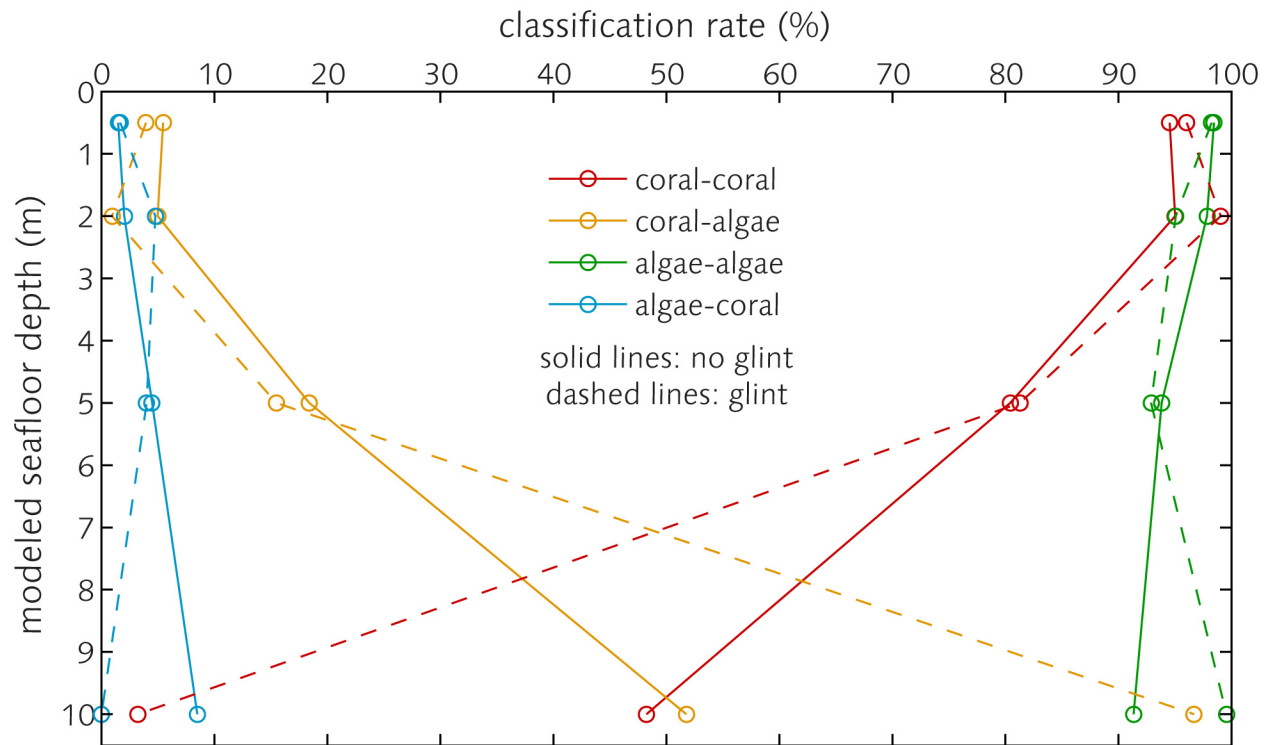
Figure 4.1-2. Classification rates for coral reef scenario #2 (conditions in Tables 4.1-4 and 4.1-5). Values indicate classification rates for specific bottom-type/depth combinations classified as bottom-type at any depth. Thus, for example, *coral-at-0.5-m* is classified as *coral-at-any-depth* approximately 93% of the time. Solid lines show results of R_{rs} modeled without glint (Table 4.1-4). Dashed lines show results of R_{rs} modeled with full glint (Table 4.1-5). Under these more turbid water column conditions, glint increases the correct classification rate of coral at 0.5 and 2 m, but greatly reduces correct coral classifications at 10 m.

The general conclusion, based on these simulations, is that glint does not markedly impact coral reef retrievals. Water clarity (or lack thereof) has a much greater impact.

4.2   Seagrass

Another important aquatic science focus for HyspIRI is detection and status of seagrass. In this case, the technical issue for HyspIRI reduces to discrimination between seagrass and sand. Since seagrass ecosystems often occur in the same regions as coral reefs, the same modeling approach as in Section 4.1 was used to investigate glint effects on seagrass retrievals. This analysis utilizes reflectance spectra measured *in situ* for sand ($n = 642$) and seagrass ($n = 263$). Results are detailed in Tables 4.2-1 through 4.2-2 on the following pages.

Table 4.2-1. Classification rates in percent.

$$R_{rs} \text{ model:} \quad L_w / E_d$$

wavebands:	405–695 nm at 10 nm intervals
suspended chl:	0.05 mg m^{-3}
aCDOM(440):	0 m^{-1}
suspended sand:	0 g m^{-3}
sun azimuth wrt along track:	90°
sun zenith:	20°
view zenith:	10°
wind:	5 m s^{-1}

ACTUAL CLASS

PREDICTED CLASS	seagr 0.5 m	seagr 2 m	seagr 5 m	seagr 10 m
seagr 0.5 m	94.7	0	0	0
seagr 2 m	4.6	97.7	0	0
seagr 5 m	0	1.5	95.8	0.8
seagr 10 m	0.8	0.8	4.2	99.2

ACTUAL CLASS

PREDICTED CLASS	seagr 0.5 m	seagr 2 m	seagr 5 m	seagr 10 m
sand 0.5 m	0	0	0	0
sand 2 m	0	0	0	0
sand 5 m	0	0	0	0
sand 10 m	0	0	0	0

PREDICTED CLASS	sand 0.5 m	sand 2 m	sand 5 m	sand 10 m
seagr 0.5 m	0	0	0	0
seagr 2 m	0	0	0	0
seagr 5 m	0	0	0	0
seagr 10 m	0	0	0	0

PREDICTED CLASS	sand 0.5 m	sand 2 m	sand 5 m	sand 10 m
sand 0.5 m	100	0	0	0
sand 2 m	0	100	0	0
sand 5 m	0	0	100	0
sand 10 m	0	0	0	100

Table 4.2-2. Classification rates in percent.

$$R_{rs} \text{ model:} \quad (L_w + L_g) / E_d$$

wavebands:	405–695 nm at 10 nm intervals
suspended chl:	0.05 mg m^{-3}
aCDOM(440):	0 m^{-1}
suspended sand:	0 g m^{-3}
sun azimuth wrt along track:	90°
sun zenith:	20°
view zenith:	10°
wind:	5 m s^{-1}

ACTUAL CLASS

PREDICTED CLASS

	seagr 0.5 m	seagr 2 m	seagr 5 m	seagr 10 m
seagr 0.5 m	98.9	0	0	0
seagr 2 m	1.1	96.6	0	0
seagr 5 m	0	3.4	100	23.2
seagr 10 m	0	0	0	76.8

ACTUAL CLASS

	seagr 0.5 m	seagr 2 m	seagr 5 m	seagr 10 m
sand 0.5 m	0	0	0	0
sand 2 m	0	0	0	0
sand 5 m	0	0	0	0
sand 10 m	0	0	0	0

PREDICTED CLASS

	sand 0.5 m	sand 2 m	sand 5 m	sand 10 m
seagr 0.5 m	0	0	0	0
seagr 2 m	0	0	0	0
seagr 5 m	0	0	0	0
seagr 10 m	0	0	0	0

	sand 0.5 m	sand 2 m	sand 5 m	sand 10 m
sand 0.5 m	100	0	0	0
sand 2 m	0	100	0	0
sand 5 m	0	0	100	0
sand 10 m	0	0	0	100

Table 4.2-3. Classification rates in percent.

$$R_{rs} \text{ model:} \quad L_w / E_d$$

wavebands: 405–695 nm at 10 nm intervals
suspended chl: 1 mg m^{-3}
aCDOM(440): 0.3 m^{-1}
suspended sand: 0.5 g m^{-3}
sun azimuth wrt along track: 30°
sun zenith: 40°
view zenith: 10°
wind: 10 m s^{-1}

ACTUAL CLASS

PREDICTED CLASS	seagr 0.5 m	seagr 2 m	seagr 5 m	seagr 10 m
seagr 0.5 m	95.4	0	0	0
seagr 2 m	4.6	99.6	0	0
seagr 5 m	0	0.4	97.7	0
seagr 10 m	0	0	1.9	100

ACTUAL CLASS

PREDICTED CLASS	seagr 0.5 m	seagr 2 m	seagr 5 m	seagr 10 m
sand 0.5 m	0	0	0	0
sand 2 m	0	0	0	0
sand 5 m	0	0	0	0
sand 10 m	0	0	0.4	0

PREDICTED CLASS	sand 0.5 m	sand 2 m	sand 5 m	sand 10 m
seagr 0.5 m	0	0	0	0
seagr 2 m	0	0	0	0
seagr 5 m	0	0	0	0
seagr 10 m	0	0	0	0

PREDICTED CLASS	sand 0.5 m	sand 2 m	sand 5 m	sand 10 m
sand 0.5 m	100	0	0	0
sand 2 m	0	100	0	0
sand 5 m	0	0	100	0
sand 10 m	0	0	0	100

Table 4.2-4. Classification rates in percent.

$$R_{rs} \text{ model:} \quad (L_w + L_g) / E_d$$

wavebands: 405–695 nm at 10 nm intervals
suspended chl: 1 mg m^{-3}
aCDOM(440): 0.3 m^{-1}
suspended sand: 0.5 g m^{-3}
sun azimuth wrt along track: 30°
sun zenith: 40°
view zenith: 10°
wind: 10 m s^{-1}

ACTUAL CLASS

PREDICTED CLASS

	seagr 0.5 m	seagr 2 m	seagr 5 m	seagr 10 m
seagr 0.5 m	97	0	0	0
seagr 2 m	3	100	0	0
seagr 5 m	0	0	99.6	0
seagr 10 m	0	0	0.4	100

ACTUAL CLASS

	seagr 0.5 m	seagr 2 m	seagr 5 m	seagr 10 m
sand 0.5 m	0	0	0	0
sand 2 m	0	0	0	0
sand 5 m	0	0	0	0
sand 10 m	0	0	0	0

PREDICTED CLASS

	sand 0.5 m	sand 2 m	sand 5 m	sand 10 m
seagr 0.5 m	0	0	0	0
seagr 2 m	0	0	0	0
seagr 5 m	0	0	0	0
seagr 10 m	0	0	0	3

	sand 0.5 m	sand 2 m	sand 5 m	sand 10 m
sand 0.5 m	100	0	0	0
sand 2 m	0	100	0	0
sand 5 m	0	0	100	0
sand 10 m	0	0	0	97

The only confusion between seagrass and sand occurs under turbid water conditions at the greatest depth modeled (10 m) with glint included. However, the confusion rate is very small: only 3%. ***The general conclusion is that glint does not impact seagrass retrievals, even under turbid water conditions.***

4.3   Station ALOHA Simulation
4.3.1   Forward Modeling

Further HydroMod simulations were performed to investigate the impact of glint on retrieval of suspended chlorophyll concentrations. This exercise was based on very clear oligotrophic oceanic conditions typically encountered at Station ALOHA, north of Oahu, Hawaii. The idea is simply to model conditions at Station ALOHA along the west and east edges of the HyspIRI scan-line, then attempt to retrieve subsurface chlorophyll values in the presence of glint, as well as after performing a glint-correction procedure. This represents somewhat of a worst-case scenario in that the target (clear, deep ocean) is very dark, which means that glint reflectance can be greater than the water-leaving reflectance signal.

HydroMod was parameterized as follows:

- Location: Station ALOHA, 22°45'N, 158°W
- Date: June 21
- Sun Azimuth wrt Along Track: 107.78°
- Sun Zeinth: 17.99°
- Suspended Chlorophyll: 0.05 μg l^{-1}
- Wind Speed: two values modeled, 0 and 10 m s^{-1}
- Atmosphere Conditions: Clear sky with marine aerosols
- Bottom Boundary: Infinitely deep ocean

To generate water column IOPs for HydroLight, the "new Case 1" IOP model in HydroLight v. 5 was used. Atmospheric conditions were modeled as Modtran's defaults for tropical atmosphere with marine aerosols. The geometry in these HydroMod simulations was similar to the previous glint characterization simulations illustrated in Figures 3.1.2-1 through 3.1.2-4.

The HydroMod runs were chosen to show the extremes of viewing direction (east and west edges of the HyspIRI field of view) and wind speed (calm and rough sea surface, U = 0 m s^{-1} and U = 10 m s^{-1}, respectively). The results of these four simulations are shown in Figure 4.3.1-1.
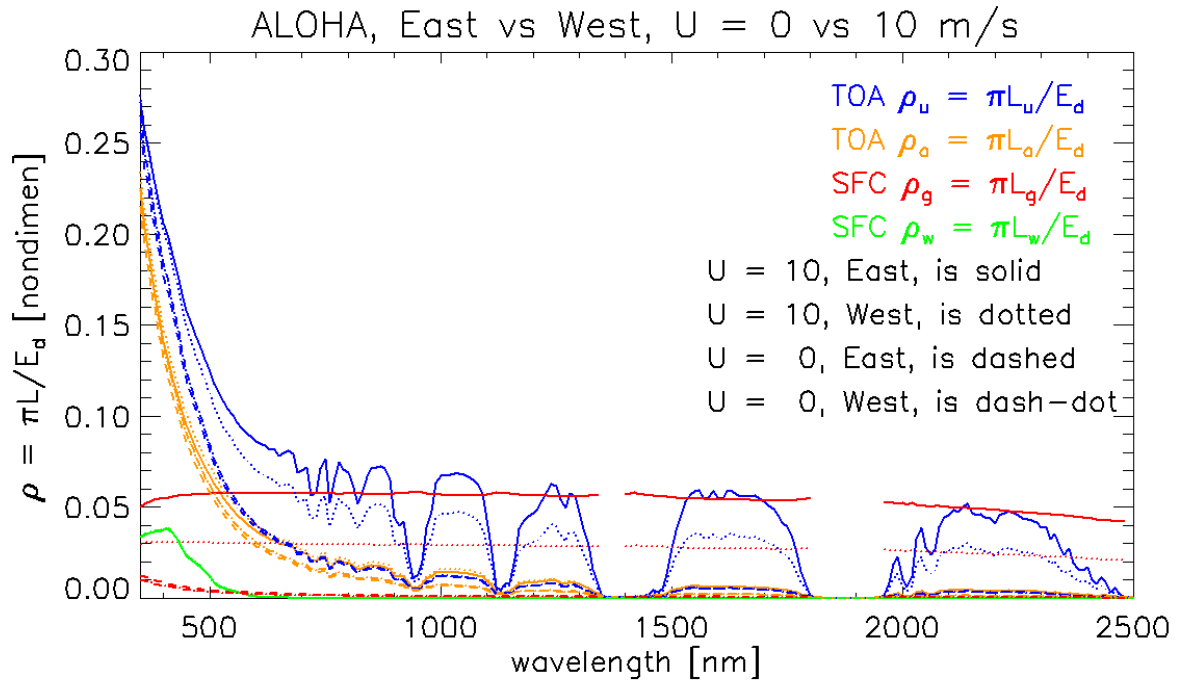
Figure 4.3.1-1. HydroMod simulations for station ALOHA.

There are several notable features in Figure 4.3.1-1. First, the water-leaving reflectances (green lines) at the sea surface are almost indistinguishable because apparent optical properties like ρ_w are insensitive to external environmental conditions such as sun angle and wind speed. The glint reflectances (red) for U = 0 m s^{-1} (a level surface) are small and almost identical because these are background sky reflectances with no direct sun glitter. However, for U = 10 m s^{-1}, the glint reflectances are large because the sea surface is rough, which means that some wave facets will produce direct sun glint. The east edge of the HyspIRI field of view (solid red) has roughly twice the glint as the west edge because the east edge is looking closer to the center of the glitter pattern. The surface glint reflectances are not plotted in the opaque atmospheric regions near 1350, 1800, and 2500 nm because the extremely low irradiances reaching the sea surface in these bands makes the Modtran calculations at the sea surface inaccurate. The TOA atmospheric path reflectances (orange) do not depend strongly on the atmospheric path differences in the east vs. west viewing directions (solid vs. dotted and dashed vs. dash-dot curves). However, the atmospheric reflectances do depend somewhat on the wind speed (upper pair of orange curves vs. lower pair) because of differences in the aerosols in the atmosphere, which depend on the 24-hour wind speed. The blue curves show the total TOA reflectances as would be measured by HyspIRI. Note that, as shown previously in Figure 3.1.2-2, the surface ρ_w and ρ_g curves plotted in Figure 4.3.1-1 are not the contributions of ρ_w and ρ_g to the TOA reflectances ρ_u because of atmospheric effects as the surface radiances are transmitted to the TOA.

4.3.2   Radiometric Inversion of Simulation Data

The HydroMod simulation data for Station ALOHA are used to investigate a possible implementation of a glint correction algorithm in a per-pixel atmospheric correction procedure.

The atmosphere-glint correction methodology is described and its application to the simulated data follows below.

Satellite-measured reflectance at the top of the atmosphere (ρ_t) is decomposed as follows:

$$\rho_t = \rho_{atm}^{TOA} + \rho_{glint}^{TOA} + \rho_w^{TOA},$$
(4.3.2-1)

where ρ_{atm}^{TOA} is atmospheric path reflectance; ρ_{glint}^{TOA} is the glint reflectance due to photons reflecting off the sea surface; and ρ_w^{TOA} is the water-leaving radiance contribution to the TOA reflectance (Gao et al. 2000). It is often useful to distinguish the Rayleigh (ρ_r) and aerosol (ρ_a, which includes Rayleigh-aerosol interaction) reflectances since the Rayleigh contribution is estimated with given atmospheric pressure while the aerosol contribution is unknown *a priori*:

$$\rho_{atm}^{TOA} = \rho_r + \rho_a.$$
(4.3.2-2)

Direct sun glint at the surface is highly variable, depending on the sea surface slope distribution (or wind speed) and viewing geometry as described in Section 3.1. In contrast, sky glint at the TOA varies depending on atmospheric molecules and aerosols with almost no dependency on the sea surface slope distribution. Sky glint is expected to be much less variable than sun glint, and therefore it can be reasonably estimated using radiative transfer simulations. Taking advantage of this *a priori* estimation of the sky glint contribution, it can be eliminated from the TOA reflectance. To do this, the two glint components are separated:

$$\rho_{glint}^{TOA} = \rho_g^{TOA} + \rho_{sky}^{TOA}.$$
(4.3.2-3)

The TOA water-leaving reflectance (ρ_w^{TOA}) is related to the sea surface water-leaving reflectance (ρ_w^{SFC}) as follows (Gao et al. 2000):

$$\rho_w^{TOA} = \frac{\rho_w^{SFC} \cdot T_{gas} \cdot t_d \cdot t_u}{1 - s \cdot \rho_w^{SFC}},$$
(4.3.2-4)

where T_{gas} is a two-way atmospheric gas transmittance; t_d and t_u are the downward and upward transmittances, respectively, due to the atmosphere; and s is the spherical albedo of the atmosphere for upward radiance. Combining the above equations produces

$$\rho_t = \rho_r + \rho_a + \rho_{sky}^{TOA} + \rho_g^{TOA} + \frac{\rho_w^{SFC} \cdot T_{gas} \cdot t_d \cdot t_u}{1 - s \cdot \rho_w^{SFC}}.$$
(4.3.2-5)

The goal of the atmosphere-glint correction procedure is to derive ρ_w^{SFC} from ρ_t. All other variables in equation (4.3.2-5) must be determined. Some variables (T_{gas}, ρ_r) are computed by radiative transfer simulations with ancillary inputs such as ozone, water vapor, and atmospheric pressure. Other variables such as ρ_{sky}^{TOA}, t_d, t_u, and s vary with aerosols to a certain degree. These variables are assumed to be known in this exercise; in practice, these may need to be refined by

an iterative approach. The remaining two terms, ρ_a and ρ_g^{TOA} are highly dependent on aerosols and sea surface slope distribution and, therefore, these are key parameters to be determined in the atmosphere-glint correction procedure.

The aerosol and glint retrieval here is performed on wavelengths longer than 1000 nm, then extrapolated to visible wavelengths. At wavelengths longer than 1000 nm, where water-leaving reflectance is negligible, equation (4.3.2-5) reduces to

$$\rho_t - \rho_r - \rho_{sky}^{TOA} = \rho_a + \rho_g^{TOA}. \tag{4.3.2-6}$$

The left-hand side can be easily computed as described above, while the right-hand side (aerosol and glint reflectances) must be derived. A simple approach is given here to spectrally decompose the aerosol and glint contribution. The glint reflectance spectral shape, $G(\lambda)$, and the aerosol reflectance spectral shape, $A(\lambda)$, are defined by normalization at a reference wavelength λ_0:

$$\rho_a(\lambda) = \rho_{a0} \cdot A(\lambda) \ \text{and} \ \rho_g^{TOA}(\lambda) = \rho_{g0} \cdot G(\lambda), \tag{4.3.2-7}$$

where ρ_{a0} and ρ_{g0} are the aerosol and glint reflectances at wavelength, λ_0. $A(\lambda)$ and $G(\lambda)$ are obtained using radiative transfer simulations. Then, equations (4.3.2-6) and (4.3.2-7) can be solved for ρ_{a0} and ρ_{g0} from two-band data by simple algebraic manipulation. The aerosol and glint reflectances are extrapolated to the visible and subtracted from the total reflectance according to equation (4.3.2-5).

Youngje Park applied the above-described atmospheric-glint correction algorithm to the HydroMod simulated TOA data for the ALOHA-East edge case. Figure 4.3.2-1 shows the input spectra for the atmospheric correction for the ALOHA-East edge, $U = 10$ m s^{-1} simulation, which includes HydroMod-generated TOA reflectance and some pre-computed atmospheric correction variables: Rayleigh reflectance, sky glint reflectance, and aerosol and glint reflectance shapes. The Rayleigh reflectance and the aerosol spectra were computed using MODTRAN5 (Berk et al. 2008) with almost identical input conditions as the forward modeling (see Section 4.3.1) to minimize errors due to differences in the Rayleigh reflectance and aerosol models. All other parameters were computed using the 6Sv1 code (Vermote et al. 1997) with the following input conditions:

- Solar zenith/azimuth: 17.99°/107.78°
- Sensor zenith/azimuth: 2°/-90°
- Atmosphere profile: tropical
- Aerosols: optical thickness 0.2 at 550 nm, maritime model with 70% relative humidity
- Wind speed: 5 m s^{-1} (different from the forward modeled $U = 10$ m s^{-1})

$A(\lambda)$ and $G(\lambda)$ are different and vary smoothly in the NIR-SWIR range. Aerosol reflectance decreases with wavelength, while glint reflectance is rather flat.
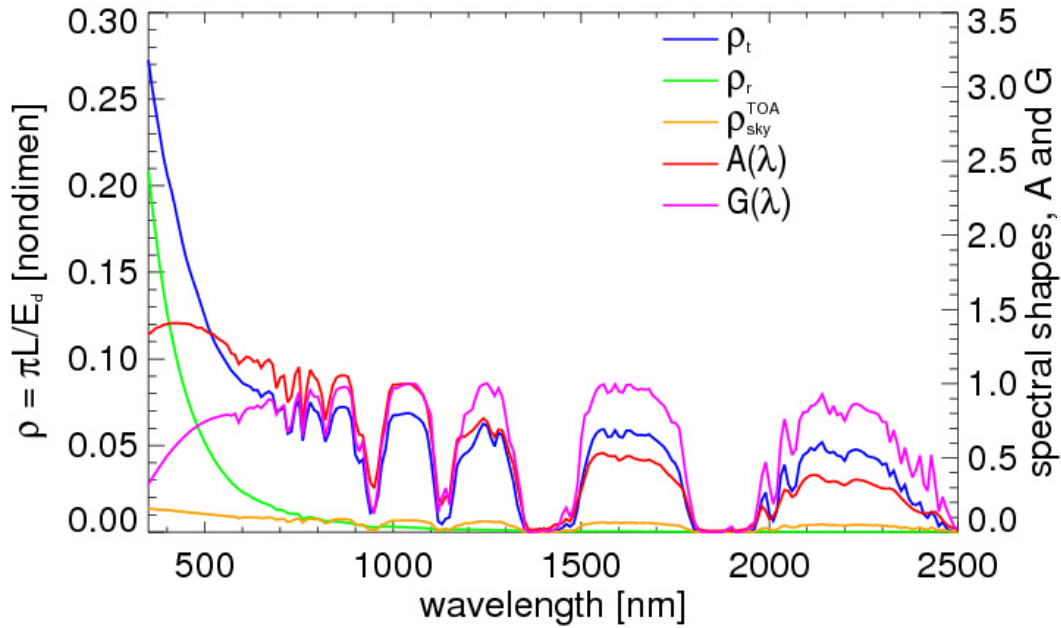
Figure 4.3.2-1. Input spectra for the atmospheric and glint correction for the ALOHA-East edge simulation. HydroMod-generated TOA reflectance (ρ_t), Rayleigh reflectance (ρ_r), sky glint reflectance (ρ_{sky}^{TOA}), and the spectral shape of the aerosol reflectance [$A(\lambda)$] and glint reflectance [$G(\lambda)$]. $A(\lambda)$ and $G(\lambda)$ are normalized at 1040 nm.

Figure 4.3.2-2 shows the glint and aerosol correction for the ALOHA-East, $U = 10$ m s^{-1} simulation. In this high-glint scenario, glint reflectance at 1040 nm is 0.047, which is more than three times that of aerosol reflectance at the same wavelength (0.013). As expected, the sum of the retrieved aerosol and glint reflectances well match the TOA reflectance corrected for Rayleigh and sky glint in the atmospheric transparent windows of the NIR-SWIR spectral range. The difference at visible wavelengths is attributable to the water-leaving reflectance contribution, which is shown in Figure 4.3.2-3. The retrieved water-leaving reflectance compares very well to the true water-leaving reflectance from the HydroMod simulation at the atmospheric window wavelengths.
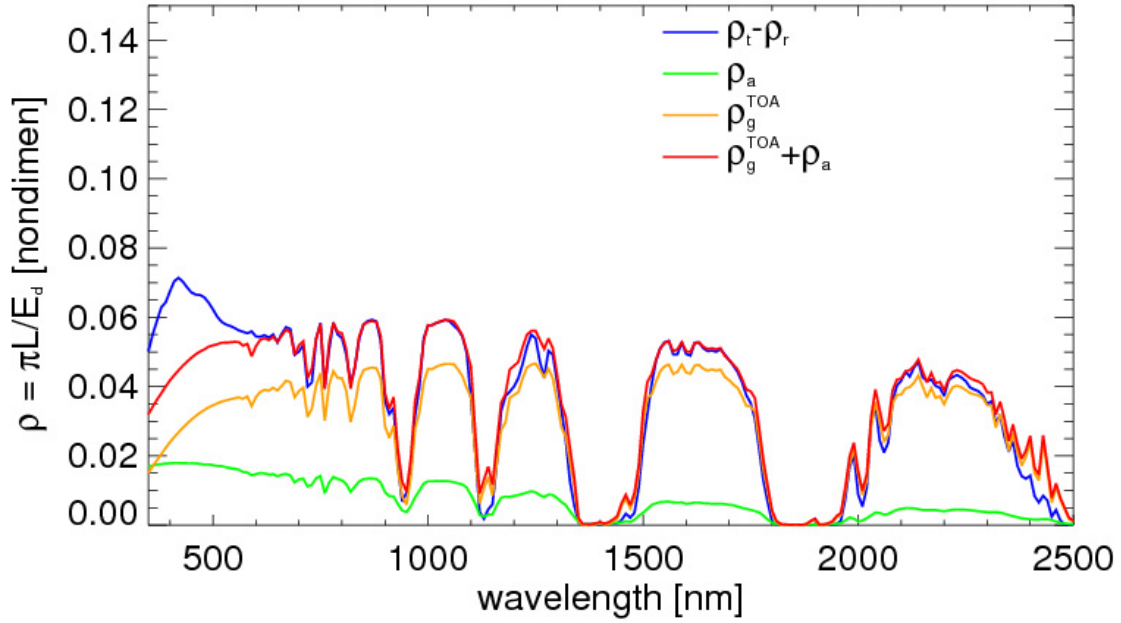
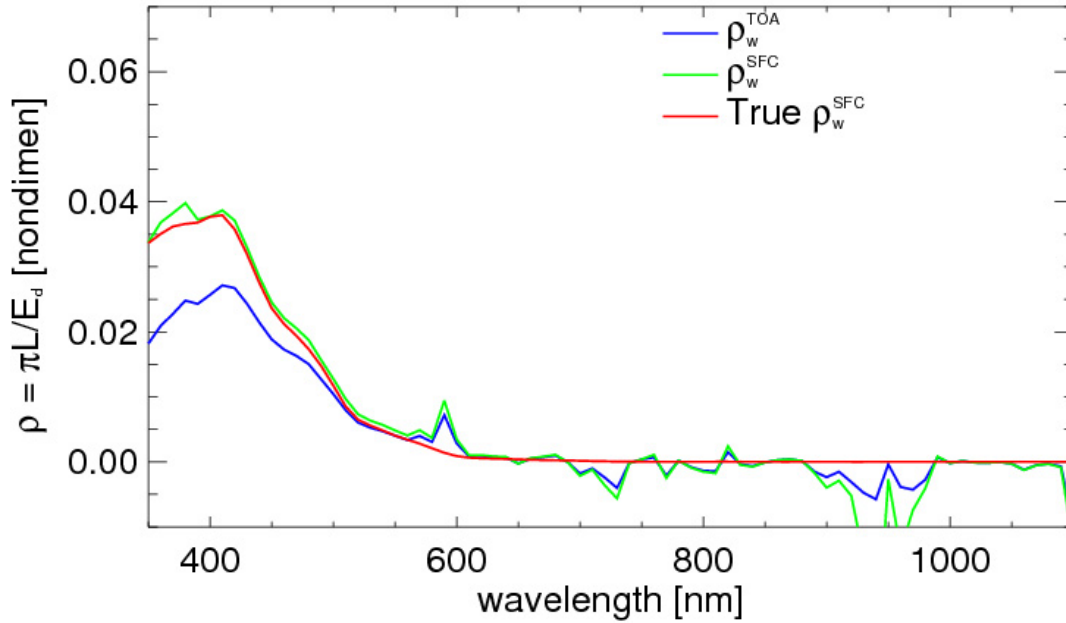**Figure 4.3.2-2.** Aerosol and glint correction for the ALOHA-East edge, $U = 10$ m s^{-1} case.

Figure 4.3.2-3. Water-leaving reflectance spectra for the ALOHA-East edge, $U = 10$ m s^{-1} case, including retrieved TOA spectrum (ρ_w^{TOA}), retrieved surface spectrum (ρ_w^{SFC}), and true surface spectrum.

For comparability, comparisons of water-leaving reflectance between true and retrieved are provided for other three cases in Figures 4.3.2-4 through 4.3.2-6. The ALOHA-West edge, $U = 10$ m s^{-1} case (Figure 4.3.2-4) again shows an excellent retrieval of water-leaving reflectance. However, two $U = 0$ m s^{-1} cases (Figures 4.3.2-5 and 4.3.2-6) show significantly higher retrievals

of the water-leaving reflectance in the visible range. The $U = 0$ m s^{-1} cases represent sun-glint-free conditions with a flat ocean surface. The estimated sun glint (not shown here) is zero for both cases. The errors are presumably due to incorrect computations of the Rayleigh reflectance, the aerosol reflectance shape, or a combination of the two.
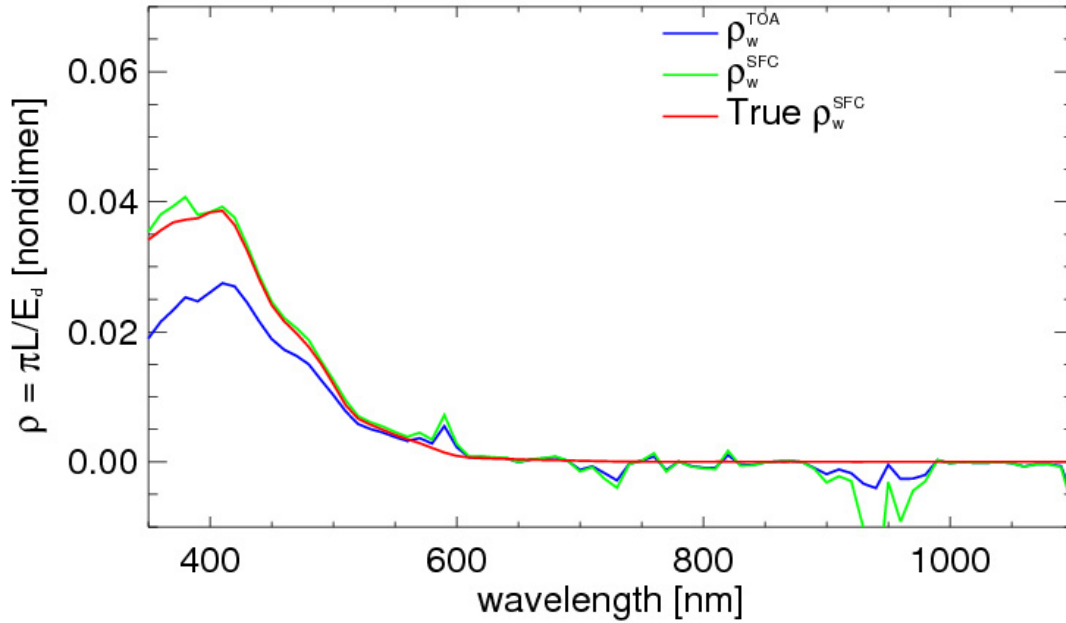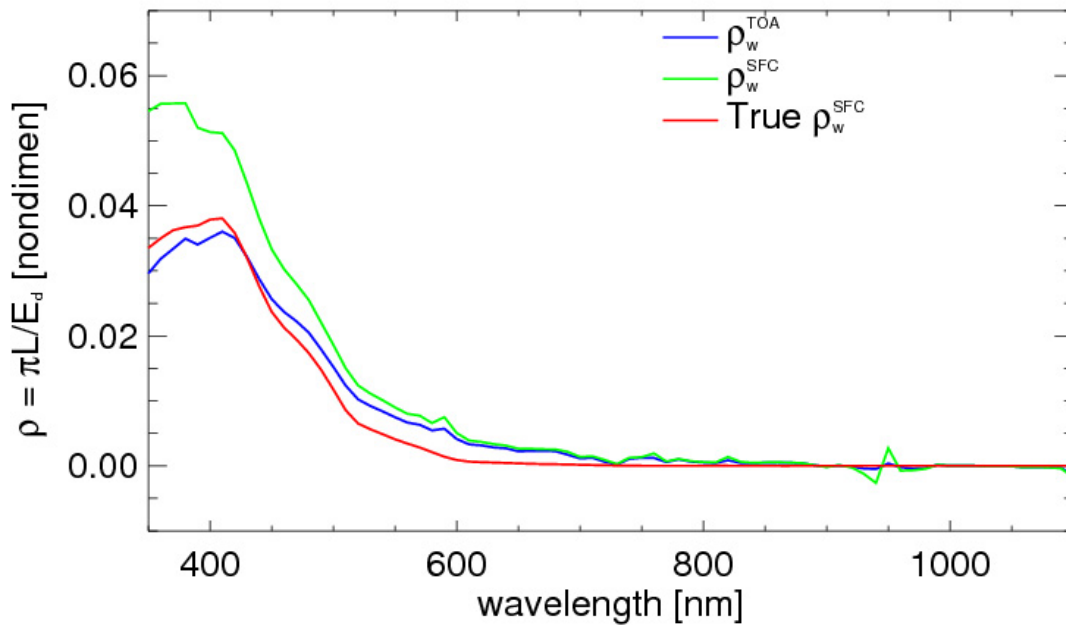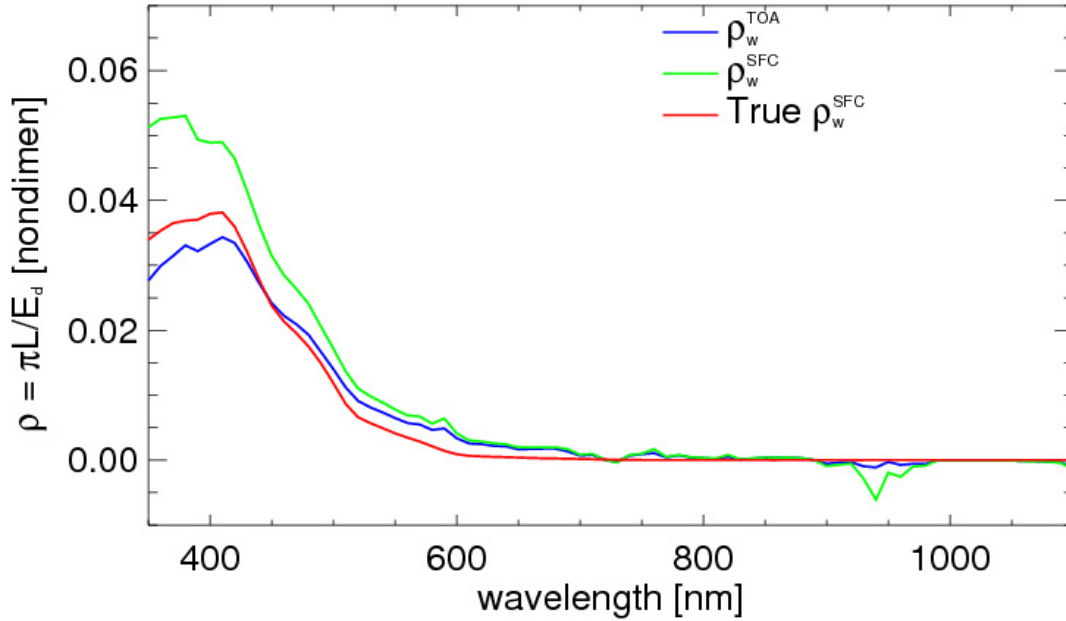

Figure 4.3.2-4. Water-leaving reflectance spectra for the ALOHA-West edge, $U = 10$ m s^{-1} case, including retrieved TOA spectrum (ρ_w^{TOA}), retrieved surface spectrum (ρ_w^{SFC}), and true surface spectrum.

Figure 4.3.2-5. Water-leaving reflectance spectra for the ALOHA-East edge, $U = 0$ m s^{-1} case, including retrieved TOA spectrum (ρ_w^{TOA}), retrieved surface spectrum (ρ_w^{SFC}), and true surface spectrum.

Figure 4.3.2-6. Water-leaving reflectance spectra for the ALOHA-West edge, $U = 0$ m s^{-1} case, including retrieved TOA spectrum (ρ_w^{TOA}), retrieved surface spectrum (ρ_w^{SFC}), and true surface spectrum.

This atmosphere-glint correction exercise for the Station ALOHA simulation demonstrates that a glint correction technique can be implemented systematically on a per-pixel basis, coupled with an atmospheric correction procedure. This glint correction relies on the separation of the TOA glint reflectance from the aerosol reflectance. Successful glint correction therefore requires accurate estimation of the spectral shape of aerosol reflectance and the Rayleigh reflectance.

4.3.3 Estimating Chlorophyll from Simulated and Inverted Data

Standard ocean color algorithms OC4 (SeaWiFS) and OC3M (MODIS) were applied to the forward-modeled radiance and inverted water-leaving reflectance data. To produce appropriate wavebands for use in OC4, HydroMod output and radiometrically inverted spectra at 10-nm intervals was spline-interpolated to 1-nm intervals then convolved with SeaWiFS relative spectral response (oceancolor.gsfc.nasa.gov/DOCS/RSR/SeaWiFS_RSRs.txt). To produce appropriate wavebands for use in OC3M, HydroMod output and radiometrically inverted spectra at 10-nm intervals was spline-interpolated to 1-nm intervals then convolved with MODIS Aqua relative spectral response (oceancolor.gsfc.nasa.gov/DOCS/RSR/Aqua_RSRs.txt).

To explore the impact of glint on chlorophyll retrievals, varying proportions of surface glint radiance were added to the water-leaving reflectance values (only for the HydroMod forward-modeled simulation data). For forward-modeled data, remote-sensing reflectance (R_{rs}) was calculated as

$$R_{rs} = (L_w + xL_g) / E_d, \tag{4.3.3-1}$$

where L_w is water-leaving radiance computed by HydroMod; L_g is glint radiance computed by HydroMod; E_d is downwelling plane irradiance computed by HydroMod; and x is the proportion of glint radiance included in the calculation, varying between 0 and 1. For the radiometrically inverted data, nondimensional reflectance values were divided by a factor of π to produce remote-sensing reflectance (R_{rs}) in units of sr^{-1}.

Table 4.3.3-1 lists chlorophyll values retrieved from the HydroMod simulation data, both for OC4 and OC3M. For detailed explanation of model runs, see Section 4.3.1. The concentration of suspended chlorophyll used in the forward model was 0.05 mg m^{-3}, a typical value at Station ALOHA. The values are plotted in Figure 4.3.3-1.

Table 4.3.3-1. Chlorophyll values (mg m^{-3}) retrieved using OC4 and OC3M algorithms applied to R_{rs} modeled by HydroMod for conditions at Station ALOHA on June 21. Values for x refer to proportion of glint included in calculation of $R_{rs} = (L_w + xL_g) / E_d$. Actual chlorophyll concentration used in HydroMod bio-optical model is 0.05 mg m^{-3}.

Algorithm	Edge	U (m s^{-1})	Value of x in $R_{rs} = (L_w + xL_g) / E_d$				
			0.0	0.25	0.5	0.75	1.0
OC4	West	0	0.066	0.081	0.094	0.106	0.117
OC4	East	0	0.065	0.084	0.101	0.115	0.128
OC4	West	10	0.065	0.22	0.355	0.484	0.603
OC4	East	10	0.064	0.354	0.613	0.833	1.013
OC3M	West	0	0.063	0.077	0.089	0.101	0.111
OC3M	East	0	0.063	0.08	0.095	0.109	0.122
OC3M	West	10	0.062	0.21	0.337	0.454	0.559
OC3M	East	10	0.062	0.336	0.567	0.754	0.903

Even with no glint, OC4 and OC3M overestimate chlorophyll by 20%: retrievals are ~0.06 mg m^{-3}. This is likely because HydroMod, OC4 and OC3M all rely on empirical best fits of various data sets to relate chlorophyll to absorption and scattering (HydroMod) or to R_{rs} (OC4, OC3M). Thus, the observed 20% error reflects that the IOP models and retrieval algorithms are based on different data sets, for which the optical properties were different for the same chlorophyll values.

The retrieval does vary with wind speed and position on the HyspIRI scan line. When wind speed is zero, there is not much difference in retrievals between the west and east edges of the scan line. When wind speed is 10 m s^{-1}, there is strong dependency on position in the scan line. Although angles associated with the west end of the swath perform better than those associated with the east edge, providing about half as large an overestimate, only in the zero-wind-speed cases do chlorophyll overestimates in the presence of large glint contributions stay within ~2× the glint-free estimate. Therefore, an effective glint correction (or some fundamentally different, full-spectral algorithm) would be required for accurate chlorophyll retrievals under all wind conditions and would be especially important in the presence of moderate-to-high wind speeds. This result differs from bottom-type discrimination, which appears more robust to glint than turbidity and worked well under a range of view-illumination geometries and water depths relevant to the HyspIRI concept (see Sections 4.1 and 4.2). A useful feature of the observed retrievals is that consistent systematic gradients across the HyspIRI VSWIR swath in chlorophyll estimated by these algorithms (i.e., higher means and/or variances towards the east edge), in the

presence of light-to-moderate winds, might provide an indicator of ineffective or incomplete glint removal.
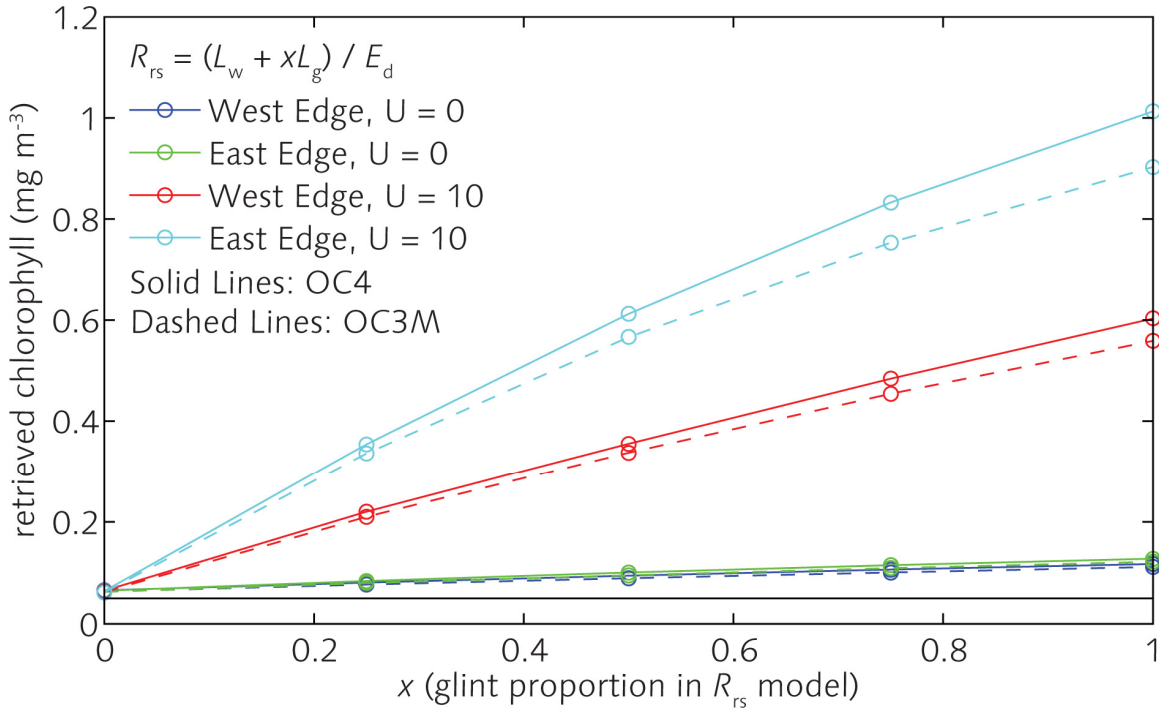

Figure 4.3.3-1. Chlorophyll values retrieved using OC4 (solid lines) and OC3M (dashed lines) algorithms, as applied to R_{rs} modeled by HydroMod for conditions at Station ALOHA on June 21. Horizontal black line is 0.05 mg m^{-3}, the chlorophyll value used in HydroMod's Case 1 bio-optical model.

Figure 4.3.3-2 shows ρ_w^{SFC} as retrieved in Section 4.3.2. When the modeled wind speed is 10 m s^{-1}, the inverted ρ_w^{SFC} closely matches the "true" ρ_w^{SFC} for both the west and east edges of the HyspIRI field of view. For the no-wind condition, however, inversion results overestimate "true" ρ_w^{SFC} by almost 0.02 (nondimensional reflectance units) at blue wavelengths, also for both the west and east edges of the HyspIRI field of view. This indicates that the coupled atmosphere-glint correction procedure noticeably under-corrects glint for the zero-wind case.

Table 4.3.3-2 lists the retrieved chlorophyll values using OC4 and OC3M and the inverted ρ_w^{SFC} spectra shown in Figure 4.3.3-2. For the zero-wind scenario, both algorithms significantly overestimate suspended chlorophyll concentrations, while for the 10 m s^{-1} wind scenario, retrievals are closer to "truth."
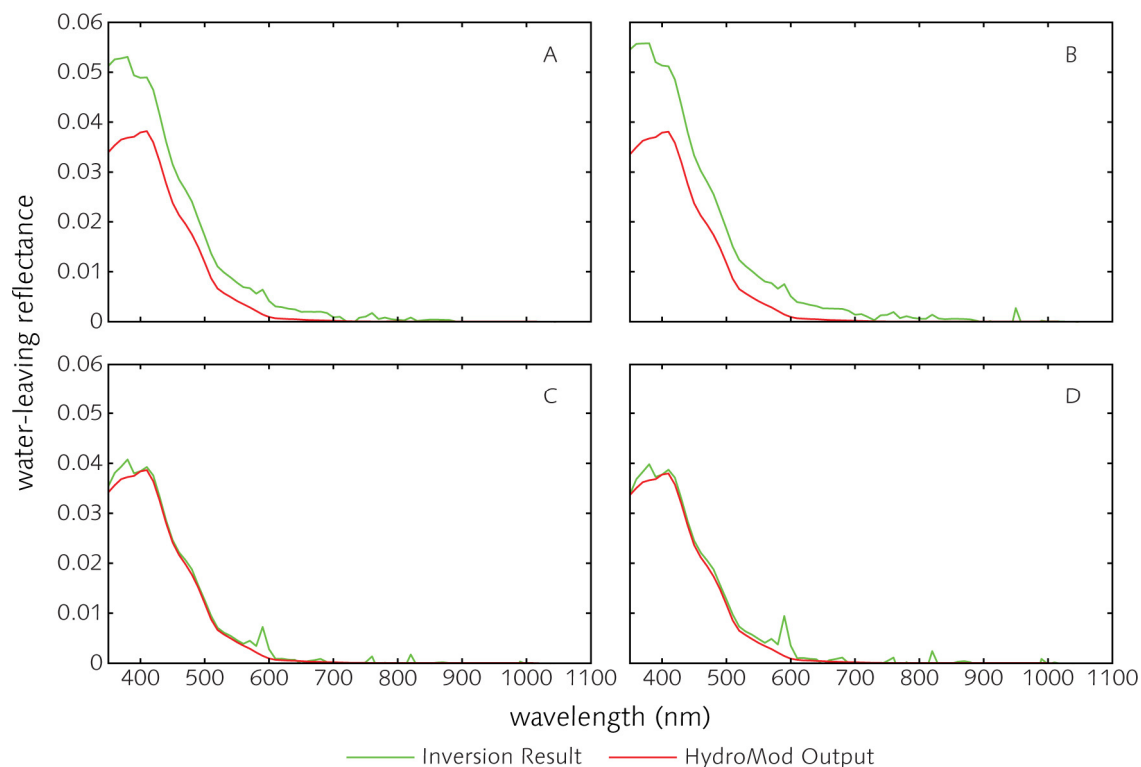
Figure 4.3.3-2. Radiometrically inverted, water-leaving reflectance spectra for Station ALOHA June 21 simulation. (A) West edge of HyspIRI field of view, $U = 0$ m s^{-1}; (B) east edge, $U = 0$ m s^{-1}; (C) west edge, $U = 10$ m s^{-1}; and (D) east edge, $U = 10$ m s^{-1}.

Table 4.3.3-2. Chlorophyll values (mg m^{-3}) retrieved using OC4 and OC3M algorithms applied to R_{rs} data derived from Figure 4.3.3-2. Actual chlorophyll concentration used in HydroMod bio-optical model is 0.05 mg m^{-3}.

Edge	U (m s^{-1})	Algorithm	
		OC4	OC3M
West	0	0.12	0.12
East	0	0.14	0.13
West	10	0.08	0.07
East	10	0.08	0.08

4.4   Emergent Vegetation and Coastal Wetlands

For coastal emergent vegetation, the glint issue becomes much more complex. For example, in salt marshes, tidal emergent vegetation is typically erectophile, with small pools of water interspersed (Figure 4.4-1). At higher tides, water encroaches on the vegetation itself, such that the soil becomes submerged, but the blades of marsh grass remain subaerial. In these systems, glint undoubtedly contributes to the remotely sensed signal and, as in open waters, the effect varies with sun and view angles. However, suitable models or measurement techniques have yet to be developed to quantify this effect.

Figure 4.4-1. Examples of salt marsh vegetation and interspersed water in Fishing Bay Wildlife Management Area, Maryland. Two species of salt marsh grass are labeled. Photos: K. Turpie.

Qualitatively, it is possible to infer glint effects from multi-angle satellite images acquired by CHRIS/Proba. Figure 4.4-2 illustrates an example of glint in the wetlands shown in Figure 4.4-1. With a nominal view zenith angle of 0°, glint is visually apparent in water bodies amongst the vegetated areas (Figure 4.4-2a). This glint is likely caused by capillary waves patterned by the local wind field. With a nominal view zenith angle of 55°, glint is much less visually apparent (Figure 4.4-2b).
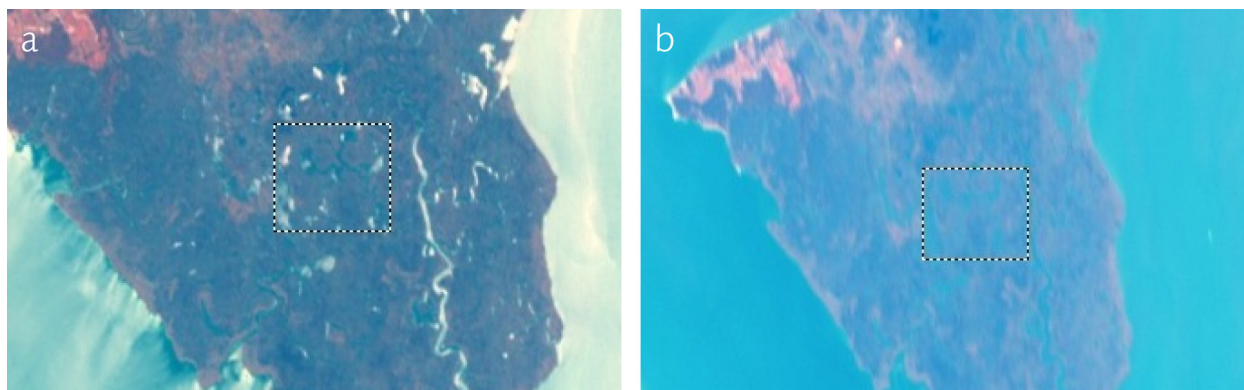
Figure 4.4-2. Multi-angle CHRIS/Proba images of Fishing Bay Wildlife Management Area, Maryland. (a) At 0° nominal view, zenith-angle glint is visually apparent on water bodies interspersed amongst subaerial vegetation. (b) At 55° nominal view, zenith-angle glint is much less apparent. Boxes cover the same ground area in (a) and (b). This region is extracted for statistics shown in Figure 4.4-3.

These visual glint patterns are supported by sample spectra. For the same region of wetland, the 0° nominal view angle spectra (Figure 4.4-3a) have higher values and are more variable than the 55° view angle spectra (Figure 4.4-3b).
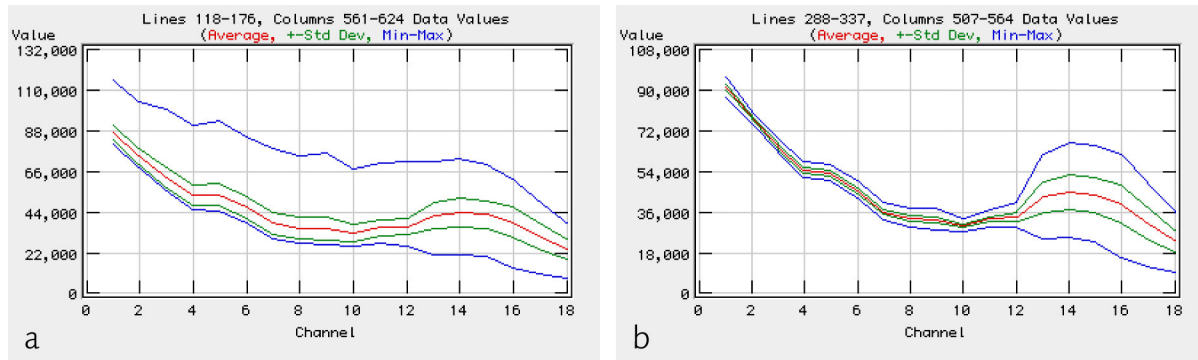
Figure 4.4-3. Spectra extracted from regions highlighted by boxes in Figure 4.4-2. (a) At 0° nominal view zenith angle, glint produces very high values across the spectrum, evidenced by the maximum spectral curve. (b) At 55° nominal view zenith angle, the glint effect is greatly reduced.

The impact of glint on emergent vegetation retrievals is unknown. Because this vegetation is subaerial, NIR and SWIR wavebands are viable for detection and characterization. This may help offset glint effects that would otherwise negatively impact retrievals based solely on VIS wavebands. The issue of emergent vegetation is possibly the most in need of focused investigation.

4.5   Summary

Results from two basic HyspIRI science objectives, to investigate glint impacts on retrievals for coral reefs and seagrass, showed that expected levels of glint do not appear to dramatically affect classification retrievals. Glint has the greatest impact when retrieval conditions are already marginal, for example, when water column optical properties limit penetration depth. Potential for improvement via mitigation for glint was not investigated.

For the open ocean, with very low suspended chlorophyll levels, it is clear that glint correction must be tied to correction for atmospheric aerosols. Thus, both are fundamental requirements for accurate retrieval of spectral remote-sensing reflectance.

The situation is less clear for glint effects in emergent vegetation. Measurement and modeling capabilities for these systems lag those for shallow and deep oceans. At the same time, emergent vegetation has the benefit of usefully observable NIR and SWIR spectral features.

5   Mitigation Options
5.1   Avoidance

Avoidance is the simplest method for mitigation of glint impacts, and it is the method of choice in operational ocean color. It is a viable option for this application because ocean color satellites have very wide fields of view and very short revisit times. As a result, any portions of imagery that exhibit significant glint can merely be ignored, then re-imaged on subsequent satellite overpasses.

Nearshore and benthic applications typically require higher spatial resolution than do scientific efforts to assess deep-ocean, offshore aquatic reflectance for the purpose of estimating inherent and apparent optical properties and parameters such as chlorophyll concentration from ocean color, i.e., 1–100 m vs. 1 km. The higher spatial resolution required closer to shore is offset by narrower fields of view and longer revisit times. The data rate for a given area of Earth surface is much lower, and it is generally not possible to ignore image data that exhibit glint effects. Thus, glint avoidance is a luxury not often afforded to nearshore and benthic applications.

Several glint correction techniques have been proposed in the peer-reviewed literature. Virtually all of them rely on the NIR to derive glint levels in the VIS. The following subsects describe the general basis for a few of these techniques.

5.2   NIR-VIS Empirical Linear Relationships

Upwelling radiance just above the sea surface $L_u(\lambda)$ is the sum of the water-leaving radiance $L_w(\lambda)$ and the glint radiance $L_g(\lambda)$:

$$L_u(\lambda) = L_w(\lambda) + L_g(\lambda). \tag{5.2-1}$$

At NIR wavelengths, especially those longer than ~900 nm, water-leaving radiance is negligible due to very strong absorption by water (see Figure 2-1), such that

$$L_w(\text{NIR}) \approx 0. \tag{5.2-2}$$

Thus, for NIR wavelengths, equation (5.2-1) reduces to

$$L_u(\text{NIR}) \approx L_g(\text{NIR}). \tag{5.2-3}$$

Because the index of refraction of water is nearly identical at VIS and NIR wavelengths (see Section 2), the relative amount of downwelling radiance reflected upward is solely a function of geometry and is independent of wavelength (see Section 3). $L_g(\text{VIS})$ and $L_g(\text{NIR})$ have very strong positive correlation.

If there are several remote-sensing pixels, each with the same $L_w(\lambda)$, then variability in $L_u(\lambda)$ is equivalent to variability in $L_g(\lambda)$. For NIR wavelengths, this situation arises *a priori* through equation (5.2-3). For VIS wavelengths, this situation arises when the underwater light field is the

same for each of the given pixels, as might occur for a small area of optically deep water. The slope $\beta_1(L_u)$ of the least-squares linear regression line of $L_u(VIS)$ on $L_u(NIR)$ is

$$\beta_1(L_u) = r(L_u) \times s[L_u(VIS)] \div s[L_u(NIR)], \tag{5.2-4}$$

where $r(L_u)$ is the correlation coefficient between $L_u(VIS)$ and $L_u(NIR)$, and s refers to the sample standard deviation. Because the variability in $L_u(\lambda)$ is equivalent to the variability in $L_g(\lambda)$, $s[L_g(VIS)] = s[L_u(VIS)]$, and $s[L_g(NIR)] = s[L_u(NIR)]$. Thus, the slope $\beta_1(L_g)$ of the least-squares linear regression line of $L_g(VIS)$ on $L_g(NIR)$ is

$$\beta_1(L_g) = r(L_u) \times s[L_u(VIS)] \div s[L_u(NIR)]. \tag{5.2-5}$$

$L_g(VIS)$ is related to $L_g(NIR)$ by

$$L_g(VIS) = \beta_1(L_g) \times L_g(NIR). \tag{5.2-6}$$

Once $\beta_1(L_g)$ has been determined for the few pixels where $L_w(\lambda)$ is constant, it is applicable to the entire scene. $L_w(VIS)$ for the entire scene is determined by substitution of equation (5.2-6) into equation (5.2-1):

$$L_w(VIS) = L_u(VIS) - \beta_1(L_g) \times L_g(NIR). \tag{5.2-7}$$

Figure 5.2-1 shows regression lines for three VIS wavebands against a NIR waveband for an AVIRIS scene of French Frigate Shoals, Hawaii (f000418t01p03_r01). Figure 5.2-2 shows the scene before and after application of equation (5.2-7). The yellow box highlights the deep-ocean region from which glint statistics were derived.
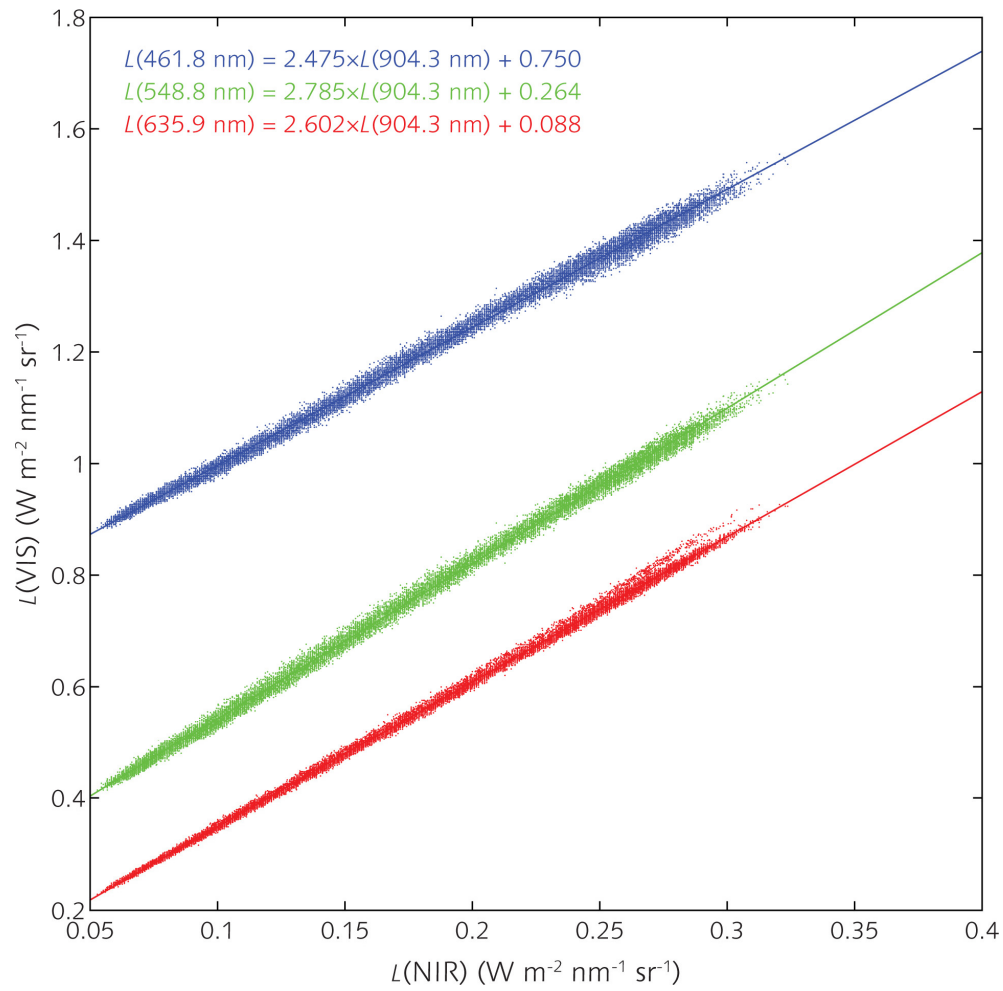
Figure 5.2-1. Empirical linear relationships between three VIS wavebands and a NIR waveband for the AVIRIS scene shown in Figure 5.2-2.
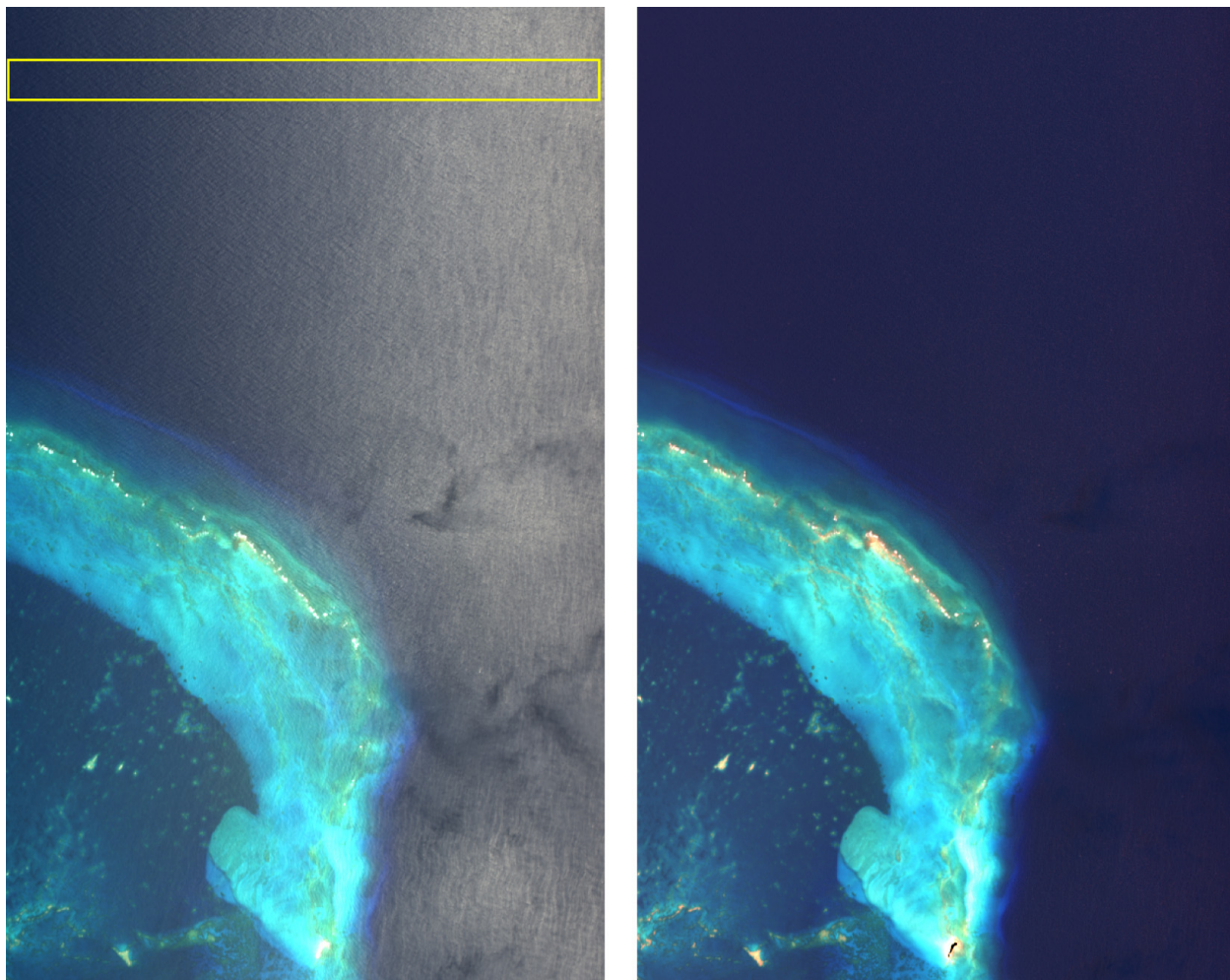
Figure 5.2-2. AVIRIS scene f000418t01p03_r01 covering the southeast portion of French Frigate Shoals, Hawaii and surrounding deep ocean. Image is rotated so that north is to the left of the scene. (Left) Original scene shows very strong glint effects. The yellow box highlights the region from which empirical linear relationships in Figure 5.2-1 were derived. (Right) The scene after application of equation (5.2-7). Glint effects are very effectively removed.

5.3   Subtraction of NIR Reflectance

Another empirical approach to correcting for glint effects makes use of the fact that glint reflectance is nearly spectrally flat throughout the VIS and NIR regions of the spectrum. Following Gao et al. (1993, 2000, 2007), the remote sensing imagery is first converted to TOA apparent reflectance and corrected for atmospheric effects. The result of the atmospheric correction is apparent reflectance at the sea surface. Because of the relationship in equation (5.2-2), any reflectance value at NIR wavelengths must arise from glint. Because glint reflectance is the same at VIS and NIR wavelengths, the NIR-derived glint reflectance can simply be subtracted from the VIS reflectance, leaving a de-glinted scene. Figure 5.3-1 shows an example of the de-glinting result.

Figure 5.3-1. Example of glint correction using subtraction of NIR reflectance. (Left) Original AVIRIS scene of Kaneohe Bay, Hawaii (f000412t01p03_r08). (Right) The scene after atmosphere and glint correction. Clouds and some sea surface features remain; this is due to automated masking. Overall, glint correction performs quite well.

5.4   Uniform Spectral Offset Approach

Goodman and Ustin (2007) and Goodman et al. (2008) describe a slightly modified version of the approach in Section 5.3. The algorithm is implemented following atmospheric correction using values of surface remote-sensing reflectance (R_{rs}, units sr^{-1}). A uniform spectral offset is calculated for each pixel such that the resulting reflectance at 750 nm is equal to a derived constant, Δ. Rather than assuming the same offset applies for all pixels or that reflectance is zero at all wavelengths greater than 750 nm, the offset in this algorithm allows reflectance to be greater than zero in areas of optically shallow water with bright substrates (e.g., sand). Using the reflectance output generated from atmospheric correction, $R_{rs}^{*}(\lambda)$, the sun-glint corrected surface reflectance, $R_{rs}(\lambda)$, is calculated as

$$R_{rs}(\lambda) = R_{rs}^{*}(\lambda) - R_{rs}(750) + \Delta, \tag{5.4-1}$$

where

$$\Delta = 0.00019 + 0.1[R_{rs}^{*}(640) - R_{rs}^{*}(750)]. \tag{5.4-2}$$

5.5 Glint-Aerosol Discrimination

The objective of this approach is simultaneous determination of the aerosol and glint components from the TOA reflectance spectrum itself. This approach would fit an automated pixel-by-pixel atmospheric correction procedure as outlined in Section 4.3. The spectral decomposition relies on the distinct shapes of the TOA glint and aerosol reflectance spectra in the NIR-SWIR bands. Aerosol reflectance has a steeper slope, while glint reflectance is rather flat across NIR-SWIR wavelengths.

The preliminary inversion of modeled Station ALOHA TOA spectra in Section 4.3 demonstrates the approach using two SWIR bands and a constant aerosol model. Results are promising, but further investigation is necessary. It would be especially useful to develop a model that can accommodate aerosol variability. Figure 5.5-1 shows variability in spectral shapes of aerosol reflectance simulated using 6S code (Vermote et al. 1997; Kotchenova et al. 2006) for three aerosol types for the Station ALOHA geometry used in Section 4.3. Since the variability primarily arises due to different aerosol types, the aerosol slope (or model) should also be retrieved in the glint-aerosol separation step. To retrieve three parameters—aerosol intensity, glint intensity, and aerosol slope—three or more bands are required for spectral decomposition. Least squares error optimization could be employed to find a matched spectrum.
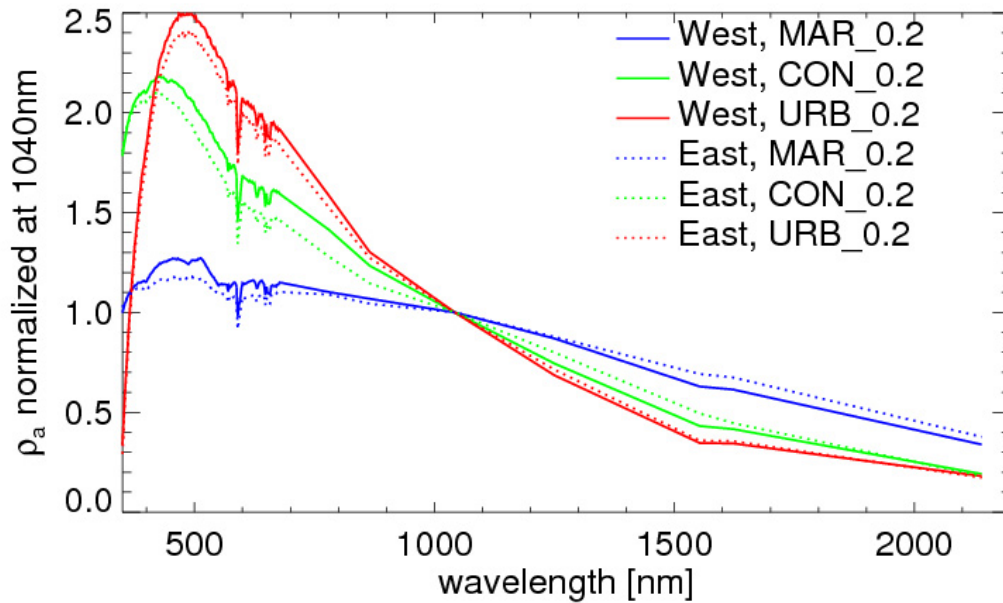

Figure 5.5-1. Variability of the aerosol reflectance spectral shapes. Computation was made using 6S code for three aerosol types—maritime, continental and urban. Aerosol optical thickness is 0.2 at 550 nm. Sun-sensor geometries are the same as ALOHA simulations in Section 4.3. For wavelengths >700nm, only atmospheric transparent window channels are shown for clarity.

6   Recommendations
6.1   Algorithms Showing Promise

The literature and the examples from Section 5 demonstrate that glint correction is feasible. The examples in Section 4 further demonstrate that key HyspIRI science objectives are achievable even in the presence of glint. Therefore, it is very reasonable to deduce that active glint correction can be a part of a successful HyspIRI processing flow; that is, glint avoidance is unnecessary, except possibly in the most extreme cases.

Each of the approaches described in Sections 5.2, 5.3, 5.4 and 5.5 has good potential for routine glint correction. Each also requires further refinement. The Empirical Linear Relationship (Section 5.2) method is insensitive to spectral variations in the reflectance of the sea surface and thus provides very good glint correction. However, in its current form, this method relies on human interaction to identify image regions of constant $L_w(\lambda)$. This precludes automated implementation. The remaining correction methods are all fully automated, so they are more readily implemented in an automated processing flow. However, they all rely on the assumption that sea surface reflectance is spectrally flat across the VIS–NIR. This assumption is valid only to first-order; deviations result in over- or under-correction. The deviations, though, would arise from differences in the index of refraction of seawater, the spectral shape of which is predictable. Thus, it should be possible to refine these methods to provide consistently reliable results.

6.2   Priorities for Phase A
6.2.1   Further Sensitivity Analyses

This report is not exhaustive. The presented analyses have touched on some key points about glint and its impact on remote-sensing retrievals of certain biophysical parameters. These issues could certainly benefit from deeper investigation. There are technical issues yet to be investigated, including (among others) the convolution of sensor noise and its impact on glint detection and correction. These technical issues, a wider variety of environmental conditions, and additional science objectives can all be addressed through continued modeling exercises.

6.2.2   Field Glint Observations

It would be very desirable to validate model results of selected, important HyspIRI science objectives. This validation can be performed on a relatively small scale with *in situ* measurements of relevant optical and biophysical parameters. Airborne measurements could also be useful, but then the scope of the validation becomes larger and less constrained. For this type of validation, see Section 6.3.1.

6.3   Longer-Term Priorities
6.3.1   Comprehensive Oceanic and Atmospheric Data Set

Forward radiative transfer models have been validated to the extent possible with incomplete data sets. Model inputs have relied on available IOP measurements plus reasonable assumptions about the missing pieces. Model predictions have been compared with available radiometric or AOP measurements. However, there are always enough missing inputs and outputs that rigorous

and complete model validation remains elusive. The same is true for inverse algorithms—there are always too many missing pieces requiring assumptions. Thus, comprehensive oceanic and atmospheric data sets are needed for validation of radiative transfer forward models (e.g., HydroLight, Monte Carlo, Modtran, HydroMod) and development and validation of remote-sensing inverse models/algorithms (e.g., TOA radiance → atmospheric correction algorithms → Rrs → in-water algorithms → IOPs, chlorophyll, water depth, bottom-type, etc.).

Environmental optics would be greatly advanced by the collection of a few comprehensive data sets for selected water and atmospheric conditions. In addition to collecting the data needed for model and algorithm validation, such a program should be viewed as an opportunity to compare various instruments and methodologies for making the same kind of measurement. Measurement redundancy is absolutely necessary in a field experiment.

Such a program must include measurements for all inputs needed to solve the radiative transfer equation (RTE) as well as the outputs from the RTE. To validate a coupled ocean-atmosphere optical model at one point in space and time, the measurements should be simultaneous and co-located. In addition to all pertinent optical parameters for solution of the RTE, ancillary measurements should be made for evaluation of various retrieval algorithms (e.g., chlorophyll, water depth, and bottom type).

The program as described would be both ambitious and expensive, but it would not be for the sole benefit of HyspIRI. This program would benefit all remote-sensing missions that observe the ocean. Thus, this program should be jointly developed by the broader oceanic and atmospheric optical science communities.

6.3.2   Glint Toolbox

Glint correction algorithms are in a state of ongoing development. Even as they become codified and implemented in routine processing, it still may be advantageous to utilize different algorithms, depending on the situation at hand. Thus, it would be useful to have a glint toolbox utility from which a user could select among a suite of glint correction techniques. Such a toolbox could easily be incorporated as a module in existing image processing software applications that rely on high-level computer languages such as IDL (e.g., ENVI and SeaDAS).

7   References

Acharya PK, Berk A, Bernstein LS, Matthew MW, Adler-Golden SM, Robertson DC, Anderson GP, Chetwynd JH, Kneizys FX, Shettle EP, Abreu LW, Gallery WO, Selby JEA, Clough SA (1998) *MODTRAN User's Manual, Versions 3.7 and 4.0.* Air Force Research Laboratory, Space Vehicles Directorate, Hanscom Air Force Base, Mass. 79 pages

Berk A, Anderson GP, Acharya PK, Shettle EP (2008) *MODTRAN5.2.0.0 User's Manual.* Spectral Sciences, Inc., MA & Air Force Research Laboratory, MA. pages

Borrego JA (1993) Wave height spectrum from sun glint patterns - an inverse problem. J Geophys Res-Oceans 98:10245-10258

Cox C, Munk W (1954) Statistics of the sea surface derived from sun glitter. Journal of Marine Research 13:198-227

Earth Science and Applications from Space: National Imperatives for the Next Decade and Beyond (2007). Committee on Earth Science and Applications from Space: A Community Assessment and Strategy for the Future (2007). National Research Council, National Academies Press. Referred to as the Decadal Survey or NRC 2007.

Fraser RS, Mattoo S, Yeh EN, McClain CR (1997) Algorithm for atmospheric and glint corrections of satellite measurements of ocean pigment. J Geophys Res-Atmos 102:17107-17118

Gao BC, Heidebrecht KB, Goetz AFH (1993) Derivation of scaled surface reflectances from AVIRIS data. Remote Sens Environ 44:165-178

Gao BC, Montes MJ, Ahmad Z, Davis CO (2000) Atmospheric correction algorithm for hyperspectral remote sensing of ocean color from space. Appl Optics 39:887-896

Gao BC, Montes MJ, Li RR, Dierssen HM, Davis CO (2007) An atmospheric correction algorithm for remote sensing of bright coastal waters using MODIS land and ocean channels in the solar spectral region. IEEE Trans Geosci Remote Sens 45:1835-1843

Goodman JA, Ustin SL (2007) Classification of benthic composition in a coral reef environment using spectral unmixing. Journal of Applied Remote Sensing 1

Goodman JA, Lee ZP, Ustin SL (2008) Influence of atmospheric and sea-surface corrections on retrieval of bottom depth and reflectance using a semi-analytical model: a case study in Kaneohe Bay, Hawaii. Applied Optics 47:F1-F11

Gordon HR, Voss KJ (2004) MODIS normalized water-leaving radiance algorithm theoretical basis document (MOD 18) version 5

Hedley JD, Harborne AR, Mumby PJ (2005) Simple and robust removal of sun glint for mapping shallow-water benthos. Int J Remote Sens 26:2107-2112

Hochberg EJ, Andréfouët S, Tyler MR (2003) Sea surface correction of high spatial resolution Ikonos images to improve bottom mapping in near-shore environments. IEEE Trans Geosci Remote Sens 41:1724-1729

Kay S, Hedley JD, Lavender S (2009) Sun glint correction of high and low spatial resolution images of aquatic scenes: a review of methods for visible and near-infrared wavelengths. Remote Sensing 1:697-730

Kotchenova SY, Vermote EF, Matarrese R, Klemm FJ (2006) Validation of a vector version of the 6S radiative transfer code for atmospheric correction of satellite data. Part I: Path radiance. Appl Optics 45:6762-6773

Kou LH, Labrie D, Chylek P (1993) Refractive-indexes of water and ice in the 0.65-μm to 2.5-μm spectral range. Appl Optics 32:3531-3540

Lee Z, Carder KL, Chen RF, Peacock TG (2001) Properties of the water column and bottom derived from Airborne Visible Infrared Imaging Spectrometer (AVIRIS) data. J Geophys Res-Oceans 106:11,639-611,651

Lee ZP, Carder KL, Mobley CD, Steward RG, Patch JS (1998) Hyperspectral remote sensing for shallow waters. 1. A semianalytical model. Appl Optics 37:6329-6338

Lee ZP, Carder KL, Mobley CD, Steward RG, Patch JS (1999) Hyperspectral remote sensing for shallow waters: 2. Deriving bottom depths and water properties by optimization. Appl Optics 38:3831-3843

Lee ZP, Casey B, Arnone R, Weidemann A, Parsons R, Montes MJ, Gao BC, Goode W, Davis CO, Dye J (2007) Water and bottom properties of a coastal environment derived from Hyperion data measured from the EO-1 spacecraft platform. Journal of Applied Remote Sensing 1:DOI: 10.1117/1111.2822610

Lesser MP, Mobley CD (2007) Bathymetry, water optical properties, and benthic classification of coral reefs using hyperspectral remote sensing imagery. Coral Reefs 26:819-829

Louchard EM, Reid RP, Stephens FC, Davis CO, Leathers RA, Downes TV (2003) Optical remote sensing of benthic habitats and bathymetry in coastal environments at Lee Stocking Island, Bahamas: A comparative spectral classification approach. Limnol Oceanogr 48:511-521

Lyzenga DR, Malinas NR, Tanis FJ (2006) Multispectral bathymetry using a simple physically based algorithm. IEEE Trans Geosci Remote Sens 44:2251-2259

Mobley CD (1994) *Light and Water: Radiative Transfer in Natural Waters*. Academic Press, San Diego

Mobley CD, Sundman LK (2008) *HydroLight 5 EcoLight 5 Technical Documentation*. Sequoia Scientific, Inc. 95 pages

Mobley CD, Gentili B, Gordon HR, Jin ZH, Kattawar GW, Morel A, Reinersman P, Stamnes K, Stavn RH (1993) Comparison of numerical models for computing underwater light fields. Applied Optics 32:7484-7504

Mobley CD, Sundman LK, Davis CO, Bowles JH, Downes TV, Leathers RA, Montes MJ, Bissett WP, Kohler DDR, Reid RP, Louchard EM, Gleason A (2005) Interpretation of hyperspectral remote-sensing imagery by spectrum matching and look-up tables. Appl Optics 44:3576-3592

Montagner F, Billat V, Bélanger S (2003) MERIS ATBD 2.13 - Sun glint flag algorithm, issue 4, revision 2

Nicodemus FE, Richmond JC, Hsia JJ, Ginsburg IW, Limperis T (1977) *Geometrical Considerations and Nomenclature for Reflectance*. National Bureau of Standards Monographs National Bureau of Standards. 52 pages

Pope RM, Fry ES (1997) Absorption spectrum (380-700 nm) of pure water .2. Integrating cavity measurements. Appl Optics 36:8710-8723

Quan XH, Fry ES (1995) Empirical equation for the index of refraction of seawater. Appl Optics 34:3477-3480

Tassan S (1994) Removal of the effect of sun-glitter from Thematic Mapper imagery of the sea. Int J Remote Sens 15:719-723

Vermote EF, Tanre D, Deuze JL, Herman M, Morcrette J-J (1997) Second Simulation of the Satellite Signal in the Solar Spectrum, 6S: An Overview. IEEE Trans Geosci Remote Sens 35:675-686

Viollier M, Tanré D, Deschamps PY (1980) An algorithm for remote sensing of water color from space. Boundary-Layer Meteorology 18:247-267

Wang MH, Bailey SW (2001) Correction of sun glint contamination on the SeaWiFS ocean and atmosphere products. Appl Optics 40:4790-4798

Appendix A   Global Wind Fields: 2-Parameter Weibull Distribution

An 18-year time series of wind speeds was constructed using SSM/I-10, SSM/I-11, SSM/I-13, and SSM/I-14 data from January 1, 1988, through September 1, 2006. SSM/I-11 and SSM/I-14 are polar orbiters, with afternoon equatorial crossovers. SSM/I-10 and SSM/I-13 have morning equatorial crossovers. Wind speed is calculated for all valid retrievals, except in the presence of rain.

From the 18-year SSMI data set, monthly Weibull parameters were calculated using maximum likelihood estimation (MLE). The shape and scale parameters were found via a multidimensional, unconstrained, nonlinear minimization of the log-likelihood function using the downhill simplex method (Nelder and Mead).

$$f(x) = \frac{\beta}{\eta}\left(\frac{x}{\eta}\right)^{\beta-1} e^{-\left(\frac{x}{\eta}\right)^{\beta}}$$

The Weibull distribution, $f(x)$, is greater than or equal to zero; the shape parameter, β, is greater than zero; and the scale parameter, η, is also greater than zero.

$$\text{Mean of } f(x) = \eta\Gamma\left(\frac{1}{\beta}+1\right)$$

$$\text{STD of } f(x) = \eta\sqrt{\Gamma\left(\frac{2}{\beta}+1\right) - \Gamma\left(\frac{1}{\beta}+1\right)^{2}}$$

The 2-paramter Weibull distribution is commonly used in probability analysis of wind speeds as it can parameterize unimodal skewed probability density functions (PDFs) of non-negative random variables. While the Weibull PDF accurately parameterizes wind-speed PDF over much of the ocean, it can fail to accurately describe very calm regions (it does not allow for any probability of zero-wind speed).

Weibull Scale Parameter: η

Weibull Shape Parameter: β

Wind Speed: Mean

Wind Speed: RMS
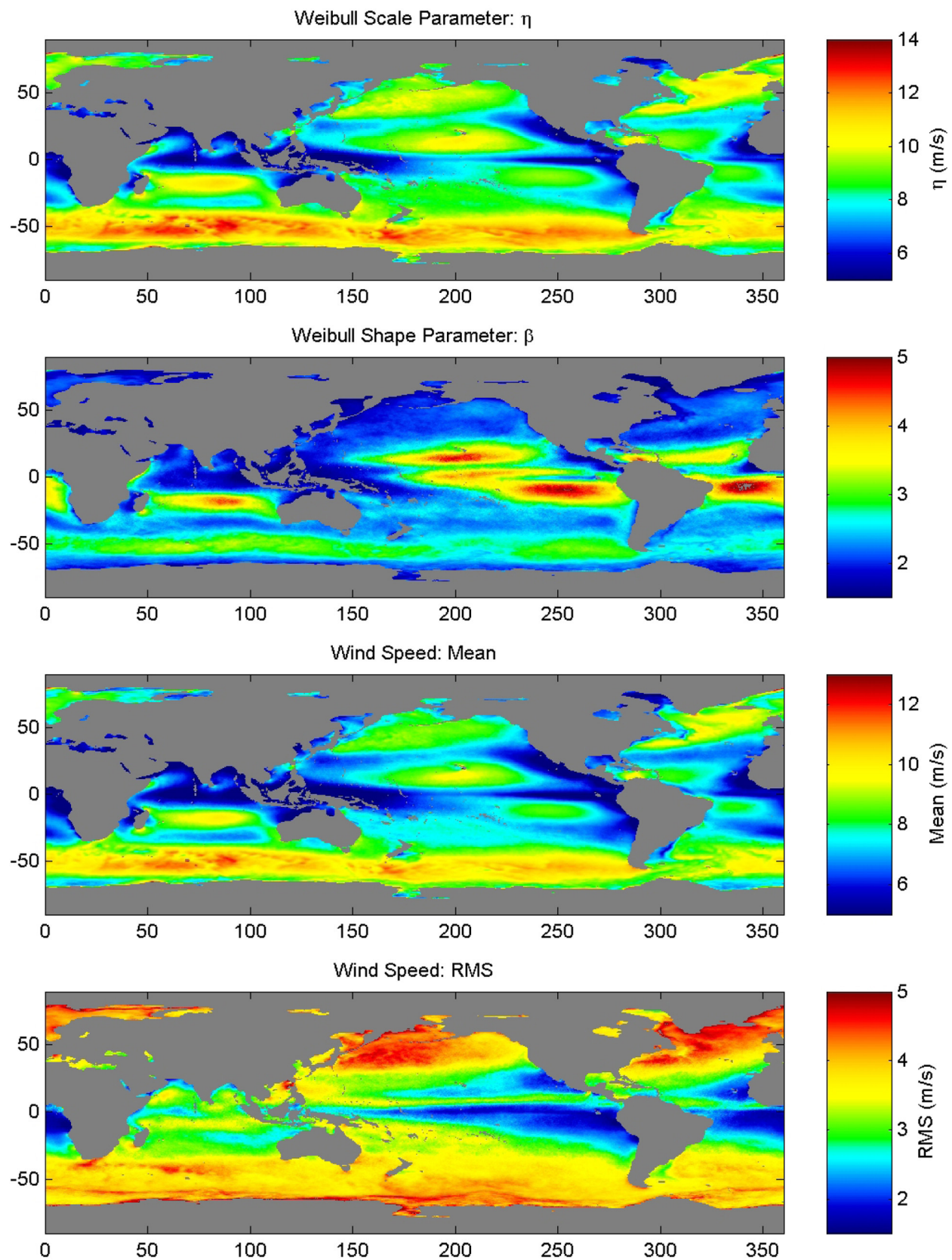
Appendix B   Global Distribution of Coral Reefs
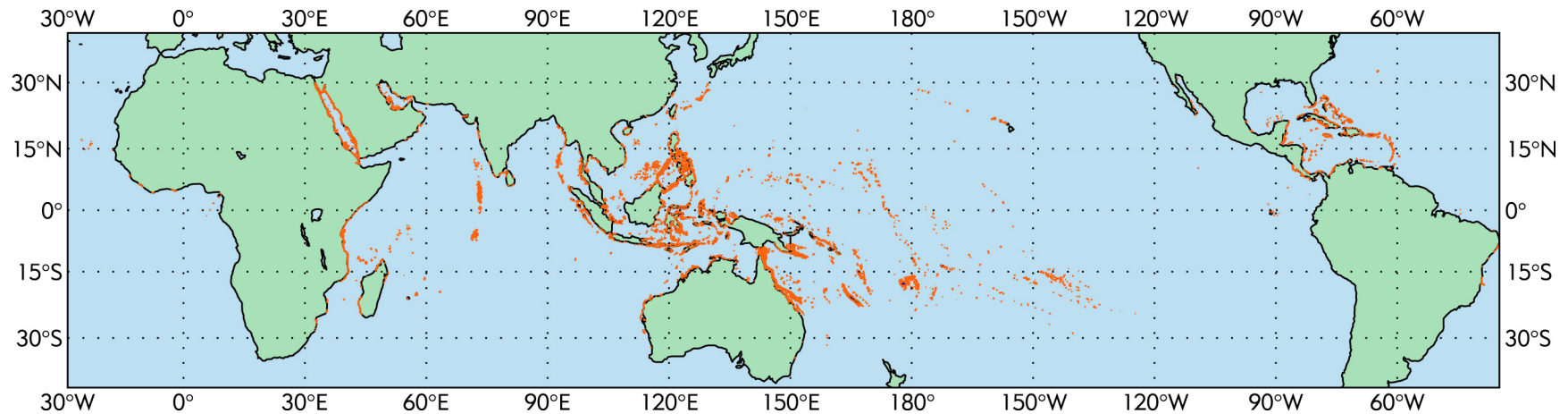
Global distribution of coral reefs (data from UNEP-WCMC). Reefs exits in the waters of over 100 countries, with an estimated area of 500,000 km^2. However, reefs are spread across 200,000,000 km^2 of ocean. Satellite remote sensing is the only feasible means of acquiring uniform scientific data across these spatial scales. Based on several previous concept studies, HyspIRI has characteristics ideally suited to global reef survey, including spatial, spectral and orbital parameters. HyspIRI will be the first ever survey to directly and uniformly assess global reef status.